First-Principles Modeling of Diffusion in Complex Materials

by

Hong Ding

A dissertation submitted in partial satisfaction of the

requirements for the degree of

Doctor of Philosophy

in

Engineering - Materials Science and Engineering

in the

Graduate Division

of the

University of California, Berkeley

Committee in charge:

Professor Mark Asta, Chair

Professor Daryl Chrzan

Professor Peter Hosemann

Fall 2014

First-Principles Modeling of Diffusion in Complex Materials

Abstract

First-Principles Modeling of Diffusion in Complex Materials

by

Hong Ding

Doctor of Philosophy in Engineering - Materials Science and Engineering

University of California, Berkeley

Professor Mark Asta, Chair

The goal of this dissertation is to explore the capability of first-principles modeling of diffusion in complex materials. Atom diffusion in ferritic alloys and electronic diffusion in α-MoO_3 are chosen as examples to demonstrate the computational study of diffusion properties in solid-state materials using first-principles modeling frameworks.

We first study the atomic diffusion problems for the development of high-temperature creep-resistant Fe-based multicomponent alloys. The temperature dependent self and solute diffusion coefficients in bcc Fe are calculated using density-functional theory, including the computation of diffusion prefactors and activation energies. For the self diffusivity, a spin-wave methodology is used for modeling the paramagnetic state to account for the effect of magnetic disorder on diffusion activation energy. Calculated self diffusion coefficients are shown to accurately reproduce the experimental measurements, including the anomaly in the Arrhenius plot near the Curie temperature. The solute impurity diffusion coefficients of the transition metal solutes (Ti-Zn, Nb-Cd and Ta-Au) are further calculated and shown to be comparable to available experimental measurements for most solutes. Our calculations show a general solute impurity diffusivity trend with minimum values for a given transition-metal row corresponding to solutes in the middle of series. Further we find a trend that diffusion of $5d$ solutes are slower than $3d$ which are slower than $4d$. The results suggest that Co, Re, Os and Ir are the slowest diffusing solute species in bcc Fe, and these elements may be effective additions for slowing coarsening rates in precipitation-strengthened ferritic alloys. Additionally, some initial work for developing an automated computational tool for calculating equilibrium point defects in intermetallic compounds is established, to assist future first-principles calculations of diffusion coefficients in these ordered alloy phases.

First-principles modeling is further employed to study adiabatic diffusion of electron small polarons in α-MoO_3, a material that has received significant attention for electrode applications in batteries and electrochemical supercapacitors. Density functional theory based calculations with van der Waals corrections (empirical dispersion corrections and van der Waals functionals) and self-interaction error corrections (Hubbard-U correction and hybrid functionals) are used to obtain accurate atomic and electronic structures of α-MoO_3, respectively. After obtaining the atomic structure of an isolated electron small polaron structure, we present a computational scheme for calculating polaron adiabatic hopping barriers in the nearest-neighbor directions. Results suggest strong polaron diffusion anisotropies in crystalline α-MoO_3. The effects of lithium-polaron binding and lattice

relaxation are further studied in order to understand their effects on electron mobilities during Li intercalation.

Overall, the results presented in this dissertation demonstrate the predictive capabilities of first-principles modeling for studying diffusion problems in complex materials. The computational framework presented here can be extended to other advanced materials of interest.

To my parents

for your $\mathcal{LOVE}$ to me

Contents

List of Figures

List of Tables

Acknowledgments

First and foremost, I would like to thank my research advisor, Prof. M. Asta, for his guidance, advice and mentorship while I pursued my degree here at Berkeley. It is his constant support and encouragement that lead me through all the ups and downs. I remembered that when I was stressed out for my preliminary exam, he took over my projects and solved problems on his own. I also remembered that when I was struggling on preparing for my qualifying exam, he helped me digest and present each piece of core knowledge. Looking back, it has been such a privilege for me to be under his tutelage.

I am also grateful for the opportunities to interact with my labmates, who helped me a lot with various aspects of my life. Thank you Drs. K. Ray, D. Olmsted, C. Ophus, V. Alexandrov, B. Hanken, and M. de Jong for patiently answering my (often naive) questions about the field when I first began my research here. Thank you Drs. N. Adelstein, T. Frolov, L. Qi, J. Solomon, I. Markus, Y. Yang, R. Freitas, T. Angsten, and D. Broberg for always being available for discussion and offering feedback. I really cherish the camaraderie we have developed through the years.

Next are all the other research collaborators who helped me think about research topics, perform calculations, analyze and summarize data, etc. Everything I presented were fruits of collaboration with these brilliant material scientists: Drs. F. Zhou, B. Sadigh, C. Liebscher, S. Huang, V. Razumovskiy, B. Medasani, W. Chen, H. Lin, C. Ni, and Profs. V. Ozolins, G. Ghosh, P. Liaw, X. Jin, and N. Mathews. I am so thankful to have had the opportunities to collaborate with you, which would not have been possible without your generous commitments of time and energy.

Additional thanks goes to my dissertation committee members: Profs. D. Chrzan and P. Hosemann, and other qualifying exam committee members: Prof. A. Minor and Dr. K. Persson. Your helpful suggestions and meticulous comments helped shape my graduate school study as well as my research.

Finally, I dedicate this dissertation to my wife, parents, extended family, and brothers and sisters at Gracepoint Church. Words cannot describe your love, care, concern, admonishment, and patience. You have provided me countless impetus and encouragements at crucial times of my life, and I owe you a debt of gratitude!

Part I

Introductory Material

Chapter 1

Introduction and Background

Diffusion has been a theoretical research topic since the early nineteenth century. The current theoretical studies of the diffusion process can be classified into different length-scales: (1) The continuum theory of diffusion was founded by German physician *Adolf Fick* in 1855 [20, 21], with his famous mathematic description of diffusion, known as Fick's laws of diffusion; (2) The microscopic picture of diffusion was motivated by the observations of Scotish botanist *Robert Brown* in 1827 [22], which led to further theoretical work by *Albert Einsten* in 1905 [23] that provided the statistical cornerstone for bridging stochastic microscopic process and macroscopic diffusion; (3) The atomistic theory of diffusion was not heralded until early 20^{th} century when German, Soviet and American physicists *Max von Laue*, *Walter Schottky*, *Yakov Frenkel* and *Ernest Kirkendall* demonstrated the important roles of point defects in controlling diffusion in crystalline materials [24, 25, 26, 27] . The time scales of diffusion problems also correspond to the diffusion rates in different material phases: the continuum and microscopic diffusion theories are inspired by the fast diffusion rates in gas and liquid, while diffusion at the atomic scale in solids occurs at a slower rate. Because diffusion processes are an integral part of microelectronics and energy applications, including ionic and electronic diffusion in batteries, and doping of semiconductors, it follows that diffusion properties in solid-state materials significantly affect material performance.

In the context of understanding diffusion phenomena in solids, extensive experimental studies have been undertaken in order to unravel the diffusion mechanisms and derive the kinetic parameters. These experiments have given some insight and basic rules for the theoretical predictions of diffusion properties in solid-state materials. However, direct observation of the diffusion processes still requires state-of-the-art characterization technologies, which results in the widespread uses of phenomenological explanations to predict diffusion mechanisms. In general, experimental measurements often provide values for diffusion coefficients that reflect an average over a specific diffusion zone and over multiple diffusion mechanisms contributing to the total diffusion flux. For example, self diffusion in closed-packed bulk crystalline materials at room temperature is mainly a vacancy-mediated process. However, the presence of other defects, such as impurities, dislocations, grain boundaries and surfaces, can significantly affect the diffusion processes and rates. Thus, it turns out to be very difficult for experiments to provide quantitive results, such as activation barriers, for individual diffusion mechanisms. Also, it is still challenging for the current

characterization techniques to detect the detailed structural information related to diffusion process , such as correlation factors and local structural distortions. The complexity of experimental studies of diffusion in solid-state materials make them both time-consuming and labor-intensive, requiring persistent and concerted efforts to produce reliable diffusion data for solids.

Considering the difficulty involved in the experimental studies, there has been a tremendous growth of interest in applying theoretical and computational modeling for studying diffusion phenomena and properties. Several computer simulation methods for modeling diffusion properties in solid-state materials have been developed. These methods cover the length scale from the atomic to continuum level, and the timescale from picosecond up to days. Figure 1.1 shows a schematic representation of these computational modeling methods over different time and length scales. The use of atomistic computational modeling for diffusion properties in solid-state materials is essential for reducing traditional experimental efforts and providing atomic parameters for mesoscale and continuum level diffusion property simulations.

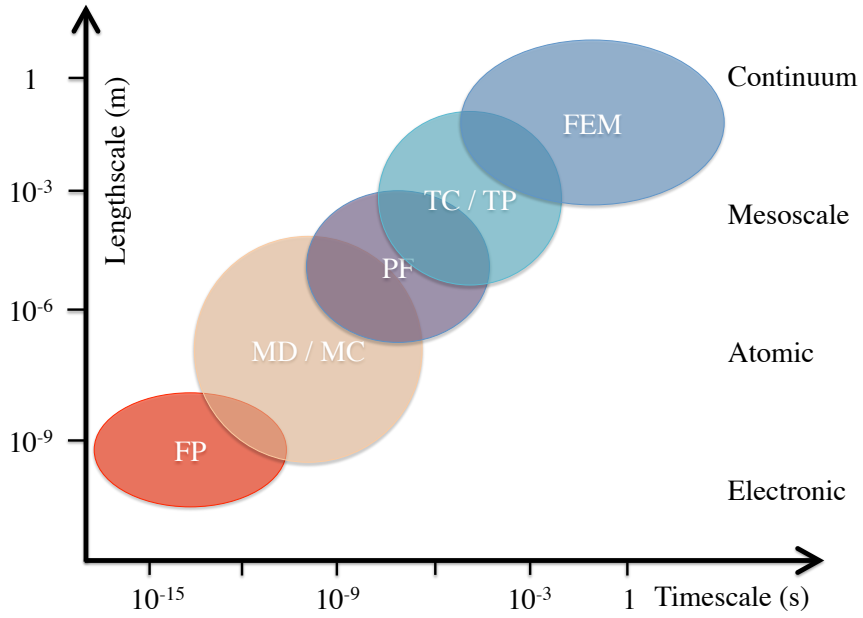

Figure 1.1: Schematic representation of the different computational modeling techniques by time and length scales: First-principles (FP), Molecular Dynamics (MD), Monte Carlo (MC), Phase Field (PF), ThermoChemical (TC) / ThermoPhysical(TP) model and Finite Element Method (FEM).

Several atomistic modeling and simulation approaches based on first-principles calculation, molecular dynamics and Monte Carlo methods have been widely developed for studying diffusion properties. A standard molecular dynamics simulation would track the motions of each atom in the simulation box within the framework of classical mechanics. Through the atomic trajectories we can derive the diffusion properties based on statis-

tical mechanics. Typically, a molecular dynamics simulation involving about millions of atoms will operate up to nanoseconds. With the improved conformational space sampling method, the accelerated molecular dynamic methods can extend the timescale further up to microseconds. Further, Monte Carlo and generalized kinetic Monte Carlo methods are other simulation approaches, which track direct exchange dynamics during the atomistic diffusion processes. Collected exchange information can be useful to analyze the spatial and temporal evolution of systems, which yield the basic diffusion properties of materials under study. Nevertheless, for the above-mentioned molecular dynamics and Monte Carlo method based studies, one of the most challenging problems is a realistic description of the interatomic interactions during the diffusion process. In particular, solid-state diffusion involves significant local crystal distortions and activation-state properties, and the relevant energy changes are hard to be accurately described based on the potentials usually used in these simulations. In this context, it is desirable to have a computational approach bridging atomic and electronic level modeling, which would give a more reliable description of energy changes during the diffusion process.

With the exponential growth of computation power in the past decades, first-principles modeling, based on density functional theory, has become a powerful alternative tool for studying the interatomic interactions at electronic and atomic level. In the framework of density functional theory, the energy of a system could be described as a functional of the atomic positions and electronic density. Previously, material thermodynamic properties have been actively studied based on first-principles modeling. The recent integration of transition-state theory and other diffusion theories leads to further extension of the modeling technique to the area of kinetic properties in materials, especially for studying diffusion properties. The application of first-principles techniques is not only capable of providing the correct interatomic interactions and energies for various diffusion processes, but also shedding light into the electronic structure effects on diffusion properties.

In what follows, we first introduce the basic theory and methodology for first-principles modeling, in particular density functional theory in Chapter 2. Several practical implementations are discussed, such as exchange-correlation functionals, weakly bonding and strong correlation interaction correction, and pseudopotential methods. Also other theories and approximations used to study diffusion properties, such as free-energy approximation and transition state theory, are discussed.

In Chapter 3, we present first-principles calculations aimed at atomic diffusivity in Fe-based alloys. This work was motivated by an experimental/computational collaborative effort of designing creep-resistant Fe-based multicomponent alloys for high-temperature applications [28, 29, 30]. The alloys under current experimental investigations contain fine dispersions of coherent, nanoscale (B2-NiAl based) intermetallic precipitates in a bcc Fe matrix. Using the calculation of alloy phase diagrams (CALPHAD) formalism [31, 32, 33] to model microstructure dynamics in such complex multicomponent phase equilibria requires various mobility data. Current first-principles calculations of self and impurity solute diffusion coefficient calculations in bcc Fe are expected to augment the solute mobility databases [34], and to give guidance for the search of slow diffusing solutes in the Fe matrix, for slowing the coarsening rate of precipitates [35]. To further help the design of intermetallic precipitate strengthened ferritic alloys, we also present the point defect studies in ordered

intermetallic compounds for future modeling of the kinetics in intermetallic precipitates.

In Chapter 4, we show first-principles calculations of small electron polaron formation and adiabatic diffusion in α-MoO_3 for electrode material applications in energy-storage devices (batteries and pseudocapacitors) [36, 37, 38, 39, 40]. The electrochemical reactions involved in energy storage applications require the conduction of charged particles (electrons and ions) across solid electrodes and liquid or solid electrolytes. Usually, the limiting factor is the ionic conductivity [41, 42, 43], whereas the unique layered structures of α-MoO_3 leads to significant interests in the electronic conductivity through polaron diffusion [44, 36, 45]. A first-principles computational scheme for evaluating the diffusion of the electron small polarons and the lithium-polaron interactions in the system is developed in the present work, in order to help understand the electron mobilities in bulk α-MoO_3.

Chapter 5 provides concluding remarks of all the work, including suggestions for future research directions.

Chapter 2

Basic Theory and Methodology

In this chapter, the basic theory and methodology for first-principles modeling of diffusion is reviewed, as background for the results presented below. The chapter is divided into three sections: Section 2.1 gives an general overview of first-principles density functional theory, Section 2.2 reviews the methods for calculating vibrational free energy to model the finite temperature effects on diffusivities, and Section 2.3 discusses the transition state theory which is used in this work for studying the temperature dependence of the rate for diffusion.

2.1 First-principles Density Functional Theory

2.1.1 Define the problem

A system with N nuclei at coordinates (R_1, R_2, ..., R_{N-1}, R_N) and n electrons at coordinates (r_1, r_2, ..., r_{n-1}, r_n), is governed by the Schrödinger equation [46]:

$$H\Psi = E\Psi \tag{2.1}$$

where Ψ is the wave function, E is the total energy of the system, and H is the full Hamiltonian given by

$$H = \underbrace{\underbrace{-\frac{\hbar^2}{2m_e}\sum_i \nabla_i^2}_{T_e} \underbrace{-\frac{\hbar^2}{2M_\alpha}\sum_\alpha \nabla_\alpha^2}_{T_n}}_{T} + \underbrace{\underbrace{\frac{1}{2}\sum_{i\neq j}\frac{e^2}{|r_i - r_j|}}_{V_{ee}} \underbrace{-\sum_{\alpha,i}\frac{e^2 Z_\alpha}{|r_i - R_\alpha|}}_{V_{en}} + \underbrace{\frac{1}{2}\sum_{\alpha\neq\beta}\frac{e^2 Z_\alpha Z_\beta}{|R_\alpha - R_\beta|}}_{V_{nn}}}_{V} \tag{2.2}$$

where the sum are over all the particles for kinetic energy T (including both electron T_e and nuclei T_n parts) and potential energy V (including electron-electron V_{ee}, electron-nuclei V_{en} and nuclei-nuclei V_{nn} parts). Here, e and Z_i denote the electron and nuclei charges, m_e and M_α denote the mass of electron and nuclei α, respectively.

The significant mass difference between electrons and nuclei (on the order of 10^3) suggests that the electron can nearly instantaneously adapt to the motion of nuclei, which

makes the Born-Oppenheimer approximation [47] accurate. The Hamiltonian for the electrons is then reduced to:

$$H = T_e + T_{en} + V_{ee} + V_{en} \tag{2.3}$$

However, this many-body problem for electrons in a Hamiltonian with nuclei coordinates is still extremely hard to solve, and further simplifications for an accurate solution is needed.

2.1.2 The Hohenberg-Kohn theorems

The most successful approximation was given in the 1960s by the Hohenberg-Kohn theorem [48], which later yielded the basic principles of density functional theory. The first theorem states that for a system consisting of n interacting electrons, the external potential $V_{\text{ext}}(\vec{r})$ and the corresponding total energy is a unique functional of the electron density $n(\vec{r})$:

$$E[n(\vec{r})] = F[n(\vec{r})] + \int n(\vec{r}) V_{\text{ext}}(\vec{r}) \tag{2.4}$$

where $F[n(\vec{r})]$ is a universal functional of $n(\vec{r})$. This theorem is more or less like a mathematical existence theorem, which alone proposed the existence of the universal function, but it does not present how to explicitly calculate this unknown functional.

The second Hohenberg-Kohn theorem states that for any particular $V_{\text{ext}}(\vec{r})$, the exact ground-state electronic density $n_0(\vec{r})$ and energy E_0 corresponds to the minimum value of the functional E:

$$E_0 = E[n_0(\vec{r})] = min\{E[n(\vec{r})]\} \tag{2.5}$$

The proofs of the theorems can be found in Ref. [49]. The theorems could also be extended to more realistic situations, which include electrons having spin, finite temperature and electric field effects.

2.1.3 Kohn-Sham Equations

In 1965, Kohn and Sham [50] proposed that the extremely complicated many-body system can be replaced with a fictitious picture for non-interacting electrons moving within an effective external potential V_{eff}. Starting from the Hohenberg-Kohn theorems, the energy can be obtain from a functional $F[n(\vec{r})]$ of the electron density $n(\vec{r})$, and in the framework of Kohn and Sham, the $F[n(\vec{r})]$ consists of three different parts, and the functional E is given by

$$E[n(\vec{r})] = T_s[n(\vec{r})] + E_H[n(\vec{r})] + E_{xc}[n(\vec{r})] + \int n(\vec{r}) V_{\text{ext}}(\vec{r}) \tag{2.6}$$

where first term is the kinetic energy of the non-interacting electrons $T_s[n(\vec{r})]$ within the non-interacting electron picture, and can be constructed by the Kohn-Sham orbitals $\phi_i(\vec{r})$:

$$T_s[n(\vec{r})] = -\frac{1}{2} \sum_i^N \phi_i^*(\vec{r}) \nabla^2 \phi_i(\vec{r}) d\vec{r} \tag{2.7}$$

and

$$n(\vec{r}) = -e\sum_{i}^{N}|\phi_i(\vec{r})|^2 \tag{2.8}$$

The second term $E_H[n(\vec{r})]$ denotes the classical static Coulomb interactions in the Hartree approximaiton:

$$E_H[n(\vec{r})] = \frac{1}{2}\int\frac{n(\vec{r})n(\vec{r'})}{|\vec{r}-\vec{r'}|} \tag{2.9}$$

and the last term is exchange-correlation energy $E_{xc}[n(\vec{r})]$, defined as

$$E_{xc}[n(\vec{r})] = (\langle T\rangle - T_s[n(\vec{r})]) + (\langle E_H\rangle - E_H[n(\vec{r})]) \tag{2.10}$$

which contains the kinetic and potential energy differences between the exact ($\langle T\rangle$ and $\langle E_H\rangle$) and non-interacting ($T_s[n(\vec{r})]$ and $E_H[n(\vec{r})]$) electrons, respectively. Hereafter, an effective potential $V_{\text{eff}}(\vec{r})$ is constructed as $V_{\text{eff}}(\vec{r}) = V_H(\vec{r}) + V_{xc}(\vec{r}) + V_{\text{ext}}(\vec{r})$ which leads to the well-known Kohn-Sham equations:

$$[-\frac{1}{2}\nabla^2 + V_{\text{eff}}(\vec{r})]\phi_i(\vec{r}) = \epsilon_i\phi_i(\vec{r}) \tag{2.11}$$

The exchange-correlation functional and the related energy expression in the Kohn-Sham approach are in general unknown and commonly approximated. The accuracy of this approach is primarily dependent on the quality of approximations for the exchange-correlation functional. Usually, the exchange-correlation functional is split into the exchange ($E_x[n]$) and correlation ($E_c[n]$) terms, i.e. $E_{xc}[n] = E_x[n] + E_c[n]$ (in Section 2.1.5, we will discuss different approximations for the exchange-correlation interactions). With these approximated exchange-correlation functionals, the Kohn-Sham equation can be solved self-consistently. The iterative process of self-consistently solving the Kohn-Sham equations is illustrated in Figure 2.1.

2.1.4 Spin-Polarized System

Electrons can be charactered with spin-up and spin-down fermions, therefore, to treat any spin-polarized system, we need an extension of the Kohn-Sham approach for calculating the ground-state charge density . Within the spin-polarized density functional theory [51], the total electron density is rigorously decomposed to two types of densities:
i) Particle density: $n(\vec{r}) = n(\vec{r},\uparrow) + n(\vec{r},\downarrow)$
and
ii) Spin density: $s(\vec{r}) = n(\vec{r},\uparrow) - n(\vec{r},\downarrow)$
where $n(\vec{r},\uparrow)$ and $n(\vec{r},\downarrow)$ denote the partial densities for spin-up ($\uparrow$) and spin-down ($\downarrow$), respectively. Following the notation of Pant and Rajagopal [52], the variational principle for obtaining the ground state partial charge density ($n_0(\vec{r})$ and $s_0(\vec{r})$) can be expressed as

$$E[n(\vec{r}), s(\vec{r})] \geq E[n_0(\vec{r}), s_0(\vec{r})] = E_0 \tag{2.12}$$

By analogy to the derivation of the Kohn-Sham Equation 2.11, the effective single-particle equation for spin-polarized systems can be expressed as

$$[-\frac{1}{2}\nabla^2 + V^{\delta}_{\text{eff}}(\vec{r})]\phi_i(\vec{r})^{\delta} = \epsilon^{\delta}_i\phi^{\delta}_i(\vec{r}) \tag{2.13}$$

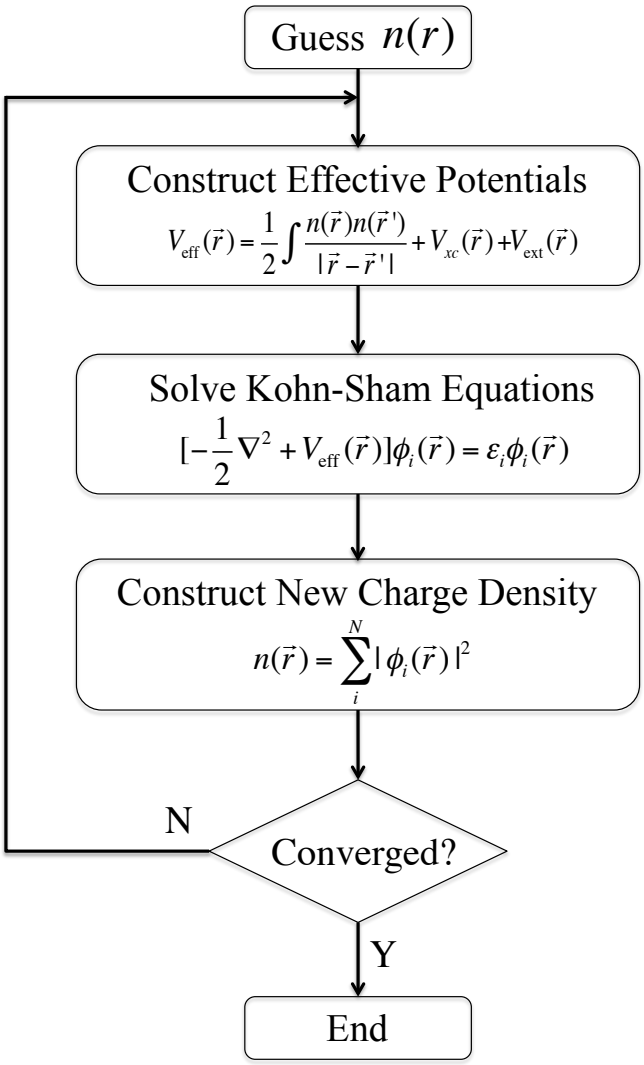

Figure 2.1: A flow chart of the iteration scheme for self-consistently solving the ground state electronic density. The calculation will converge when input and output electron density or total energy agree to within a prescribed precision.

where the two parts $\delta = \uparrow$ and $\delta = \downarrow$ are coupled and subject to an external magnetic field which is part of the effective external potential V_{eff}. For some systems, such as itinerant magnets, the lowest energy solution may be spin polarized. The spin functional accounts for magnetic effects and leads to the spin splitting in the system.

2.1.5 Exchange-Correlation Functional

In this section, we will review different approximations for defining the exchange-correlation energy as the functional of electron charge density. The most basic approach is called local density approximation (LDA), where the total exchange-correlation energy is obtained from an integration over all space for exchange-correlation energy potential $\epsilon_{xc}[n(\vec{r})]$, which is approximated with a *local* homogeneous electron gas density $n(\vec{r})$:

$$E_{xc}^{LDA}[n(\vec{r})] = \int n(\vec{r})\epsilon_{xc}[n(\vec{r})]d\vec{r} \tag{2.14}$$

The exchange-energy density in LDA can be analytically determined by the Hartree-Fock approach (neglecting the correlation interactions) and it can be analytically expressed as [53]:

$$\epsilon_x[n(\vec{r})] = -\frac{3}{4}[\frac{3}{\pi}n(\vec{r})]^{1/3} \tag{2.15}$$

However, an analytic expression for the correlation energy of the homogenous electron gas is still unknown except in the limits of infinitely-weak or infinitely-strong correlation systems. Ceperley and Alder [54] first performed quantum Monte-Carlo calculations for the homogeneous electron gas, yielding relatively accurate values of the correlation energy density for several intermediate values of the charge density, and they were later further interpolated to all densities [55].

For the system where the local charge density varies significantly, the LDA can be inaccurate. Therefore, the generalized gradient approximation (GGA) scheme was later introduced to account for the effect of the charge density gradient on exchange-correlation energy, which can be implicitly given as:

$$E_{xc}^{GGA}[n(\vec{r})] = \int n(\vec{r})\epsilon_{xc}[n(\vec{r})]F_{xc}[n(\vec{r}), \nabla n(\vec{r})]d\vec{r} \tag{2.16}$$

where $F_{xc}[n(\vec{r}), \nabla n(\vec{r})]$ is an enhancement factor chosen with different schemes. The forms of $F_{xc}[n(\vec{r}), \nabla n(\vec{r})]$ are usually carefully constructed and written as a function of Seitz radius r_s and the reduced density gradient $s(\vec{r})$. The $s(\vec{r})$ is a dimensionless parameter defined as:

$$s(\vec{r}) = \frac{|\nabla n(\vec{r})|}{2k_F(\vec{r})n(\vec{r})} \tag{2.17}$$

where $k_F(\vec{r})$ is the local Fermi momentum. Several formulations of the exchange-energy enhancement factor have been suggested, such as Becke 88 [56], PW91 [57], PBE [58] and optB88 [59] exchange functionals. The relations between enhancement factor and the magnitude of reduced density gradient for these functionals are plotted in Figure 2.2. It is known that a smaller exchange enhancement factor corresponds to less repulsive exchange functionals, which gives rise to higher energy for non-homogeneously charged systems [60].

In general, the LDA functionals tend to overbind, leading to smaller lattice constant predictions, whereas GGA functionals tend to underbind, leading to overestimation of lattice constants.

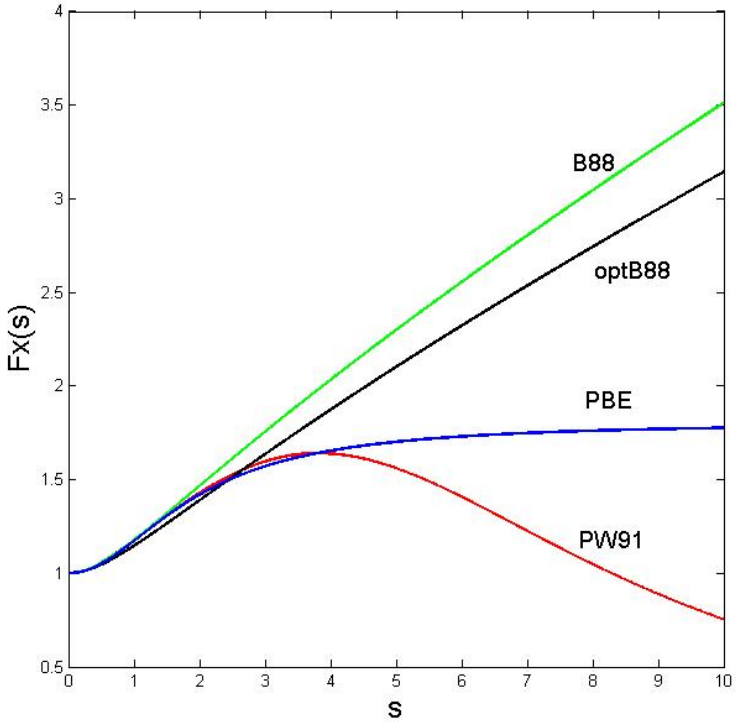

Figure 2.2: A comparison between exchange functions (F_X) and reduced charge density s for different GGA functionals.

2.1.6 Weakly-bonded interactions

The weak van der Waals (vdW) interactions are ubiquitous in nature. In particular, these vdW forces plays an important role in structural stability in materials. However, an accurate description of the vdW force is very challenging for density functional theory. The *nonlocal* features of interaction is beyond the reach of simple approximations (LDA and GGA) of conventional density functional theory. Currently, two types of computational efficient vdW interaction corrections in density functional theory have been developed to account for the dispersion forces: (1) adding semi-empirical vdW interactions or (2) employing a *nonlocal* exchange-correlation functional.

The former form of vdW force correction is an inexpensive approach but not really "first-principles". The most well-developed approach was proposed by Grimme [61], and in what follows it will be referred as the DFT-D method. In this approach, a force-field like dispersion potential $E(D)$ in asymptotic form is added between each pair of close-shell atoms located at $\vec{r}_i$ and $\vec{r}_j$:

$$E(D) = s_6 \frac{C_{ij}}{|\vec{r}_i - \vec{r}_j|^6} f_D(|\vec{r}_i - \vec{r}_j|) \tag{2.18}$$

where C_{ij} is the pairwise semi-empirical dispersion coefficients, s_6 is a parameter that de-

pends on the choice of exchange-correlation functional, and $f_D(|\vec{r}_i - \vec{r}_j|)$ is a function used to damp the singularity for $|\vec{r}_i - \vec{r}_j|^{-6}$. For the coefficient C_{ij}, in the first implementation (DFT-D1) [61], they were empirical parameters. For describing the interactions between different atoms, a mixed value in the form of a harmonic mean, i.e. $C_{ij} = 2C_iC_j/(C_i + C_j)$, was used. In the subsequent implementation (DFT-D2) [62], it instead employed the geometric mean, i.e. $C_{ij} = \sqrt{C_iC_j}$, with each atomic parameter obtained from the first-principles calculated atomic ionization potentials and dipole polarizabilities. The newer version (DFT-D3) [63] derived these values through time-dependent density functional theory calculations for different geometries, which considers more of atomic local environment. For a summary and review of this approach and implementation see Ref. [64].

The latter type of vdW force corrections expresses the vdW interactions within the $non - local$ correction terms as derived by Dion *et al.* [65] using adiabatic-connection fluctuation-dissipation theorem. The correlation functional is separated into local and non-local parts:

$$E_c = E_c^0 + E_c^{nl} \tag{2.19}$$

where the *local* part (E_c^0) still makes use of LDA functional while several other approximations are employed for the *nonlocal* part (E_c^{nl}) which accounts for vdW interactions. The particular form of the nonlocal correlation functional (E_c^{nl}) has been a subject of intensive studies, and it is usually expressed as:

$$E_c^{nl} = \frac{1}{2} \int_i \int_j n(\vec{r}_i)\phi(\vec{r}_i, \vec{r}_j)n(\vec{r}_j)d\vec{r}_i d\vec{r}_j \tag{2.20}$$

which involves a double integration of the response functional (kernel) ϕ, which is a function of charge spatial coordinates. The magnitude of the non-local term is much smaller than the local correlation term E_c^0, which makes it easy for approximating it through a simple dielectric function [65]. Several schemes have been developed to improve the efficiency of evaluating the non-local correlation energy through a double spatial integral [66].

Several schemes of exchange-correlation functional have been proposed, like original revPBE functional [67] and its alternatives optPBE, optB88 [59] and optB86b [60]. The performance of these functionals was first evaluated through a set of twenty-two dispersion-bound molecular complexes and later applied for studying other systems. Other functional forms have also been suggested in the literature, such as the VV09 [68] and VV10 [69] schemes. A modified version of van der Waals density functional (vdW-DF2) was proposed by Lee *et al.* [70] which makes uses of semi-local exchange functional (PW86) with refitted parameters (rPW86) and a non-local correlation energy kernel. Most recently, Berland and Hyldgaard further modified the exchange-correlation functional based on the plasmon description and analysis of exchange interactions in the large enhancement factor regime (vdW-DF-cx) [71], which yields more accurate predictions of lattice constant and bulk moduli for layered materials.

2.1.7 Strongly Correlated Systems

Simple density functional theory approximations also fail in some strongly-correlated systems, typically for localized states with open d and f shells, where the conventional LDA

and GGA methods yield incorrect predictions of the occupancy of the localized states. For example, LDA or GGA give partially filled d-band with metallic behavior and itinerant d-electrons for the case of one electron within an orbital-independent potential. Several attempts have been made in order to overcome this problem by taking into account the strong correlation interactions.

One approach proposed by Perdew and Zunger [55] was called self-interaction correction (SIC) method, which produces the localized nature of the electrons for transition metal compounds, while the calculated SIC one-electron energy deviates significantly from experimental measurements [72]. The Hartree-Fock (HF) method uses the term for canceling the self-interaction [73], which gives the correct discription of the Mott insulator problem. However, in the pure Hartree-Fock approximation, it neglects the screening of Coulomb interactions, which results in band gap predictions much higher than experimental measurements. In contrast, another approach called GW approximation [74, 75] treats the electron self-energy as expansion of single particle Green's function (G) and the screened Coulomb interaction (W), which can be regarded as a Hartree-Fock treatment with frequency- and orbital-dependent screened Coulomb interactions. However, the implementations of GW calculations in solids become extremely computationally expensive.

In the present study, two other approaches are employed: (1) DFT+U and (2) hybrid functional methods. The former approach introduces an orbital-dependent interaction term with an energy scale parameter U. In general, the total energy of a system in the DFT+U formalism is given as follows:

$$E_{\mathrm{DFT+U}}[n(\vec{r})] = E_{\mathrm{DFT}}[n(\vec{r})] + E_{\mathrm{Hub}}[\{n^{I\sigma}_{mm'}\}] - E_{\mathrm{dc}}[\{n^{I\sigma}\}] \tag{2.21}$$

where E_{DFT} represents the total energy functional obtained from conventional density functional theory and E_{Hub} is the term with the Hubbard Hamiltonian to correct the correlated states. The term E_{dc} is used to eliminate the "double counting" (dc) due to the presence of E_{Hub} for the correlated electrons from the conventional E_{DFT}. Here, we adopt the notation $n^{I\sigma}_{m}$ which denotes the occupation numbers of the localized orbitals with atomic site index I, state index m and spin index σ, $n^{I\sigma}_{mm'}$ is the occupation numbers product of states m and $m^{'}$, and $n^{I\sigma} = \sum_m n^{I\sigma}_m$. Within the fully localized limit implementations, Equation 2.21 can be further simplified as [76]:

$$E_{\mathrm{DFT+U}}[n(\vec{r})] = E_{\mathrm{DFT}}[n(\vec{r})] + \sum_I \frac{U^I}{2}[\sum_{m,\sigma\neq m',\sigma'} n^{I\sigma}_m n'^{I\sigma'}_m - \sum_\sigma n^{I\sigma}(n^{I\sigma}-1)] \tag{2.22}$$

where the orbital-dependent parameter U^I corresponds to the Hubbard U correction in DFT+U framework. The DFT+U method is one of the simplest approaches to improve the description of the strongly-correlated systems, which shows good performance of ground state energy, atomic force and stress calculations.

In the hybrid functional methods, the exchange-correlation functional is approximated by mixing the "exact" exchange energy from the Hartree-Fock approximation and exchange-correlation energy from conventional functionals like LDA or GGA. The Hartree-

Fock exchange functional is given as [76]:

$$E_x^{HF}[n] = -\frac{1}{2}\sum_{i,j}^{occ}\int d\vec{r}_i d\vec{r}_j \frac{\phi_i^*(\vec{r}_i)\phi_j^*(\vec{r}_j)\phi_j(\vec{r}_i)\phi_i(\vec{r}_j)}{|\vec{r}_i - \vec{r}_j|} \tag{2.23}$$

where the sum runs over all the occupied orbitals ϕ_i with the same spins. The first hybrid functional was introduced by Becke [77] by including half of Hartree-Fock exchange functional and half of conventional exchange-correlation functionals, i.e. $E_{xc} = \frac{1}{2}(E_x^{HF} + E_{xc}^{LDA/GGA})$. Several other schemes were later proposed with various modifications, like, B3LYP [78], PBE0 [79, 80] and HSE [81], which have been widely applied for studying various systems and presented good performance on addressing strong correlation issues within reasonable computational complexities.

2.1.8 Pseudopotential

A density functional theory calculation with all electrons in a solid is still cumbersome and computationally expensive. Electrons near the atomic nucleus (core electrons) are hardly affected by the dynamics of the valence electrons and external potentials. The valence electrons participate mostly for forming binding under ambient conditions, while the contribution from core electrons are rare. Therefore, the electronic properties of materials are dominated by the valence electron interactions. In this case, if we separate the dynamics of the core and valence electrons, the interaction between the core electrons and valence electrons can be approximated using an effective potential. This leaves only the valence electrons of interest for the electronic structure calculations. In particular, given that the valence ($\psi_i^v(\vec{r})$) and core ($\psi_j^c(\vec{r})$) electron wavefunctions all satisfy Kohn-Sham Equation 2.11 with eigenvalues of ϵ_i^v and ϵ_j^c, respectively, valence electron wavefunctions can be rewritten as [82]:

$$\psi_i^v(\vec{r}) = \tilde{\psi}_i^v(\vec{r}) - \sum_j < \psi_j^c|\tilde{\psi}_i^v(\vec{r}) > \psi_j^c(\vec{r}) \tag{2.24}$$

and the pseudo external field V_{ext}^{ps} for the valence electron wavefunction is given by

$$V_{ext}^{ps}\tilde{\psi}_i^v(\vec{r}) = V_{ext}\tilde{\psi}_i^v(\vec{r}) + \sum_j(\epsilon_i^v - \epsilon_j^c) < \psi_j^c|\tilde{\psi}_i^v(\vec{r}) > \psi_j^c(\vec{r})\tilde{\psi}_i^v(\vec{r}) \tag{2.25}$$

The new pseudo wavefunctions for the valence electron still satisfy the Kohn-Sham equations:

$$[-\frac{1}{2}\nabla^2 + V_{ext}^{ps}]\tilde{\psi}_i^v(\vec{r}) = \epsilon_i\tilde{\psi}_i^v(\vec{r}) \tag{2.26}$$

Here, an effective pseudopotential ($V_{ext}^{ps}\tilde{\psi}_i^v(\vec{r})$) is introduced to reproduce the valence electron density outside the core region.

Several different pseudopotential schemes have been suggested. In this work, the projected-augmented-wave (PAW) pseudopotentials [83] are used in most cases. In the PAW method, the electronic wavefunction is expressed as a valence part expanded in the plan-wave basis and a contribution from the core radius of each nucleus. The contribution from

the core region can be further written as the difference between the atomic orbitals and that wavefunction within the core region to adjust for different environments. The valence term is smooth and easy for calculation within a Cartesian grid, while the contribution from the core radius requires evaluation with radial grids. Overall, the PAW method is a convenient approach to address the feature of rapid oscillations of the valence electron wavefunction close to the ion core. Details about the implementation is available in Ref. [84].

2.1.9 Ionic force and relaxation

The ionic forces in density functional theory calculations are evaluated by applying the Hellmann-Feynman theorem [85, 86] to the variations of ionic positions:

$$\vec{F} = -\frac{\partial E}{\partial \vec{R}} = - < \phi | \frac{\partial H}{\partial \vec{R}} | \phi > \tag{2.27}$$

where ϕ denotes the ground-state wavefunction. The force on ion α at position R_α interacting with surrounding ions positioned at $\{R\}$ can be further rewritten as [82]:

$$\vec{F} = -\int_r n(r) \frac{V_{en}(r - R_\alpha)}{\partial R_\alpha} dr - \frac{\partial V_{nn}(\{R\})}{\partial R_\alpha} \tag{2.28}$$

where n(r) is the corresponding electron charge density.

For the system searching for the lowest-energy configuration, the atomic positions can be relaxed according to the ionic forces calculated with Equation 2.27 until they vanish at the equilibrium states. This kind of searching can be in general performed with different optimization methods like quasi-Newton or conjugate gradient algorithm, in order to obtain the lowest-energy equilibrium states.

2.2 Vibrational Free Energy

2.2.1 Harmonic Approximation

For systems at elevated temperature, the lattice vibrations (phonons) contribute to the total energy in the system. The harmonic approximation suggests that each atom deviates only slightly from the equilibrium position and the vibrational energy (H_{vib}) of the system is evaluated with a sum of the quadratic terms based on atomic displacements:

$$H_{vib} = \frac{1}{2} \sum_{ls\alpha, l't\beta} \phi_{ls\alpha, l't\beta} \mu_{ls\alpha} \mu_{l't\beta} \tag{2.29}$$

where μ_{ls} indicates the displacement of atom s located in unit cell l, and α and β indicate the Cartesian components. The $\phi_{ls\alpha, l't\beta}$ is the force-constant matrix defined as:

$$\phi_{ls\alpha, l't\beta} = \frac{\partial^2 U}{\partial \mu_{ls\alpha} \partial \mu_{l't\beta}} \tag{2.30}$$

with all atoms at equilibrium positions with potential energy U. The force-constant matrix connects the ion forces F_{ls} and the corresponding displacement of $\mu_{l't}$ through the relation:

$$F_{ls\alpha} = -\sum_{l't\beta} \phi_{ls\alpha,l't\beta}\mu_{l't\beta} \tag{2.31}$$

The corresponding vibration energy is determined by the number of thermally activated vibration modes at a given temperature T. Based on the harmonic approximation partition function of the lattice vibration, the Helmholtz free energy takes the form [87]:

$$F_{\text{vib}}(T) = k_B T \sum_q \sum_s \ln\{2\sinh[\frac{\hbar\omega_{qs}}{2k_B T}]\} \tag{2.32}$$

where k_B is the Boltzmann constant and ω_{qs} denotes the frequency of the s-th vibration mode with wave-vector q. The vibrational frequency ω_{qs} is the eigenvalue of the dynamical matrix $(D_{s\alpha,t\beta}(q))$ which can be calculated through Fourier transformation of the force constant matrix as:

$$D_{s\alpha,t\beta}(q) = \frac{1}{\sqrt{M_s M_t}} \sum_l \phi_{ls\alpha,0t\beta} \exp[-iq(R_{ls} - R_{0t})] \tag{2.33}$$

where the sum is over the infinite number of cells in the crystal and R_{ls} denotes the position of atom s in equilibrium state with atom mass M_s in primitive cell l. Within the high-temperature limit where $\hbar\omega_{qs} \ll k_B T$ and $\sinh(x) \approx x$ (for $x \to 0$), Equation 2.32 can be approximated as

$$F_{\text{vib}}(T) \approx k_B T \sum_q \sum_s \ln(\hbar\omega_{qs}/k_B T) \tag{2.34}$$

and the vibration entropy could be obtained as

$$S_{\text{vib}} = -(\frac{\partial F}{\partial T})_V = k_B[\sum_q \sum_s \ln(k_B T/\hbar\omega_{qs}) + 1] \tag{2.35}$$

In this work, the vibrational free energy of interest is related with the defect formation and migration free energy, which requires supercell calculations. In performing the sums over states in Equations 2.34 and 2.35 we use only the $q = 0$ modes for the supercell. For a $n_1 \times n_2 \times n_3$ supercell this corresponds to a $n_1 \times n_2 \times n_3$ sampling of the Brillouin zone of the primitive unit cell.

2.2.2 Phonon Calculations

Several schemes have been proposed to calculate the phonon vibrational frequencies ω_{qs} in Equation 2.32. To obtain the full dispersion relation, the finite displacement method [88] or the linear response method [89] based on the density functional perturbation theory can be applied. The finite displacement method involves constructing the dynamical matrix from the forces that result from displacements of atoms from their equilibrium positions, while the linear response method calculates the dynamical matrix directly from

a set of wave-vector q through evaluating the second-order change in the potential energy induced by atomic displacements.

In this work, the most direct frozen-phonon approach is employed to evaluate the vibrational frequencies at $q = 0$ mode in the supercell. In this approach all symmetry-distinct displacements in the unit cell are made and the resulting forces on all of the atoms calculated. From this information the $q = 0$ dynamical matrix can be constructed and its eigenvalues can be determined to give the required vibrational frequencies. A drawback of the frozen-phonon approach is that the chosen wave-vector q should be commensurate within the cell, and for general $q \neq 0$, the translation symmetry is lost and cannot be calculated with this approach.

2.3 Transition State Theory

The electronic and atomic diffusion calculations in the work presented below requires a description of the activated process to change from the initial to final stable states. Transition state theory has been a useful guide for understanding the basic physics of the infrequent events, and it is employed here to calculate activation energies and hopping frequencies of atoms and electrons. Herein, this process can be considered as a dynamic trajectory of the system in its configuration space. These two initial and final states correspond to two local minima on the potential energy surface, respectively, and there is a dividing surface between these two energy basins. At temperature T, the system within the initial state accumulates enough activation energy to overcome the energy barriers to reach the dividing surface. Once the dynamic trajectory for the system crosses the dividing surface, it transits to the final state basin (assuming zero recrossing) and thermalizes again before make the next transition. The residence time in a given basin is much longer than the timescale for making a transition, which makes the next transition independent with respect to previous transition.

In general, the transition state rate constant k can be written as [90]:

$$k = (k_B T/h) \exp[-\Delta G/k_B T] \tag{2.36}$$

where ΔG is the difference in free energy between the activated and equilibrium states. Substituting the definition of the Gibbs free energy $\Delta G = \Delta H - T\Delta S$, where ΔH and ΔS correspond to the enthalpy and entropy changes, respectively, we obtain

$$k = (k_B T/h) \exp[\Delta S/k_B] \exp[-\Delta H/k_B T] \tag{2.37}$$

which follows the form of an Arrhenius rate constant:

$$k = A \exp(-E_a/k_B T) \tag{2.38}$$

with $A = (k_B T/h) \exp[\Delta S/k_B]$, a pre-exponential frequency factor which determines the activation entropy and $E_a = \Delta H$, an exponential factor that depends on the activation enthalpy.

To apply transition state theory to the study of diffusion properties, it is also important to identify the minimum energy path and saddle configuration. The configurations

on the minimum energy path has the energy minimum in all other directions except along the pathway. The maximal energy barriers along the minimum energy path are reached on the saddle configuration, with one particular negative eigenvalue of the dynamical matrix corresponding to the eigenvector parallel to the path. In principle, the saddle configuration is the bottleneck of the whole transition path.

The harmonic transition state theory is a simple approximation often used for reaction rate calculations. The ideal and analytical expression of the harmonic transition state theory approximation was proposed by Vineyard in Ref. [91], which has been widely applied for studying rate constants in solids. This approach is based on the normal approximation that the potential energy surfaces around the initial state and saddle configuration are smooth for harmonic expansions of the potential energy.

Using the harmonic theory to compute the migration free energy leads to an expression for the hopping frequency involving the zero-temperature energy barrier and the vibrational frequencies in the equilibrium and saddle point states. These approximations and the high-temperature limit give rate constants under the harmonic transition state theory:

$$k = \tilde{\nu} \exp[-E_a/k_B T] \tag{2.39}$$

where the pre-exponent factor can be written as

$$\tilde{\nu} = \frac{\prod_{j=1}^{N} \nu_j^{ini}}{\prod_{j=1}^{N-1} \nu_j^{sad}} \tag{2.40}$$

where ν^{ini} and ν^{sad} denote the vibrational frequencies in the initial and saddle-point configurations, respectively. One imaginary frequency corresponding to the motion along the reaction path at the saddle-point configuration is excluded from ν_i^{sad} in the denominator.

Part II

Results and Discussion

Chapter 3

First-principles Modeling of Self Diffusion and Solute Impurity Diffusion in Ferritic Alloys

3.1 Forward

In this chapter, we focus on atomic diffusion in ferritic alloys. This study, which includes modeling of both self- and solute diffusion, was motivated by our involvement in a multi-institutional effort focused on the development of creep-resistant Fe-based multicomponent alloys for high-temperature applications. The high creep resistance of Fe-Ni-Al-Cr-based two-phase alloys under consideration in this work is understood to originate from a threshold stress controlled by a precipitation strengthening mechanism in the bcc Fe matrix [28, 29, 30]. Since the mechanical properties originate from the precipitate microstructure, there is considerable interest, for the purpose of optimizing these alloys, in understanding the precipitation kinetics, and in particular the coarsening at the service temperature [92], as the coarsening of these precipitations can lead degradation of strength [29]. The development of predictive computational approaches for modeling the precipitation kinetics are thus of interest to assist in the alloy design process.

In recent years, there has been significant progress in the modeling of precipitation kinetics in multicomponent alloys, within the framework of the so-called CALPHAD approach [31, 32, 33]. In this approach, diffusion-limited precipitation kinetics are modeled employing thermodynamic databases of free-energy functions and kinetic databases of atomic mobilities. These databases are used in software programs such as DICTRA [32, 93] to solve one-dimensional diffusion problems with boundary conditions relevant to alloy processing, and PRISMA [94] to perform mean-field kinetic modeling of precipitate nucleation, growth and coarsening. The thermodynamic databases for iron-based alloys [95] have been actively developed over the past several decades, while the kinetic databases for the alloys of interest in our work remain less advanced. For the development of mobility databases, an important quantities are the self- and solute tracer diffusion coefficients, which set the dilute-limit values for the diffusion coefficients for the matrix and solute species. Therefore, as an initial focus, the work presented in this chapter is concentrated on the development and

application of first-principles based methods to calculate self- and solute impurity-diffusion coefficients in bcc Fe, as a first step towards building a more comprehensive framework for using density functional approaches to aid in the development of more comprehensive mobility databases for ferritic alloys.

A framework using density functional theory methods for the modeling of self diffusion and solute impurity-diffusion in bcc Fe was presented in Ref. [35]. This computational approach extended previous studies of Cu, P, Ni and Cr diffusion in bcc Fe [96, 97, 98] by including vibrational frequency calculations, hopping frequency calculations within harmonic transition-state theory and solute diffusion correlation factors calculated within Le Claire's nine-frequency model for a direct computation of diffusion pre-factor. The work also combined density-functional-theory calculated vacancy formation and migration energies, solute-vacancy binding energies and solute migration energies in the ordered ferromagnetic state with a semi-empirical treatment of the effects of magnetic disorder. The approach has been applied for other bcc metals, including W [99], and solute impurity diffusion calculations for W and Mo [35], and Cr, Mn, V and Ta [100] in bcc Fe.

The present work employs the computational framework outlined above to evaluate the transition metal solute ($3d$ Ti-Zn, $4d$ Nb-Cd and $5d$ Ta-Au) impurity diffusivity in bcc Fe, in order to find the general diffusivity trends among these solutes. Calculated solute diffusion coefficients for Ti, Cr, Co, Ni, Cu, Zn, Nb and Ag have been further compared with experimental measurements to assess the accuracy of the model. We further developed a spin-wave based method for direct calculations of the self-diffusion activation energy in the paramagnetic state, for modeling the effect of the magnetic phase transition on the self diffusion coefficient in bcc Fe.

For future efforts aimed at modeling precipitation kinetics in ferritic alloys, it would be desirable to develop a framework for modeling diffusion coefficients in the ordered intermetallic phases that serve as the strengthening precipitates in these materials [28, 29, 30]. As an initial step, we present work aimed at the development of automated computational tools for high-throughput calculations of intrinsic point defect concentrations in intermetallic compounds, and demonstrate initial applications for the B2 and $L2_1$ phases relevant to the alloy design effort that supported this work.

The remainder of this chapter is organized as follows. In Section 3.2 we review the basic formalism for modeling self- and solute diffusion in bcc Fe, followed by a discussion of the approach to incorporate the effect of magnetic disorder in Section 3.2.3. The approach is used to model the change in the activation energy for self diffusion due to magnetic disorder in Section 3.3. Calculated solute diffusion coefficient results are presented and compared with experimental data in Section 3.4. The intermetallic defect studies are presented in Section 3.5.

Part of the results presented in Section 3.3, including the figures and tables, were published by Hong Ding, Vsevolod I. Razumovskiy and Mark Asta, in Acta Mater., 70, 130136 (2014) [101]. The material is reproduced here with permission of the co-authors and publishers.

Part of the results presented in Section 3.4, including the figures and tables, were published by Hong Ding, Shenyan Huang, Gautam Ghosh, Peter K. Liaw and Mark Asta, in Scripta Mater., 67, 732735 (2012) [102]. The material is reproduced here with permission

3.2 Review of Atomic Diffusion Calculations

The formalism for calculating self and solute diffusion coefficients is based on classical harmonic transition-state theory, assuming a mono-vacancy mediated mechanism. The computational approach will be described in Sections 3.2.1 and 3.2.2, for self diffusion and solute diffusion in bcc Fe, respectively. A model for the effects of magnetic disorder on the calculated diffusion coefficients is summarized in Section 3.2.3.

3.2.1 Self Diffusion

For self diffusion in a cubic fcc or bcc structure, mediated by a mono-vacancy mechanism, and assuming that atomic jumps are dominated by nearest-neighbor hops, the self diffusion coefficient can be writtten as follows [103]:

$$D = a^2 f_0 C_v \Gamma, \tag{3.1}$$

where a is the lattice constant of the structure, f_0 denotes the correlation factor of the lattice ($f_0 = 0.727$ for the bcc lattice [104]), C_v is equilibrium vacancy concentration and Γ is the vacancy hopping frequency.

Under conditions of hydrostatic stress, the equilibrium vacancy concentration can be written as:

$$C_v = \exp\left(\frac{-\Delta G_v^f}{k_B T}\right) = \exp\left(\frac{-\Delta H_v^f}{k_B T}\right) \exp\left(\frac{\Delta S_v^f}{k_B}\right), \tag{3.2}$$

where k_B is the Boltzmanns constant, T is the temperature, ΔG_v^f is the Gibbs free energy for vacancy formation, given in terms of the vacancy formation enthalpy (ΔH_v^f) and entropy (ΔS_v^f) as $\Delta G_v^f = \Delta H_v^f - T\Delta S_v^f$. The high-temperature limit of the harmonic approximation for the lattice dynamics yields a constant value of ΔS_v^f [105]. Further, under ambient pressure conditions, the vacancy formation enthalpy, i.e. $\Delta H_v^F = \Delta E_v^f + P\Delta V_v^f \approx \Delta E_v^f$ can be equated with the vacancy formation energy (ΔE_v^f), since the pressure-volume contribution ($P\Delta V_v^f$) is negligible.

To compute ΔH_v^f, we can consider a supercell containing N lattice sites, and consider the total energy difference between the non-defected supercell containing N atoms ($E(N)$) and the defected supercell with $N-1$ atoms and one vacancy ($E(N-1)$), yielding:

$$\Delta H_v^f = E(N-1) - \frac{N-1}{N} E(N). \tag{3.3}$$

where $E(I)$ denotes the total energy of the supercell calculated by density functional theory. If we assume that the vacancy formation entropy (ΔS_v^f) is dominated by vibrational contributions, the value of ΔS_v^f in the high-temperature limit of the harmonic approximation can be written as follows:

$$\Delta S_v^f = k_B[\sum_{i=1}^{3(N-1)} \ln\left(k_B T/h\nu_i^{vac}\right) - \frac{N-1}{N}\sum_{i=1}^{3N} \ln\left(k_B T/h\nu_i^{bulk}\right)] \tag{3.4}$$

where ν_i^{vac} denotes a phonon frequency in the defected supercell with one vacancy and ν_i^{bulk} corresponds to the phonon frequencies in the non-defected bulk structure.

The vacancy hopping frequency (Γ) is related to the migration free energy (ΔG_v^m), i.e. $\Delta G_v^m = \Delta H_v^m - T\Delta S_v^m$, where ΔH_v^m and ΔS_v^m correspond to vacancy migration enthalpy and entropy, respectively. The vacancy migration enthalpy can be accurately approximated as the vacancy migration energy. The quantity could be calculated through the total energy difference between the supercell with vacancy migration saddle-point configuration ($E^{sad}(N-1)$) and supercell with vacancy at equilibrium configuration (($E(N-1)$)):

$$\Delta H_v^m = E^{sad}(N-1) - E(N-1) \tag{3.5}$$

According to the harmonic transition-state theory (c.f. Equation 2.37), the vacancy hooping frequency could be written as

$$\Gamma = \frac{\prod_{i=1}^{3(N-1)} \nu_i^{vac}}{\prod_{i=1}^{3(N-1)-1} \nu_i^{sad}} \exp\left(\frac{-\Delta H_v^m}{k_B T}\right) \tag{3.6}$$

where ν_i^{vac} and ν_i^{sad} denote the vibration frequencies in the vacancy and saddle-point configuration, respectively. One imaginary frequency corresponding to the motion along the diffusion path at the saddle-point configuration is excluded from ν_i^{sad} in the denominator. In what follows we will refer to the product $\nu^* = \frac{\prod_{i=1}^{3(N-1)} \nu_i^{vac}}{\prod_{i=1}^{3(N-1)-1} \nu_i^{sad}}$, as the "attempt frequency".

Substituting Equations 3.2, 3.3, 3.4 and 3.6 into Equation 3.1 gives the Arrhenius form of diffusion equation

$$D = D_0 \exp\left(-\frac{Q}{k_B T}\right) \tag{3.7}$$

where the diffusion activation energy Q is given as

$$Q = \Delta H_v^f + \Delta H_v^m \tag{3.8}$$

and the diffusion prefactor D_0 is given as

$$D_0 = a^2 f_0 \nu^* \exp\left(\frac{\Delta S_v^f}{k_B}\right) \tag{3.9}$$

3.2.2 Solute Diffusion

For solute diffusion via a monovacancy mechanism, similarly, the solute diffusion coefficient (D_s) in the limit of very dilute solute concentrations can be written as [103]:

$$D_s = a^2 f_2 C_v \exp\left(-\frac{\Delta G_b}{k_B T}\right) \Gamma_2 \tag{3.10}$$

where ΔG_b denotes the nearest-neighbor solute-vacancy binding free energy, Γ_2 is frequency for the exchange of a solute atom with nearest-neighbor vacancy and f_2 is the solute diffusion correlation factor.

To compute f_2, we employed Le Claire's nine frequency formalism [18], which takes into account of all of the symmetrically distinct atom-vacancy exchange rates when

the vacancy and solute atom are within the first and second neighbor shells, as illustrated in Figure 3.1. Each distinct exchange between surrounding atoms and vacancy would lead to a different local configuration of matrix atoms, solute and vacancy.

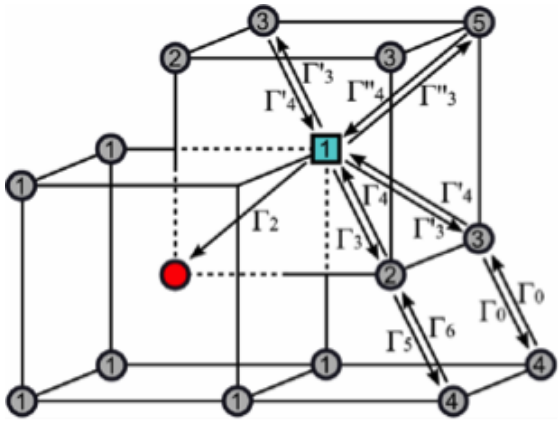

Figure 3.1: An illustration of the different vacancy hops involved in the Le Claire nine-frequency model for the correlation factor for impurity diffusion in a bcc crystal. The red circle, green square and grey circles denote the impurity solute, the vacancy and the matrix (Fe) atoms, respectively. The numbers in the circles and squares indicate the neighboring site of the solute atom. Adapted from Huang *et al.* [1].

In the formalism of Le Claire, the correlation factor is written as follows:

$$f = \frac{1 + t_1}{1 - t_1} \tag{3.11}$$

where t_1 can be expressed in terms of the nine jump frequencies shown in Fig. 3.1:

$$t_1 = -\frac{\Gamma_2}{\Gamma_2 + 3\Gamma_3 + 3\Gamma_3' + \Gamma_3'' - \frac{\Gamma_3\Gamma_4}{\Gamma_4 + F\Gamma_5} - \frac{2\Gamma_3'\Gamma_4'}{\Gamma_4' + 3F\Gamma_0} - \frac{\Gamma_3''\Gamma_4''}{\Gamma_4'' + 7F\Gamma_0}}. \tag{3.12}$$

where $F = 0.512$ and the jump frequencies can be written as

$$\Gamma_i = \nu_i^* \exp\left(-\Delta H_m / k_B T\right) \tag{3.13}$$

where ν_i^* and ΔH_m are the attempt frequency and migration energy corresponding to hopping process i, respectively. In the present work, the migration energy of each individual jump is derived from first-principles supercell calculations. The attempt frequencies (ν_i^*) in Equation 3.12 are assumed constant for all of the jump frequencies, as it was found that that f_2 is relatively insensitive to small variations in these values [1].

Regarding the solute-vacancy binding free energy ΔG_b in Equation 3.10, it can be expressed as $\Delta G_b = \Delta H_b - T\Delta S_b$, where ΔH_b and ΔS_b are the corresponding enthalpy and entropy change, respectively. In the high-temperature limit of the harmonic lattice dynamic approximation, both quantities would be constant [105]. As with the vacancy formation end migration quantities, the binding enthalpy and entropy can be derived from density

functional theory calculation, employing the N-site supercells. Specifically, the binding enthalpy can be written as

$$\Delta H_b = E(N-2,1,1) - E(N-1,1,0) - E(N-1,0,1) + E(N,0,0) \tag{3.14}$$

where $E(N-1,j,k)$ represents the total energy of a structure with $N-(j+k)$ host (Fe) atoms, j (= 0 or 1) solute atom and k (= 0 or 1) vacancy (being nearest neighbour to solute for E(N-2,1,1)). By analogy to Equation 3.4, the solute-vacancy binding entropy can be written as:

$$\Delta S_b = k_B[\sum_{i=1}^{3(N-1)} \ln(\nu_i^{vac}/\nu_i^{vac,sol}) + \sum_{i=1}^{3N} \ln(\nu_i^{sol}/\nu_i^{bulk})] \tag{3.15}$$

where $\nu_i^{vac,sol}$, ν_i^{sol} correspond to the phonon frequencies for the supercell with a nearest-neighbor solute-vacancy pair, and one isolated solute (with no vacancies), respectively. Γ_2 is defined analogously to Equation 3.6 with the saddle-point configuration corresponding to the solute atom hopping to the nearest-neighboring vacancy. Therefore, the solute diffusion coefficient could be expressed in the form of Equation 3.7, where

$$Q = \Delta H_v^f + \Delta H_b + \Delta H_m \tag{3.16}$$

and

$$D_0 = a^2 f_2 \exp[(\Delta S_v^f + \Delta S_b)/k_B]\nu^* \tag{3.17}$$

where ΔH_m is the migration energy for the solute to hop to the nearest-neighboring vacancy and ν^* is the corresponding attempt frequency which can be calculated from harmonic transition-state theory.

3.2.3 Modeling the Effect of Magnetic Disorder on Diffusion

In 1961, Buffington *et al.* discovered an anomaly near T_c in the Arrhenius plot for the self diffusion coefficient (D) of bcc Fe [4], that was confirmed in a series of subsequent experimental studies [5, 6, 7]. The anomaly involves a deviation in the temperature (T) dependence of D from normal Arrhenius behavior as T is increased through T_c. Initial theoretical explanations for this behavior were based on the decrease in the shear modulus that occurs over the same temperature range [106, 107]. Based on Girifalco's work related to the magnetic-energy contribution to the activation energy for self-diffusion (Q) [108], Ruch *et al.* [109] proposed a model for $D(T)$ in which the temperature dependence is described assuming a constant value for the prefactor (D_0) and a temperature dependence of Q originating from the effect of magnetic disorder. The resulting model for $Q(T)$ is given as follows:

$$Q(T) = Q^P[1 + \alpha S(T)^2]. \tag{3.18}$$

In Eq. 3.18, Q^P is the activation energy in the disordered paramagnetic state (assumed constant), $S(T) = M(T)/M(T = 0K)$ is the reduced magnetization at any finite temperature T (measured values for $S(T)$ are reported in [110, 111]), and α is a parameter that quantifies the dependence of Q on the state of magnetic order. Unlike the constant activation energy Q in the conventional Arrhenius expression for the diffusion coefficient as shown

in 3.7, a temperature dependence of the diffusion activation energy $Q(T)$ is introduced here. Equation (3.18) can be rewritten alternatively as:

$$Q(T) = Q^F[(1 + \alpha S(T)^2)/(1 + \alpha)] \tag{3.19}$$

where $Q^F = Q^P(1 + \alpha)$ is the activation energy in the fully ordered ferromagnetic state at zero temperature, which can be computed from density functional theory calculations.

The expression for $Q(T)$ given in Eq. 3.18 has been widely used to model both self diffusion and solute diffusion data in bcc Fe, with D_0, Q^P and α treated as fitting parameters [6, 112, 113]. Values for α derived from such analyses have been reported to range between 0.061 and 0.23 [19], suggesting that the activation energies for self and solute diffusion in ferromagnetically ordered and paramagnetically disordered bcc Fe can differ by as much as 23%. In the case of solute diffusion, semi-empirical models have been proposed that correlate the magnitude of α with the changes in local magnetic moments induced by substitutional solute species [114]. In Section 3.3, we introduce the recently developed "spin-wave" metrology for describing the energetics of paramagnetic disordered phases of magnetic materials in the framework of density functional theory, in order to model the parameter α in bcc Fe.

3.2.4 Summary

In general, the temperature dependence of self- and solute diffusion coefficients in bcc Fe are modeled in the form of:

$$D = D_0 \exp\left[-\frac{Q(T)}{k_B T}\right] \tag{3.20}$$

Here, $Q(T)$ is the temperature-dependent diffusion activation energy, accounting for the effect of magnetic disorder as given in Equation 3.19. For self diffusion, the activation energy in the fully ordered ferromagnetic state (Q^F) is calculated with Equation 3.8, with the parameter α obtained from experiments or calculations as shown in the following. For solute diffusion, we compute Q^F with Equation 3.16, with the parameter α obtained from the corresponding experiments. The values of $S(T)$ in Equation 3.18 are obtained from Refs. [110, 111].

Further, diffusion prefactors D_0 are also computed in the fully ordered ferromagnetic state, ignoring the effect of magnetic disorder. The computations follow Equation 3.9 for self diffusion and Equation 3.17 for solute impurity diffusions, respectively. The present approaches ignore the effect of magnetic disorder on diffusion prefactor, while the recent work of Wen and Woo [115] also employed molecular dynamics and spinlattice dynamics for considering the magnetic entropy contribution to vacancy diffusion. The present work makes use of the semi-empirical formalism outlined above for treating magnetic disorder effects, following most of the experimental literature on this topic (see Ref. [114] and references therein).

Regarding the entropic contribution to the diffusion prefactor, the present computational framework only considers the vibrational free energy contributions. Other contributions (like electronic excitations) to the vacancy formation, binding and migration free

energies, are found to be relatively small and negligible [35]. For the vibrational free energy calculations, the harmonic approximation is employed, not including the anharmonic effects on vacancy formation energies discussed as being important recently in calculations for Al and Cu [116]. Considering that extensive self diffusion studies in the paramagnetic state of bcc Fe have not led to significant changes of activation energies [4, 5, 6, 7, 8, 9, 10, 11, 12, 13, 14, 15, 16], such anharmonic effects are not considered in the present work.

The solute diffusion correlation factor f_2 in Equation 3.17 is calculated using Le Claire's nine-frequency model as illustrated in Figure 3.1 and Equations 3.11 and 3.12. Within the Le Claire's model, we only consider the atom-vacancy exchange rates when the vacancy and solute atom are within the first and second neighbor shells. We notice that some recent work from Garnier *et al.* [117] and Bocquet [118] reports methods for accounting for the solute-vacancy interactions up to the third nearest shells for the bcc structure. Our calculated Fe-vacancy exchange activation energies at the third neighbor shell of a solute species are comparable with the vacancy migration energy in pure bcc Fe, indicating that Le Claire's model with neglect of vacancy-solute interactions beyond the second neighbor is reasonable.

3.3 Self Diffusion Calculations in bcc Fe

3.3.1 Introduction

In the most general case, accurate modeling of the finite-temperature properties of magnetic materials requires going beyond the framework of standard density functional theory, e.g., through the use of dynamical mean-field theory [119] that includes all possible magnetic excitations The magnetic excitations result into both transverse and longitudinal fluctuations in the system. The transverse fluctuations can be characterized by the continuous rotation of the electron spin moments, while the longitudinal fluctuations affect the magnitudes of electron spin moments. For systems where the transverse magnetic fluctuations are dominant, the paramagnetic state can be modeled within the framework of density functional theory through a variety of methods.

One such approach is the disordered local moment (DLM) method [120, 121, 122, 123, 124], which describes the paramagnetic state in a manner that is equivalent to a collinear system with randomly distributed spin-up and spin-down local magnetic moments [124]. This representation of the magnetically disordered system allows one to use a very efficient coherent potential approximation (CPA) [125, 126] to calculate the electronic structure of a system in a disordered magnetic state.

As computer power has grown over the past years, another approach based on the use of supercells to model systems with random arrangements of positive and negative magnetic moments has gained popularity [127, 128, 129, 130, 131] . In such supercell approaches, the disordered magnetic state is usually modeled using either a special quasirandom structure[132], designed to mimic a perfectly random structure by reproducing its correlation functions for a certain number of the nearest neighbors around each site [127, 128, 129], or averaging over a large enough set of randomly-generated collinear magnetic structures [129, 130, 131].

The methods summarized above have different relative strengths. The CPA method is extremely computationally efficient, though current implementations of the method do not allow one to obtain accurate forces on atoms, and therefore are not practical for calculating such properties as diffusion constants or vibrational frequencies where knowledge of interatomic forces is required for atomic relaxations or for generation of the dynamical matrix. The supercell approach represents one of the most accurate ways to determine the total energy of a magnetically disordered system, which allows one to obtain, for example, a rather accurate description of a phonon spectrum of a magnetically disordered system [130]. However, in spite of the advances in computational power and algorithm development, the supercell approach remains cumbersome for calculating such properties as vacancy formation or migration energies, which require additional averaging over a set of *local* magnetic configurations around the defect.

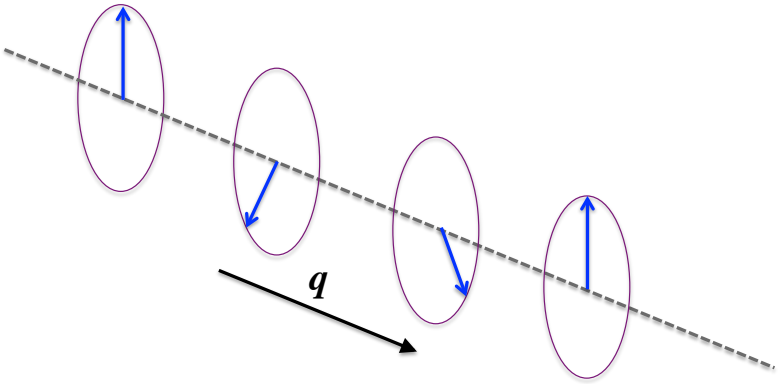

Figure 3.2: Illustration of the magnetic moments for the planar spin spiral configurations with spin wave vector q. The blue arrows denote the local magnetic moments.

In the current work we employ an alternative approach for description of the disordered magnetic state which combines attractive features of both the DLM-CPA and supercell methods. The approach is based on the density functional theory formalism for calculating the energetics of materials with planar spin-spiral magnetic configurations [133]. The planar spin-spiral magnetic configuration with spin-wave vector q is illustrated in Figure 3.2, the magnetic moment orientation at a position $\mathbf{R}$ relative to the reference site $\mathbf{r}$ can be written as:

$$m(\mathbf{r}+\mathbf{R}) = \begin{pmatrix} m_x(\mathbf{r})\cos(\mathbf{q}\cdot\mathbf{R}) - \mathbf{m_y}(\mathbf{r})\sin(\mathbf{q}\cdot\mathbf{R}) \\ m_x(\mathbf{r})\sin(\mathbf{q}\cdot\mathbf{R}) - \mathbf{m_y}(\mathbf{r})\cos(\mathbf{q}\cdot\mathbf{R}) \\ 0 \end{pmatrix} \tag{3.21}$$

where $m_x(\mathbf{r})$ and $m_y(\mathbf{r})$ are magnetic moments at the reference position $\mathbf{r}$ projected to x and y directions, respectively.

The main advantage the spin-spiral representation of a magnetic system is that for a given spin-spiral vector the system is magnetically homogenous, in the sense that all sites

in the lattice are equivalent, similar to DLM-CPA approach, but with the additional advantage that non-collinear magnetic effects are taken into account. Moreover, the spin-spiral magnetic structures can be calculated in any code supporting this type of calculation, which make it feasible to combine the spin wave methodology with the the most efficient modern first-principles methods and techniques, to obtain as accurate results in the determination of total energies as in the supercell approaches summarized above.

In what follows we first describe the spin-wave method, and then apply it to the calculation of the vacancy formation and migration energies in the paramagnetic state of bcc Fe. Combining these results with similar calculations for the ferromagnetic state allows us to compare the parameter α as defined in Equations 3.18 and 3.19 above from first-principles modeling. Using this value of α, experimentally measured values of $S(T)$ [110, 134], and diffusion prefactor calculated in the ferromagnetic state, the temperature dependence of the self-diffusion coefficient in bcc Fe can be calculated. The results are given below and compared to available experimental data.

3.3.2 Spin-Wave Method

The spin-wave method was introduced recently by Ruban and Razumovskiy [133] and it has been shown to give good predictions of the vacancy formation energy, elastic constants, and phonon spectra for bcc paramagnetic Fe. This method is based on the idea that the total energy of the ideal paramagnetic state state (i.e., a state with randomly arranged magnetic moments, neglecting short-range order) can be calculated as a sum of the energy of a set of systems with planar spin spiral configurations as [133]:

$$E^{\mathrm{IPM}} = \sum_i w_i E(\mathbf{q}_i), \tag{3.22}$$

where E^{IPM} is the total energy of the ideal paramagnetic state (IPM), $E(\mathbf{q}_i)$ is the total energy of the system with a planar spin spiral with a wavevector $\mathbf{q}_i$, and w_i are the corresponding weights (representing the degeneracy of the given $\mathbf{q}_i$ point in the Brillouin zone). In other words, the energy of the ideal paramagnetic state is represented by averaging over the magnon spectrum, as schematically illustrated in Figure 3.3.

Similar to the sampling of electronic states in regular total-energy calculations, the Brillouin-zone (BZ) integral is approximated by a sum over a set of spin-spiral configurations characterized by a finite set of special wavevectors ($\{\mathbf{q}_i\}$) within the first Brillouin zone. In previous calculations, it has been found that an accurate description of the IPM state can be obtained using relatively few $\mathbf{q}$-points generated according to the well-known special-point schemes for sampling the BZ [135, 136, 137]. For the current study, we make use of 8 Monkhorst-Pack $\mathbf{q}$-points [137] to model the ideal paramagnetic state; this level of approximation has been shown to provide an accurate representation of the energy in previous studies of the paramagnetic state in both bcc and fcc structures of Fe [133]. The 8 spin-wave vectors used in the present work are listed in Table 3.1.

The magnetic configuration can be characterized using lattice spin-spin correlation functions $\tilde{\xi}_p$:

$$\tilde{\xi}_p = \frac{1}{N} \sum_{i,j \in p} \mathbf{e}_i \mathbf{e}_j \tag{3.23}$$

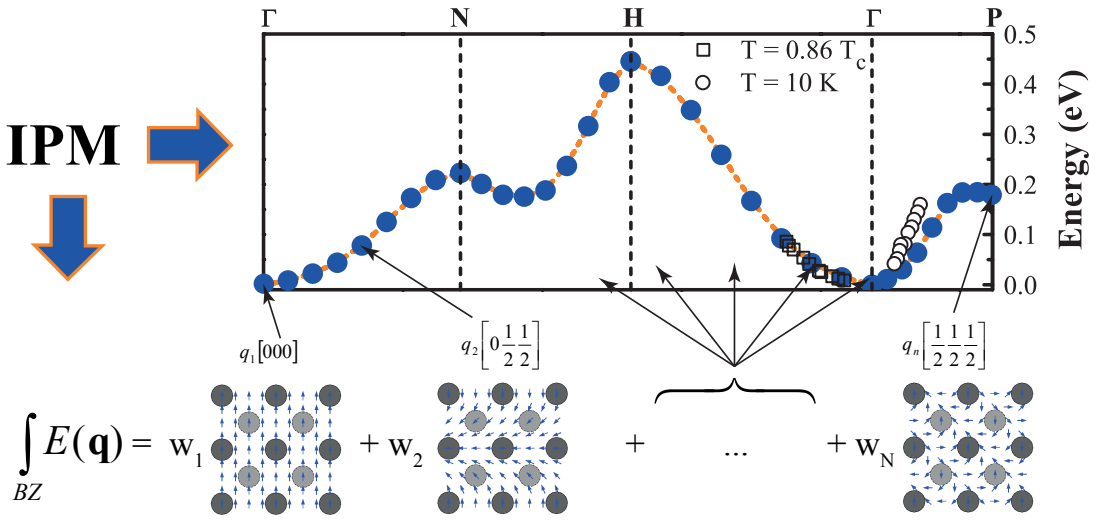

Figure 3.3: Illustration of the spin-wave based method for total energy calculations in the ideal paramagnetic state, based on the average over a set of planar spin spiral states with the weights, w_N, determined by the multiplicity of the corresponding q point in the Brillouin zone. The top right figure presents the magnon dispersion relations of bcc Fe in comparison with experimental measurements from Ref. [2] and Ref. [3].

where N is the atom number in the system for a given coordinate shell p, and $\mathbf{e}_i$ is the direction of spin at site i. It is clear all lattice spin-spin correlation functions in the IPM state with randomly arranged magnetic moments would vanish, i.e. $\tilde{\xi}_p = 0$. Here, the values of $\tilde{\xi}$ for the first 24 coordination shells obtained using 8 Monkhorst-Pack **q**-points are listed in Table 3.2. As we can see the spin-spin correlation functions $\tilde{\xi}$ have all vanished up to the 19^{th} coordination shells, which could be regarded as an excellent approximation for the ideal paramagnetic state, a state with zero magnetic short range order.

Table 3.1: The spin-wave vectors of the 8 Monkhorst-Pack **q**-points for the bcc structure used in the present work. The weights w_i are those given in Equation 3.22.

Num.	**q** $(2\pi/a)$	w_i
1	[0.00 0.00 0.00]	1/64
2	[0.25 0.00 0.25]	12/64
3	[0.50 0.00 0.50]	6/64
4	[0.50 0.25 0.25]	24/64
5	[0.50 0.50 0.50]	2/64
6	[0.00 0.50 0.00]	6/64
7	[1.00 0.75 0.75]	12/64
8	[1.00 1.00 1.00]	1/64

It should be noted that in the calculations for the paramagnetic state, the weights w_i in Eq. (3) were chosen to correspond to the ideal paramagnetic state, a state with zero magnetic short range order (MSRO). To check if this approximation was valid for

Table 3.2: Spin-spin correlation functions for the first 24 coordination shells of the bcc structure using the 8 Monkhorst-Pack **q**-points and weights as shown in Table 3.1

$Num.$	1	2	3	4	5	6	7	8	9	10	11	12
lmn	111	200	220	311	222	400	331	420	422	511	333	440
$\tilde{\xi}_{lmn}$	0.0	0.0	0.0	0.0	0.0	0.0	0.0	0.0	0.0	0.0	0.0	0.0
$Num.$	13	14	15	16	17	18	19	20	21	22	23	24
lmn	531	442	600	620	533	622	444	711	551	640	642	731
$\tilde{\xi}_{lmn}$	0.0	0.0	0.0	0.0	0.0	0.0	1.0	0.0	0.0	0.0	0.0	0.0

calculations of Q in the paramagnetic state of Fe, we performed additional calculations using the formalism described in Ref. [133], adjusting the weights to correspond to the state of MSRO calculated for Fe at $T = 1200$ K. The value of Q^P derived from these calculations accounting for MSRO was approximately 2 % higher than that obtained neglecting MSRO (i.e., in the ideal paramagnetic state). The results thus suggest that MSRO has a relatively small effect on the calculated activation energies for diffusion in bcc Fe, at least in this temperature range. Thus the contribution of MSRO is neglected in the remainder of this study.

3.3.3 Computational Details

All density functional theory calculations undertaken in this work have been performed within the framework of the PW91 generalized gradient approximation (GGA) [57], using the projector-augmented-wave (PAW) method [83, 84], as implemented in the Vienna ab-initio Simulation Package (VASP) [138]. A supercell with $N = 64$ sites ($4 \times 4 \times 4$ primitive cells) with experimentally measured lattice constants at T_c [139] has been used in calculations of vacancy formation and migration enegies (H_v^f and H_v^m, respectively) in Fe. The energy cutoff has been set to 450 eV and a k-point density equivalent to a $12 \times 12 \times 12$ mesh for a primitive unit cell has been employed. The convergence criteria have been chosen to be 10^{-5} eV for the total energy and 0.01 eV·Å^{-1} for the forces, in the self-consistency and atomic relaxation iterations, respectively. In the present work, this spin-wave approach is applied for calculations of the energy of supercells corresponding to the perfect crystal lattice, to a system with a single vacancy, and to a system in the saddle-point site for vacancy-mediated diffusion along the nearest-neighbor directions. The saddle-point geometries were obtained from force-based relaxation with the hopping atom initially put at the position halfway between neighboring vacancy sites.

In the latter calculations we average the results over all nearest-neighbor directions for a given spin-spiral state to restore the symmetry of the underlying crystal structure. . In all supercell calculations we used atomic positions obtained from relaxations in the ordered ferromagnetic state, neglecting the effect of spin disorder on the atomic relaxations.

In calculations of $D(T) = D_0 \exp(-Q/k_B T)$, the diffusion prefactor D_0 is calculated using conventional expressions from classical harmonic transition-state theory [140], with the required phonon frequencies in the binding and saddle-point configurations derived from a finite-displacement method in the magnetically-ordered ferromagnetic state

using 64-atom supercells. In these calculations, we assumed that D_0 is constant, independent of temperature, neglect ing the small (10-20%) shifts in phonon frequencies between ferromagnetic and paramagnetic states in bcc Fe [141].

3.3.4 Calculation Results of Self Diffusivity of bcc Fe

The total energies of structures with the magnetic spin configurations corresponding to the 8 Monkhorst-Pack **q**-points are plotted in Figure 3.4. In comparison with the state $\mathbf{q} = (000)2\pi/a$ corresponding to the ferromagnetic state, other states with different magnetic spin configurations all have higher energies, ranging from 0.08 to 0.45 eV per atom.

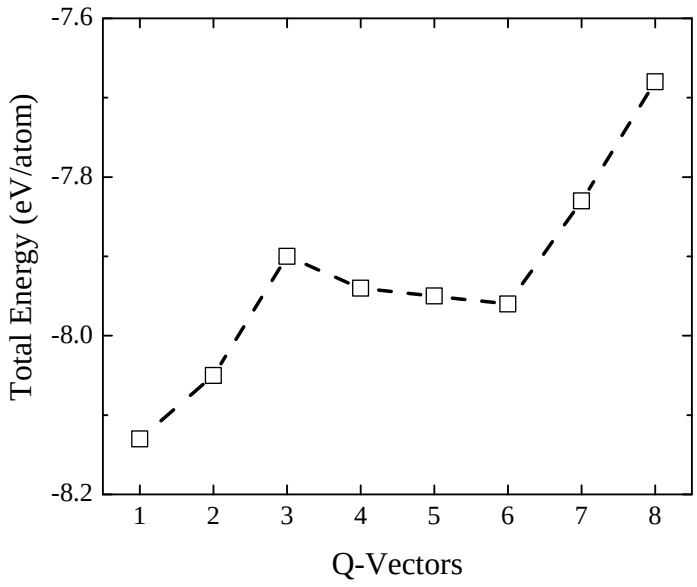

Figure 3.4: Total Energies of the structures with the magnetic spin configurations corresponding to the 8 Monkhorst-Pack **q**-points listed in Table 3.1

.

Neglecting spin-orbital coupling effects, for any structure with an given spin-wave vector, the system would be magnetically homogeneous and all the atomic sites of the lattice are symmetrically equivalent. However, the presence of a vacancy would destroy this equivalence, while the local spin-spin correlation functions around the vacancy site should still vanish. Therefore, after obtaining the total energies of the structures with different **q** vectors, we can calculate the corresponding vacancy formation energies (ΔH_v^f) by calculating the relative energy difference between the structure with and without a vacancy. The obtained vacancy formation energies of the these structures with the magnetic spin configurations corresponding to the 8 Monkhorst-Pack **q**-vectors are plotted in Figure 3.5. It can be seen that vacancy formation energy ranges from 1.08 to 2.24 eV over the given 8

q-vectors, and the minimal value of vacancy formation energy is obtained for the structure with $\mathbf{q} = (111)2\pi/a$. Similarly, the vacancy migration energy could be calculated for the states with given **q**-vectors as shown in Figure 3.6. The migration energies (ΔH_v^m) ranges from 0.25 to 0.84 eV over 8 states with different **q**-vectors.

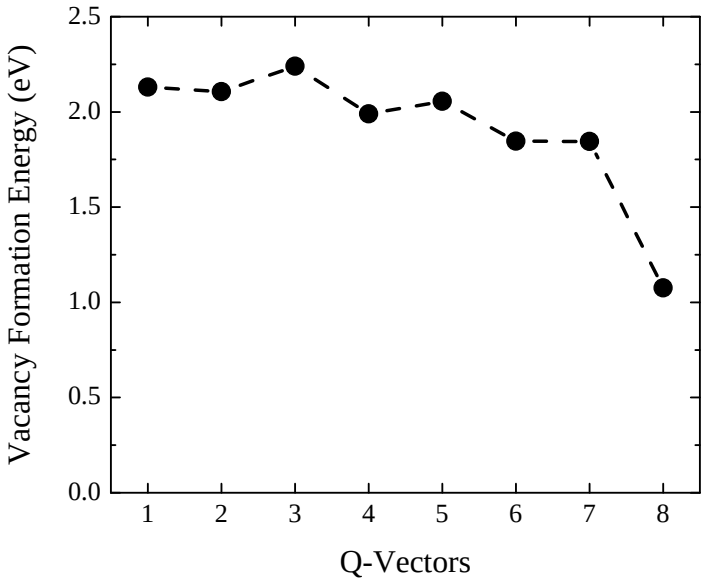

Figure 3.5: Vacancy formation energies of the structures with the magnetic spin configurations corresponding to the 8 Monkhorst-Pack **q**-points listed in Table 3.1

Averaging over the weights w_i determined by the multiplicity of the corresponding **q** point in the Brillouin zone as listed in Table 3.1 yields the vacancy formation and migration energies in the IPM state. In Table 3.3 we summarize our calculated results for the vacancy formation and migration energies, and the activation energy for self diffusion of bcc Fe in both paramagnetic and ferromagnetic states. The results are compared to available experimental data in Table 3.4. The present results for vacancy formation and migration energies in the ferromagnetic state (ΔH_v^{f-F} and ΔH_v^{m-F}, respectively) for bcc Fe are consistent with previous GGA-DFT calculations which have reported results ranging from 1.95 to 2.23 eV for ΔH_v^{f-F} and from 0.64 to 0.67 eV for ΔH_v^{m-F} (see [96, 35, 142] and references therein).

For the paramagnetic state, our results for the vacancy formation energy in Fe can be compared to the calculated relaxed and unrelaxed values reported in Ref. [133], obtained from both the DLM and spin-wave methods. For the unrelaxed vacancy formation energy at the same lattice constant used in the present calculations, the DLM and spin-wave results reported in Ref. [133] are 2.24 eV and 2.0 eV, respectively; the current calculations yield a value of 2.10 eV that is intermediate between the two values. For the relaxed vacancy formation energy the current value of 1.98 eV is considerably larger than the value of 1.77 eV

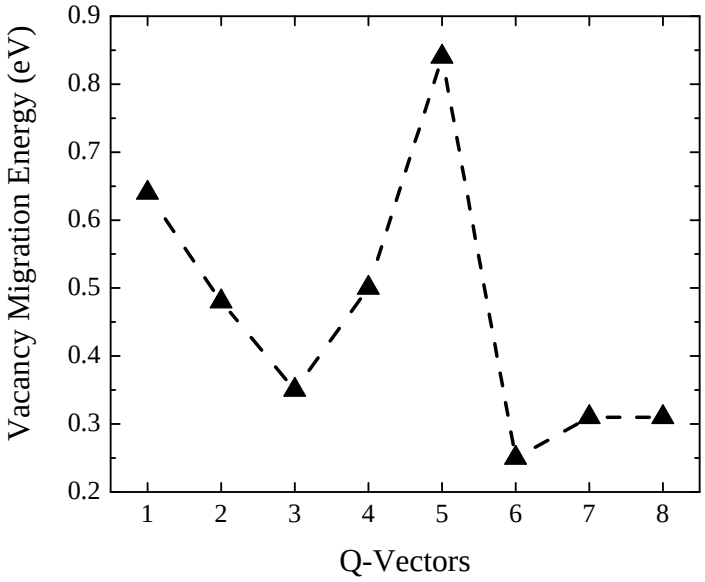

Figure 3.6: Vacancy migration energies of the structures with the magnetic spin configurations corresponding to the 8 Monkhorst-Pack **q**-points listed in Table 3.1

Table 3.3: Diffusion activation energy (Q), vacancy formation energy (ΔH_v^f) and migration energy (ΔH_v^m) of bcc Fe calculated in the ferromagnetic and paramagnetic states using the high-temperature lattice constants a (Å) close to the Curie temperature. The effect of magnetic disorder on diffusion activation energy is quantified by the energy difference (ΔQ^{F-P}), as well as the parameter $\alpha = Q^F/Q^P - 1$.

	a	Ferromagnetic			Paramagnetic			ΔQ^{F-P}	α
		ΔH_v^{f-F}	ΔH_v^{m-F}	Q^F	ΔH_v^{f-P}	ΔH_v^{m-P}	Q^P		
Fe	2.90	2.13	0.64	2.77	1.98	0.43	2.41	0.36	0.149

reported in Ref. [133] from the spin-wave method. The origin of the discrepancies between the current results and the spin-wave-method values reported in Ref. [133], which were obtained from nominally the same approach, were considered in some detail in the course of this work. It was found that this discrepancy originated from two sources. The first was the use of a smaller supercell ($3 \times 3 \times 3$) in Ref. [133], and the second was related to the choice of the energy cutoff parameter for the initial phase of the electronic minimization algorithm as described further in [143]. We note that the 0.15 eV difference in the vacancy formation energy calculated here for ferromagnetic versus paramagnetic bcc Fe is 0.06 eV smaller and 0.08 eV larger than the values reported from positron measurements in Refs. [144] and [145], respectively.

The total Q for Fe is calculated to decrease by 0.36 eV in going from the ferromagnetic to the paramagnetic state. Magnetic disordering has a comparable effect on both

Table 3.4: Experimental and calculated diffusion activation energies in the fully ordered ferromagnetic state (Q^F) and paramagnetic state (Q^P) in Fe (in units of eV), along with corresponding values of $\alpha = Q^F/Q^P - 1$.

Ref.	Q^F	Q^P	α
Present Work	2.77	2.41	0.149
Iijima [19]	3.01(5)	2.61(4)	0.156
Hettich*et al.* [5]	2.94	2.53	0.162
Lübbehusen and Mehrer [7]	2.95-3.10	2.57-2.68	0.147-0.156
James and Leak [8]	2.64	2.50	0.056
Wen *et al.* [115]	2.15(7)	1.91(5)	0.125

the vacancy formation and migration energies, with the difference between the ferromagnetic and paramagnetic states being approximately 0.2 eV for both vacancy formation and migration energies.

In Table 3.4 we list values of $\alpha = Q^F/Q^P - 1$ obtained from the present calculations and previously reported fits to experimental data for $D(T)$. The experimental values of α reported in Table 2 come from fits of the slope of the relationship between $\ln[D(T)]$ versus $1/T$ from measured self-diffusion coefficients. It can be seen that the experimental reports are somewhat scattered, with values of α for Fe ranging between 0.056 and 0.162 [5, 7, 19, 8, 115]. The current calculations result in a value of $\alpha = 0.149$ which is much closer to the upper limit of the reported values from experimental measurements (0.162). In recent work by Iijima [19], the author assessed the available experimental diffusion data and suggested the value of 0.156 for α, which agrees very well with the present calculated results.

The spin-wave DFT approach for calculating Q and α can be combined with calculations of the diffusion prefactor D_0 [146, 35] as discussed in Section 3.3.3, in order to compute the full temperature dependence of D for temperatures spanning T_c. The diffusivities are calculated for temperatures up to 1184 K for Fe (the $\gamma \rightarrow \alpha$ transition temperature). Our calculated results are compared with available experimental data in Figure 3.7. At the highest measured temperature of 1148 K from Ref. [6], the reported experimental measurement of bcc Fe self diffusivity from ref is 1.06×10^{-15} m^2s^{-1}, which is very good agreement with our predicted value of 8.66×10^{-15} m^2s^{-1}. In addition, a value of $D = 5.41\times10^{-23}$ m^2s^{-1} is reported from the same work at the lowest measured temperature of 766 K, which is also in consistent with our calculated value of 4.62×10^{-23} m^2s^{-1}. Overall, it can be seen that the calculated $D(T)$ of Fe agrees very well with the experimental measurements in the high-temperature region (>950 K), while showing slight deviations from the measurements in the lower temperature region.

Overall, the agreement between calculations and measurements is seen to be very good, with calculated values of D differing from the most recently reported measurements by no more than a factor of two over the temperature range from 0.7 to 1.1 T/T_c. Given that the current calculated results for $D(T)$ are derived directly from DFT calculations and measured values for $S(T)$, without any adjustable parameters, the level of agreement between computational and experimental results is highly encouraging.

It is noteworthy that the magnetic effect in bcc Fe, i.e. the pronounced difference of diffusion activation energies in ferromagnetic and paramagnetic states, results in more

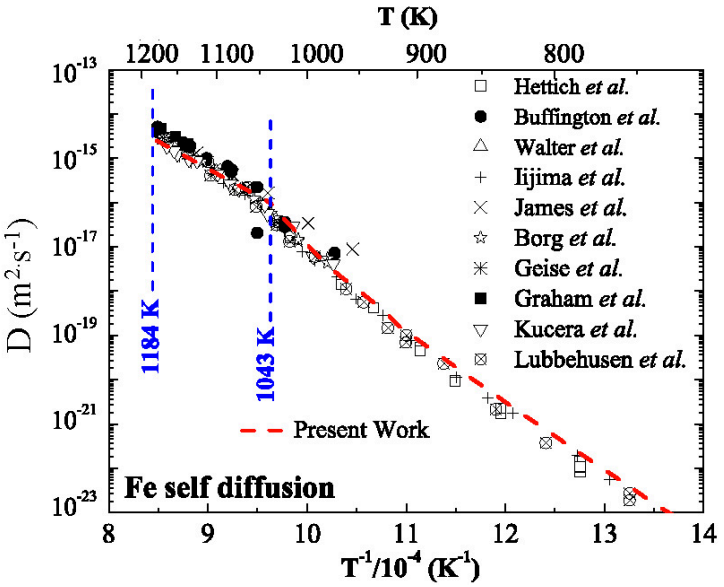

Figure 3.7: Calculated temperature dependence of self diffusion coefficients of bcc Fe in comparison with experimental data [4, 5, 6, 7, 8, 9, 10, 11, 12, 13, 14, 15, 16].

than an order of magnitude lowering of $D(T)$ below 900 K in the ferromagnetic state, relative to what would be predicted from an extrapolation of the Arrhenius behavior in the paramagnetic state. Further, the results highlight that computational predictions for Fe made by extrapolating from the zero-temperature ordered ferromagnetic state, without accounting for the effect of magnetic disorder, would lead to a large overestimation of $D(T)$ in the paramagnetic state.

3.3.5 Role of Electronic Structure

The discovery of the anomaly in the diffusion coefficient in Fe for temperatures near T_c inspired similar studies in other ferromagnetic systems like Co, in search of similar effects [106]. However, no significant change in $Q(T)$ was observed through T_c for Co within experimental accuracy [14, 15]. This result implies that α is vanishingly small for Co, and consequently the diffusion activation energy in paramagnetic and ferromagnetic states is essentially the same. To date it remains incompletely understood why Co displays an apparent absence of the anomaly in self diffusivity observed for Fe, its neighbor in the periodic table. To understand the dramatically different effect of magnetic disordering on the self diffusivity for Fe and Co, we also have employed the spin-wave method to examine activation energies in these two materials.

Calculated results for the activation energies of Co in both paramagnetic and ferromagnetic states are summarized in Table 3.5. For the ferromagnetic state, our calculations predict somewhat lower values than those reported by LaBrosse *et al.* [147] ($\Delta H_v^{f-F} = 2.34$ eV and $\Delta H_v^{m-F} = 1.19$ eV). One possible reason for this difference between our results and previously published calculations is that we have used a larger lattice parameter in our

Table 3.5: Diffusion activation energy (Q), vacancy formation energy (H_v^f) and migration energy (H_v^m) of fcc Co calculated in the ferromagnetic and paramagnetic states using the high-temperature lattice constants a (Å) close to the Curie temperature.

	a	Ferromagnetic			Paramagnetic			ΔQ^{F-P}
		ΔH_v^{f-F}	ΔH_v^{m-F}	Q^F	ΔH_v^{f-P}	ΔH_v^{f-P}	Q^P	
Co	3.60	1.99	0.77	2.76	1.97	0.76	2.73	0.03

calculations (corresponding to measurements at T_c), since we are interested in modeling diffusion near T_c. It can be seen that the calculated results show relatively small differences (a few hundredths of an eV) between the vacancy formation and migration energies in the ferromagnetic versus the paramagnetic states of Co, which lead to an almost negligible change in the diffusion activation energy Q between the two states. These results are in sharp contrast to those for Fe, where Q is calculated to decrease by 0.36 eV in going from the ferromagnetic to the paramagnetic state.

Table 3.6: Experimental and calculated diffusion activation energies in the fully ordered ferromagnetic state (Q^F) and paramagnetic state (Q^P) in fcc Co (in units of eV) [14, 15].

Spe.	Ref.	Q^F	Q^P
Co	Present Work	2.76	2.73
	Hirano *et al.* [14]	2.83	2.70
	Bussmann *et al.* [15]	2.99	2.99

For fcc Co, we list values of diffusion activation energies obtained from the present calculations and previously reported fits to experimental data for $D(T)$ in Table 3.6. In contrast to Fe, the magnetic phase transition is found to have a negligible effect on Q for Co, which is similar to the results obtained by Hirano *et al.* [14] based on experimental measurements.

The self diffusivities are calculated for temperatures up to 1786 K for fcc Co (the melting temperature) and compared with available experimental data [14, 15, 16, 16] in Figure 3.8. In comparison with Figure 3.8, the experimental diffusivity measurements of fcc Co are lower in magnitude than those for bcc Fe, consistent with experimental measurements, and our calculated results are found to agree best with the most recent data from Bussmann *et al.* [15]. In Figure 3.9, a comparison is made between the behavior of the diffusion coefficients in bcc Fe and fcc Co, by plotting the normalized diffusivity $D(T)/D(T_c)$ versus the inverse of the normalized temperature T/T_c near the Curie temperature, which highlights the dramatically different effect of magnetic disordering on $D(T)$ for bcc Fe and fcc Co.

In considering the origin of the differences between these two elements, we can naturally identify two main factors: (i) crystal structure (i.e., bcc versus fcc for Fe and Co, respectively) and (ii) electronic structure (e.g., band filling). Considering the first, it is typically expected that diffusion in closed packed structures (fcc) is slower than in more open structures (bcc) [148]. Consequently, the relative magnitudes of the effects of magnetic disorder on $D(T)$ in Fe and Co might be influenced by a dominant structural factor

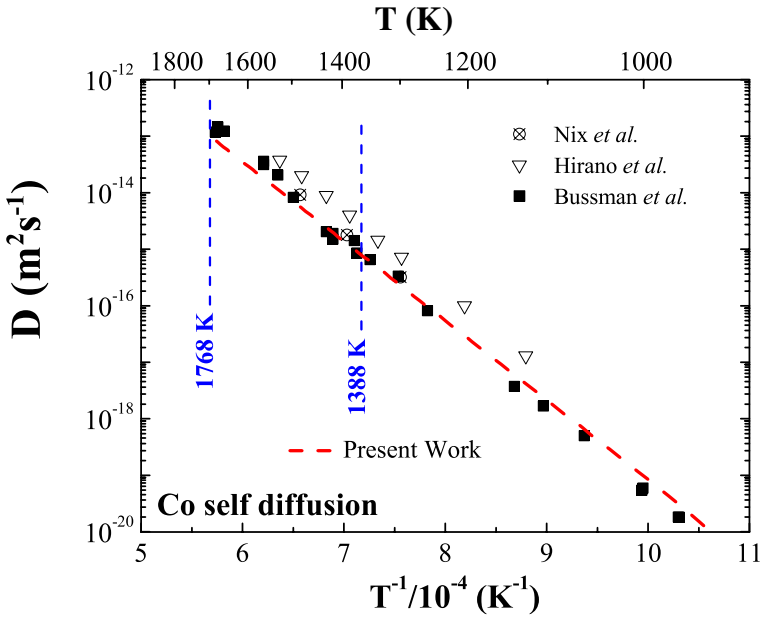

Figure 3.8: Calculated temperature dependence of self diffusion coefficients of fcc Co in comparison with experimental data [14, 15, 16].

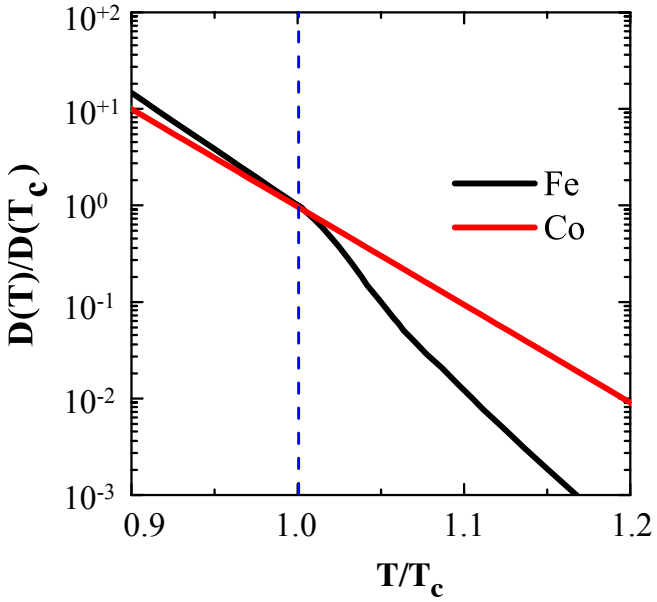

Figure 3.9: Comparison of the behavior of $D(T)$ near T_c is compared for Fe and Co.

associated with the different atomic coordinations in the fcc and bcc crystal structures. On the other hand, there is a fundamental difference between the two metals which originates from their electronic structure: for Co the spin-up d-band is completely filled, which makes it a "strong" ferromagnet following the classification of the Slater and Pauling curve [149], while in the case of Fe it is partially filled, i.e. the Fermi level crosses the majority (spin-up) band, which makes Fe a "weak" ferromagnet.

To unravel the relative importance of these two effects, we have performed additional first-principles calculations focused on the vacancy formation energy in both ferromagnetic and paramagnetic states for a series of elements with different d-band filling: Mn, Fe and Co. We perform calculations for each element in two different structures: bcc and fcc. All calculations have been performed with the intent of investigating overall trends with structure and band filling, and thus we consider ideal crystal structures without local lattice relaxations, using the same atomic volumes for bcc and fcc states. Additionally, in the application of the spin-wave method for modeling the paramagnetic state we make use of one single $\mathbf{q}$ point [135, 136], which is shown in Ref. [133] to lead to accuracy in the calculations of total energies for paramagnetic Fe to within 0.03 eV.

Table 3.7: Vacancy formation energy difference between ferromagnetic and paramagnetic states for Mn, Fe and Co (in units of eV) in bcc and fcc structures.

Structure	Mn	Fe	Co
bcc	-0.50	-0.44	-0.05
fcc	-0.43	-0.15	-0.04

Using the approach outlined in the previous paragraph, we compute vacancy formation energy differences between ferromagnetic and paramagnetic states in the series Mn, Fe and Co as shown in Table 3.7. These results show that there is a certain "dampening" effect related to the crystal structure: the energy differences between ferromagnetic and paramagnetic states are less pronounced in the fcc structure relative to the bcc structure. Additionally, these results suggest that the band-filling effect appears to be dominant, i.e., the change of the vacancy formation energy due to magnetic disorder is most pronounced for both "weak" ferromagnets Fe and Mn and it is almost absent for the "strong" ferromagnet Co. These results suggest that the origin of the anomalous behavior of D near T_C is mainly related to the electronic structure of Fe, i.e. the incomplete spin-up d-band filling. The results further suggest that the effect of magnetic disorder on $D(T)$ may vary significantly with alloying of Fe by elements that tend to increase the overall d-band filling.

3.3.6 Summary

In this section, we have demonstrated a first-principles approach for calculating self-diffusion activation energies of bcc Fe in both ferromagnetic and paramagnetic states. The calculated self-diffusion activation energy, combined with the self-diffusion prefactor calculated with the approach described in Ref. [35], we can obtain the temperature dependence of self diffusion coefficient spanning over the Curie temperature. Results obtained with this method are found to agree with the most recent experimental data to within a factor of two over the temperature range of 0.7 to 1.1 T/T_c for Fe.

The approach proposed in this work was also used to investigate the origin of the pronounced differences between Fe and Co, in terms of the effects that magnetic disorder has on the diffusion activation energies in these metals. From an analysis of vacancy formation energies in both ferromagnetic and paramagnetic states, the calculations suggest that the magnitude of the effect of the magnetic phase transition on $D(T)$ is correlated with d-band filling, and is more pronounced for "weak" magnetic elements with incompletely filled majority bands like Fe.

3.4 Solute Diffusion Coefficient Calculations in bcc Fe

In Section 3.3, we have presented a method to predict the self diffusion coefficients in bcc Fe. For the Fe-based multicomponent alloys under development in the project that supported this work, it is of more direct interest to calculate solute diffusion properties. In what follows we consider calculations of solute diffusion coefficients in the dilute limit, i.e., we consider the calculation of solute impurity-diffusion coefficients. In the context of modeling diffusion in multicomponent systems, solute impurity-diffusivities are of interest because they dictate the limiting behavior of solute mobilities in the dilute condition.

In addition to providing values that are useful in generating mobility databases, computational studies also provide insights into the mechanisms underlying variations in solute diffusion coefficients with chemistry. For example it has long been assumed that the lowest values of solute diffusion coefficients correspond to solutes that are most oversized relative to the host atoms, as these species are expected to have the largest activation energies. However, first-principles calculations (e.g., [150, 151, 152]) have shown that this "rule-of-thumb" is not generally reliable, and have pointed to the importance of more subtle electronic-structure effects. In this work we show that both the activation energies and diffusion prefactors for transition-metal solutes in bcc Fe show systematic trends versus bandfilling that cannot be easily understood based on size effects alone.

In the current work, we employ the approach described in Ref. [1] for computing solute impurity-diffusion coefficients in α-Fe within the framework of Le Claire's nine-frequency model [18], employing density-functional-theory calculations of the relevant hopping frequencies for the zero-temperature ferromagnetic state, and experimentally derived parameters to account for the effects of magnetic disorder, which have been briefly reviewed in Section 3.2.2 and Section 3.2.3. We employ this methodology in the study of $3d$ (Ti-Zn), $4d$ (Nb-Cd) and $5d$ (Ta-Au) transition metal solutes in bcc Fe, expecting the results would be useful in the context of developing mobility databases. Several solute species, e.g. Sc, Zr, Y and rare-earth solutes are not included considering the significant atomic mismatch would lead to different diffusion mechanisms as addressed later in the chapter.

In the remainder of this chapter, the trends in calculated activation energies and diffusion prefactors across these series are presented in Section 3.4.2 and Section 3.4.3, respectively. The results are obtained using computational methods described in Section 3.4.1. We then estimate the solute diffusivities neglecting magnetic disorder effects in Section 3.4.4. The comparisons between our calculations and experimentally measured solute diffusion coefficients for the species with measured values for the parameter α (see Section 3.2.3) are presented in Section 3.4.5, followed by discussion and summary.

3.4.1 Computational Details

Spin-polarized DFT calculations were performed within the generalized gradient approximation of Perdew, Burke and Ernzerhof (PBE) [58]and the projector augmented wave (PAW) method [83, 84], as implemented in the Vienna ab initio simulation package (VASP) [153, 154, 155, 156]. The plane-wave cutoff is set as 300 eV[84] and we employed Monkhorst-Pack sampling [157] of reciprocal space, with k-point grids equivalent to 12×12×12 for a conventional bcc unit cell. The saddle-point geometries were identified in a 4×4×4 bcc supercell from force-based energy minimizations where the hopping atoms were initially put at the position halfway between neighboring vacant sites. For calculations of vibrational frequencies, we computed all of the $q = 0$ normal-mode frequencies in a 3×3×3 bcc supercell using the frozen-phonon algorithm available in the VASP code.

3.4.2 Calculations of Diffusion Activation Energy

Assuming a monovacancy mechanism, the activation energy for solute diffusion in the dilute limit is given by Equation 3.16 in Section 3.2.2, as the sum of the vacancy formation energy (ΔH_f), the solute-vacancy binding energy (ΔH_b) and the solute migration energy (ΔH_m). For the $3d$ (Ti-Zn), $4d$ (Nb-Cd) and $5d$ (Ta-Au) transition metal solute species considered in the present work, the values of ΔH_b and ΔH_m calculated using density functional theory in ferromagnetic bcc Fe are listed in Table 3.8. In the convention adopted here, negative (positive) values of ΔH_b correspond to an attractive (repulsive) interaction between vacancy and solute.

Table 3.8: Solute-vacancy binding enthalpy ΔH_b for transition metal solute species (in unites of eV) in ferromagnetic bcc Fe

Group	IV	V	VI	VII	VIII	IX	X	XI	XII
	Ti	V	Cr	Mn	Fe	Co	Ni	Cu	Zn
ΔH_b	-0.27	-0.08	-0.08	-0.06	-	-0.01	-0.12	-0.28	-0.40
		Nb	Mo	Tc	Ru	Rh	Pd	Ag	Cd
ΔH_b		-0.37	-0.19	-0.15	-0.12	-0.18	-0.30	-0.55	-0.69
		Ta	W	Re	Os	Ir	Pt	Au	
ΔH_b		-0.33	-0.17	-0.13	-0.13	-0.16	-0.28	-0.32	

It can be seen that the ΔH_b are all negative, indicating the attractive interactions between the transition metal solutes and a vacancy in ferromagnetic bcc Fe. Among the solutes considered in this work, the weakest attractive interaction corresponds to the solute Co, while the strongest interaction is for Cd. Here we note our results are comparable with previously published solute-vacancy binding energies for Ti (-0.22 eV), V (-0.04 eV), Cr (-0.05 - -0.06 eV), Mn (-0.1 eV), Ni (-0.07 - -0.19 eV), Cu (-0.16 - 0.24 eV), Zn (-0.33 eV) [158, 142, 98, 159, 160]. The calculated values of the binding energies for Co (-0.1 eV) and Mo (-0.33 eV) reported in Ref. [158] are somewhat higher than the magnitudes obtained in the present work. The difference between calculations may be associated with the choice of pseudopotentials, supercell size, plane-wave cutoffs, etc.

The quantities of ΔH_b for the solute species considered in this work are also plotted

in Figure 3.10. It can be seen that in each period, the strongest solute-vacancy binding is found for solute species at the beginning or end of the transition metal series. On the other hand, group VIII solutes, i.e. Ru and Os, which are in the middle of the series, show the weakest attractive interactions with solutes. This trend among $3d$, $4d$ and $5d$ transition metal solute series is consistent with recent computational results published for ΔH_b vs. atomic number for $4d$ solute elements in bcc Fe [161]. In each group, most $4d$ transition metal solutes present the strongest solute-vacancy binding energies whereas the weakest interactions are presented by $3d$ transition metal solute species, yielding a basic trend of $\Delta H_b(3d) < \Delta H_b(5d) < \Delta H_b(4d)$. Such a trend of the solute-vacancy binding energies are generally correlated with the solute size as shown in Figure 3.11. A comparison of the values of Goldschmidt atomic radius with ΔH_b in Figure 3.12 shows a general trend that the largest magnitudes for the solute-vacancy binding energies are obtained for the largest atomic-size solute species. Similar trends were also observed for transition metal solute elements in Ni [150]and the trends were rationalized by a simple picture that large solute atoms prefer to be near vacancies in order to minimize elastic energy due to the atomic size mismatch. However, such a correlation between size and ΔH_b in Figure 3.10 and Figure 3.11 is not perfect. For example, Ta is predicted to have the largest binding energy among $5d$ transition metal solutes despite the fact that its atomic radius is slightly smaller than that of Au. Besides, both Os and Re have very similar values of ΔH_b despite the smaller size of the former. Also we can see that despite the 0.2 Å atomic-size difference between solute V and Mn, they present similar values of ΔH_b.

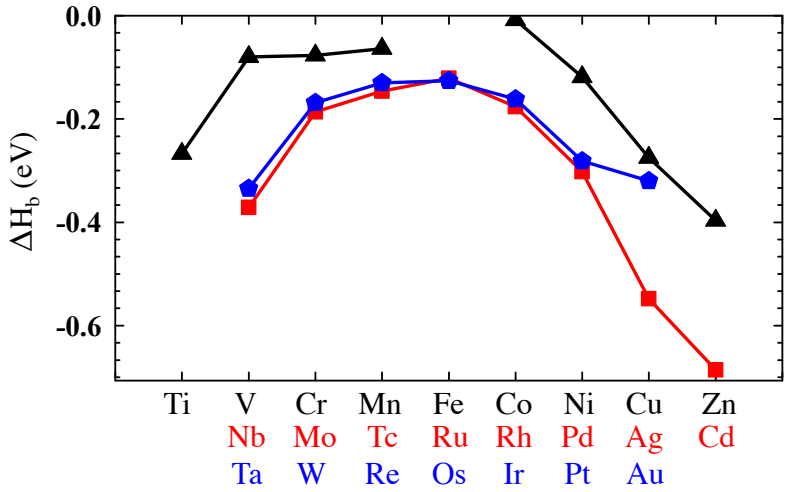

Figure 3.10: Calculated solute-vacancy binding energies ΔH_b for $3d$ (black triangle), $4d$ (red square) and $5d$ (blue pentagon) transition metal solutes in ferromagnetic bcc Fe.

Next, the solute migration energies ΔH_m for the solute species considered in the present work are given in Table 3.9. The values range from 0.35 to 0.90 eV. The lowest solute migration energy corresponds to Nb, while the solute Os shows the highest value. The

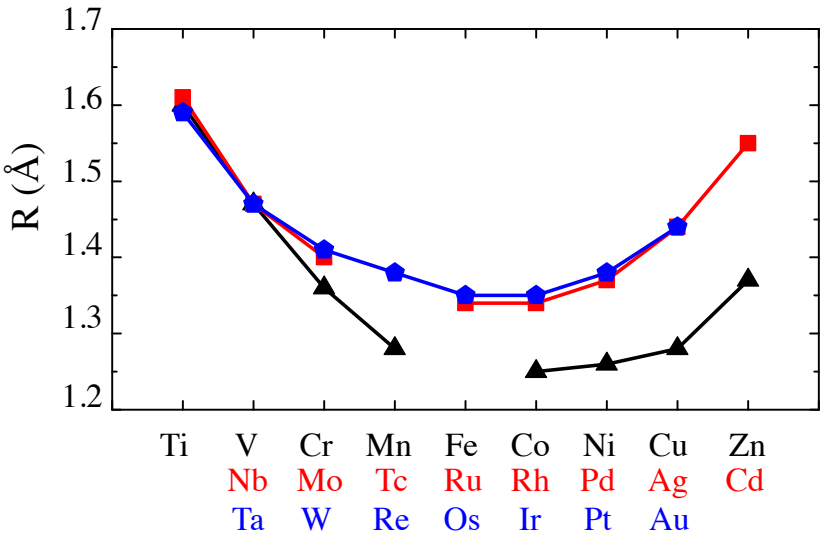

Figure 3.11: Goldschmidt atomic radius for $3d$ (black triangle), $4d$ (red square) and $5d$ (blue pentagon) transition metal series [17].

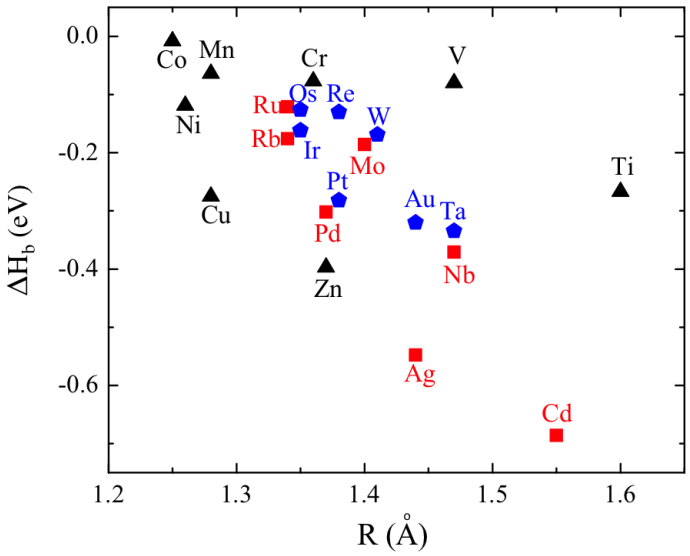

Figure 3.12: Relation between calculated solute-vacancy binding energies ΔH_b and Goldschmidt atomic radius [17] for $3d$ (black triangle), $4d$ (red square) and $5d$ (blue pentagon) transition metal series.

trend of solute migration energies ΔH_m in each transition metal solute series are plotted in Figure 3.13, featuring the maximal values corresponding to the solutes at the center of the

transition metal series.

Traditionally, it is assumed that a larger atomic-size solute species would give rise to larger lattice strain during the atomic migration process, resulting in an increase of migration energies. Comparing the trends presented in Figure 3.11 and Figure 3.13, we argue that such a "rule-of-thumb" is not reliable, as we can see that our results yield an inverse trend, namely, large atom-size solute species correspond to smaller solute migration energies. Also, it is noteworthy that the atomic size of $4d$ transition metal solutes are generally larger than that of the $5d$ solutes (from group VI to XIII). However these solutes have somewhat smaller values of solute migration energy. These trends are somewhat counterintuitive. However, similar trends have been obtained in previous calculations, e.g. for Al-based [162] and Ni-based alloys [150].

Janotti *et al.* proposed that the main reasons behind such trends were not simple strain energy due to the atomic size misfit, rather the increase of the d-state electronic bonding between the solute and the host. Due to the symmetry, the saddle point configuration has closer solute-host interatomic distances in comparison with that of binding configurations. Therefore, the solute with lower compressibility would have larger strain energy which corresponds to higher solute migration energies. In this context, a plot of the pure elementary compressibility K for the transition metal solute series are shown in Figure 3.14, which shows that the trends of K are in general consistent with the change of ΔH_m across the series. Hereby, we argue that the trend of ΔH_m are more correlated with solute compressibility as shown in Figure 3.15, instead of simply solute size, which is consistent with the explanation from Janotti *et al.* in Ref. [150].

Table 3.9: Calculated solute migration enthalpies ΔH_m (in units of eV) for solute-vacancy exchange in ferromagnetic bcc Fe for transition metal solutes.

Group	IV	V	VI	VII	VIII	IX	X	XI	XII
	Ti	V	Cr	Mn	Fe	Co	Ni	Cu	Zn
ΔH_m	0.37	0.46	0.55	0.69	-	0.72	0.62	0.50	0.43
		Nb	Mo	Tc	Ru	Rh	Pd	Ag	Cd
ΔH_m		0.35	0.52	0.68	0.73	0.73	0.62	0.43	0.34
		Ta	W	Re	Os	Ir	Pt	Au	
ΔH_m		0.43	0.71	0.86	0.90	0.88	0.85	0.76	

From Equation 3.16, the solute diffusion activation Q can be expressed as a sum of pure Fe vacancy formation energy ΔH_v^f, solute-vacancy binding energy ΔH_b and solute migration energy ΔH_m. In the present work, all these terms were calculated in the fully ordered ferromagnetic state and used to compute the corresponding value of the diffusion activation energy (Q^F). The calculated values of Q^F for the solutes are illustrated in Table 3.10 and Figure 3.16. The values of diffusion activation energy from the present calculations range from 1.85 to 2.97 eV. It is worth noticing that Co (2.92 eV), Re (2.93 eV), Os (2.97 eV) and Ir (2.92 eV) are the four solutes that have larger diffusion activation energies than the calculated self-diffusion activation energy for ferromagnetic bcc Fe (2.84 eV) using the same computational framework. These species are potential candidates for slow diffusers in bcc Fe.

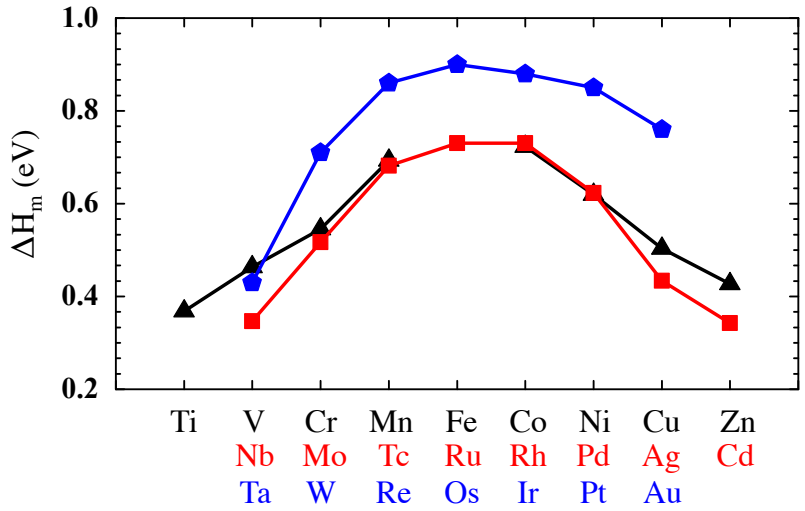

Figure 3.13: Calculated solute migration energies ΔH_m for solute-vacancy exchange in ferromagnetic bcc Fe for $3d$ (black triangle), $4d$ (red square) and $5d$ (blue pentagon) transition metal series.

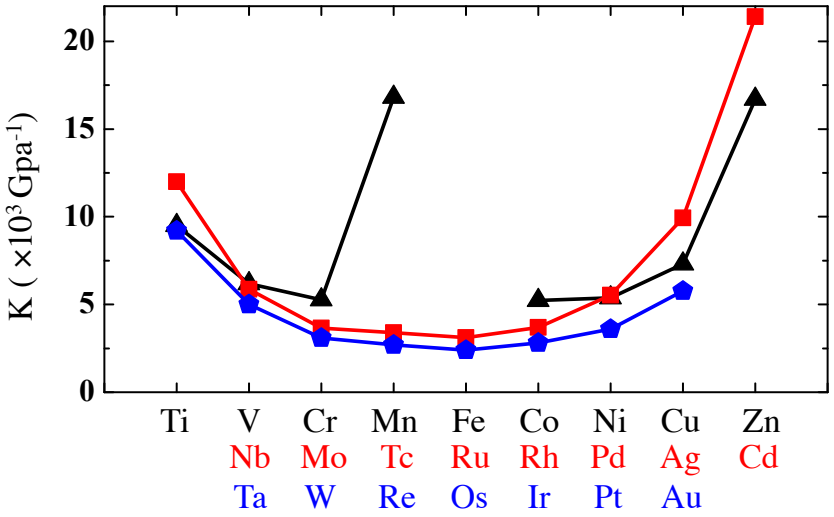

Figure 3.14: Compressibility K for $3d$ (black triangle), $4d$ (red square) and $5d$ (blue pentagon) transition metal series [17].

From the present calculations, some interesting trends for Q^F among the $3d$, $4d$, and $5d$ transition metal solute species can be observed. First, in the same period, these three series all show the maximal values of Q^F in the center, indicating the potential slow diffusivities of those solute species in the system. Next, in the same group, a general

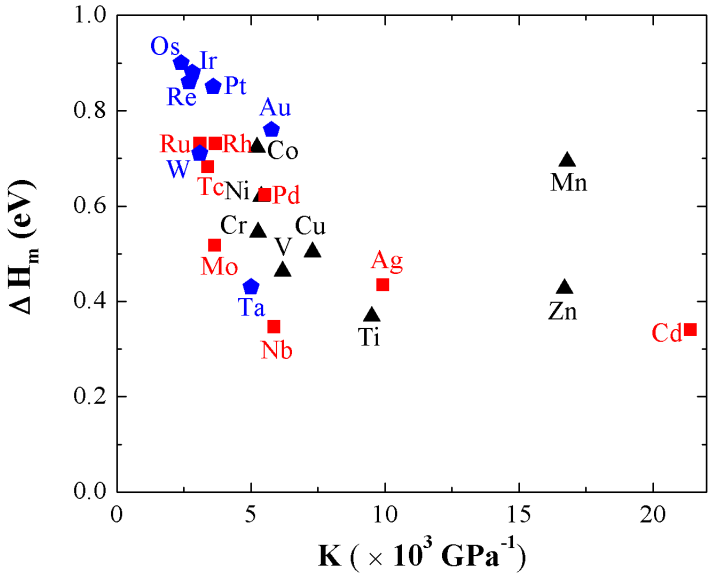

Figure 3.15: Relation between calculated solute migration energies ΔH_m and Compressibility K [17] for $3d$ (black triangle), $4d$ (red square) and $5d$ (blue pentagon) transition metal series.

trend of the ordering of the magnitudes for Q, namely, $Q_{5d} > Q_{3d} > Q_{4d}$, except group V solutes (V, Nb and Ta), is presented. This indicates that the $5d$ solutes are expected to be the slowest diffusers within each group. It can be seen that the large atomic size and small atomic compressibility of the $5d$ solute species are the main reasons for the large values of Q^F, while the differences between $4d$ and $3d$ transition metal solute species would be mainly attributed to the change of the solute-vacancy interactions ΔH_b due to the atomic size difference. We found these trends of Q^F are also in consistent with the recent computational results from the work of Zacherl *et al.* [163] in Ni alloys.

Table 3.10: Calculated solute diffusion activation energies in the fully ordered ferromagnetic state Q^F of the transition metal species considered in the present work (in units of eV).

Group	IV	V	VI	VII	VIII	IX	X	XI	XII
	Ti	V	Cr	Mn	Fe	Co	Ni	Cu	Zn
Q^F	2.30	2.58	2.66	2.83	-	2.92	2.70	2.42	2.23
		Nb	Mo	Tc	Ru	Rh	Pd	Ag	Cd
Q^F		2.17	2.57	2.73	2.81	2.75	2.52	2.08	1.85
		Ta	W	Re	Os	Ir	Pt	Au	
Q^F		2.30	2.74	2.93	2.97	2.92	2.77	2.64	

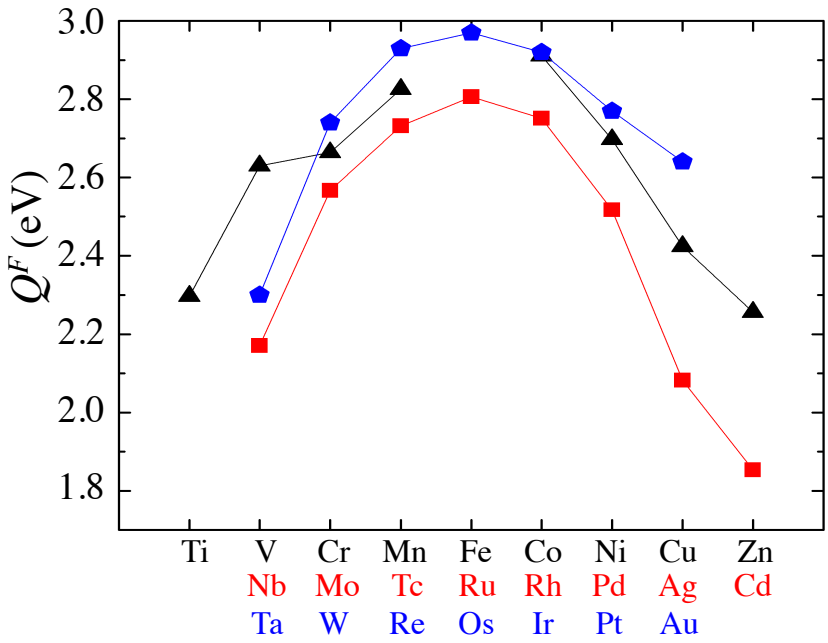

Figure 3.16: Calculated solute diffusion activation energy in the fully ordered ferromagnetic state of bcc Fe (Q^F) for $3d$ (black triangle), $4d$ (red square) and $5d$ (blue pentagon) transition metal series.

3.4.3 Calculations of Diffusion Prefactor

As shown in Equation 3.7, the diffusion prefactor can be expressed in terms of the lattice constant (a), the correlation factor (f_2), the attempt frequency for the hop of a solute atom to a nearest-neighbor vacancy (ν^*), the entropy of vacancy formation in bcc Fe (ΔS_v^f), and the entropy of vacancy binding to a nearest-neighbor solute (ΔS_b).

Diffusion Correlation Factor

We first focus on the solute diffusion correlation factor f_2. The presence of the solute next to the vacancy would also affect the surrounding matrix atom hopping rates. The atom exchange rate between the vacancy and matrix atom next to the solute would be different from those in the pure matrix, which affects the correlation factor. Unlike the self diffusion in bcc Fe with a fixed value of $f_0 = 0.727$ in Equation 3.1, the solute diffusion correlation factors (f_2) are different depending on solute species, which is related with the vacancy-solute interactions, solute and matrix atom migrations. In the present work, the value of f_2 for each solute species is derived from Le Claire's nine-frequency model [18] as discussed in Section 3.2.2. For simplicity, the attempt frequencies (ν^*) are assumed constant for all of the jump frequencies, while each migration energy was derived from the corresponding density functional theory calculations. Although the jump frequencies are a function of temperature, the temperature dependencies of the calculated values of f_2 are

relatively weak in comparison with the Arrhenius dependence of the diffusion coefficients, because they mostly depend on the ratios among the relevant vacancy migration jump frequencies rather than their exact values.

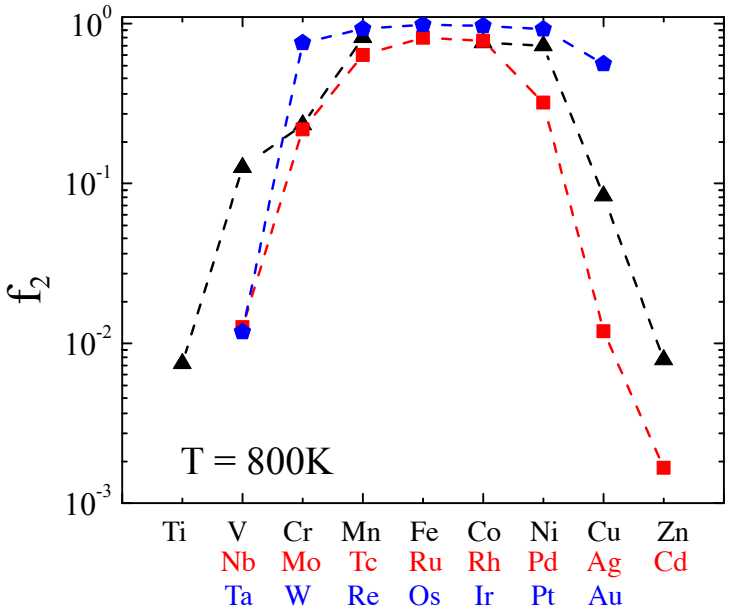

Figure 3.17: Calculated solute diffusion correlation functions f_2 within in the Le Claire's nine-frequency model [18] for $3d$ (black triangle), $4d$ (red square) and $5d$ (blue pentagon) transition metal series.

Figure 3.17 shows the calculated solute diffusion correlation factors f_2 in bcc Fe for the solute species considered in the present work at the temperature of 800 K. The calculated solute correlation factors span a range of values from 10^{-3} to 1. For the solutes at either the beginning or end of each transition metal series, anomalously small values of f_2 are obtained. For example among the $5d$ transition metal solutes, our calculations give a value of $f_2 = 0.02$ for Ta, while a value of $f_2 = 0.98$ is derived for Os. To understand the origin of these large variations between solute atoms, it is of interest to analyze the denominator of t_1 defined in Equation 3.12, which contains four contributions:

(1) $\Omega_2 = \Gamma_2$,
(2) $\Omega_3 = 3\Gamma_3 - \frac{\Gamma_3\Gamma_4}{\Gamma_4+F\Gamma_5}$,
(3) $\Omega_3^{'} = 3\Gamma_3^{'} - \frac{2\Gamma_3^{'}\Gamma_4^{'}}{\Gamma_4^{'}+3F\Gamma_0}$
(4) $\Omega_3^{''} = \Gamma_3^{''} - \frac{\Gamma_3^{''}\Gamma_4^{''}}{\Gamma_4^{''}+7F\Gamma_0}$.

These four terms corresponds to the four different jump directions for the vacancies after exchanging the position with the solute atom. We compare the different contribution terms for Ta and Os in Table 3.11. The values of Ω_3, $\Omega_3^{'}$ and $\Omega_3^{''}$ are at least 52 times

smaller than the value of Ω_2 for Ta. This situation is in contrast to the results for Os, where Ω_2 is smaller than the other three terms. For Ta, t_1 can be written to first order in the small parameter $\epsilon = (\Omega_3 + \Omega_3^{'} + \Omega_3^{''})/\Omega_2$ as $t_1 \approx -(1-\epsilon)$, leading to $f_2 \approx \epsilon$. This expression illustrates that the small value of f_2 for Ta is related physically to the much higher jump frequencies for exchange of a vacancy with Ta (Ω_2) compared to the relevant rates of exchange with neighboring Fe atoms.

Table 3.11: Contributing terms of Ω_2, Ω_3, $\Omega_3^{'}$ and $\Omega_3^{''}$ (in units of THz) to the correlation factors for Ta and Os at T = 800 K.

	Ω_2	Ω_3	$\Omega_3^{'}$	$\Omega_3^{''}$
Ta	1.9×10^{-3}	7.8×10^{-8}	3.6×10^{-5}	8.8×10^{-6}
Os	2.1×10^{-6}	7.1×10^{-5}	1.9×10^{-4}	4.6×10^{-5}

This reflects the strong solute-vacancy binding for Ta as shown in Figure 3.10, which gives rise to a large fraction of solute-vacancy hops which are followed by hops back to the original solute position. Similarly low values of f_2 have also been reported for Y in Fe [164] and Mg in Al [152].

Solute-Vacancy Binding Entropy

The solute-vacancy binding entropy ΔS_b is one term in the diffusion prefactor factor representing the vibrational contribution to the temperature dependent part of solute-vacancy binding free energy. It is determined from the vibrational entropy change, namely, the change of the vibrational frequency spectrum observed when the vacancy is bound to the solute atom, relative to when it is far from the solute. Herein, the entropy term is calculated within the high-temperature limit of the harmonic approximation as shown in Equation 3.15. Calculated values of solute-vacancy binding entropy for each solute species of interest are plotted in Figure 3.18. Within each transition metal row, a general maximal value of ΔS_b is presented in the middle of series. Also within the same column, a clear order of $\Delta S_b(3d) > \Delta S_b(4d) > \Delta S_b(5d)$ is observed. In particular, the values of ΔS_b for the $3d$ solute species are about two to three orders of magnitude higher than that for $5d$ solute species. One would speculate that the values of ΔS_b are correlated with that of ΔH_b as shown in Frigure 3.10. We found even though smaller values of ΔS_b correspond to the larger values of ΔH_b for the $3d$ solute species, similar trends are not found for the $4d$ and $5d$ transition metal species.

We also note the small cusps of ΔS_b for the group IX solutes, namely, Co, Rh and Ir. For the case of Rh, a linear interpolation from the values of ΔS_b between the neighbouring solutes (Ru and Pd) would suggest a value of ΔS_b which is 30% higher than the calculated value presented here.

Solute jump attempt frequency

We turn next to an analysis of the jump frequency for the exchange of a solute atom and a nearest-neighboring vacancy. The solute jump attempt frequency ν^* can be described within harmonic transition-state theory [140] as the quotient of product of the vibrational

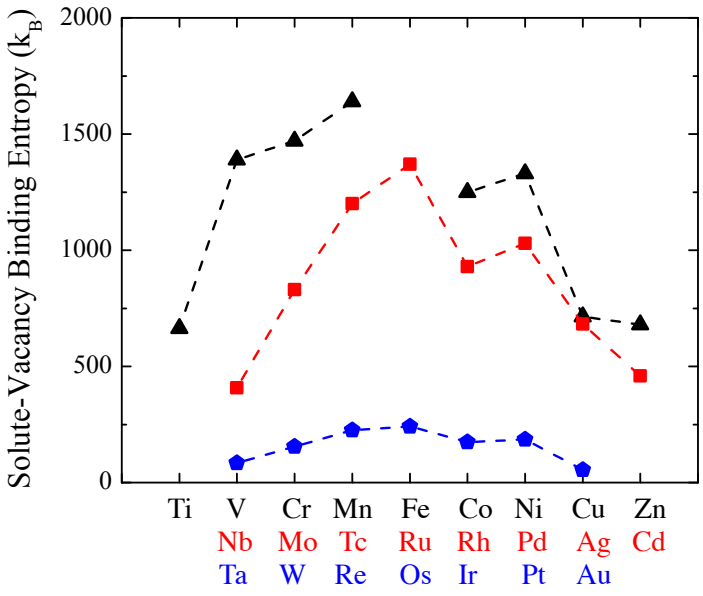

Figure 3.18: Calculated solute-vacancy binding entropy ΔS_b in ferromagnetic bcc Fe for $3d$ (black triangle), $4d$ (red square) and $5d$ (blue pentagon) transition metal series.

frequencies corresponding to a configuration with a nearest-neighbor solute-vacancy pair and the product of frequencies for a saddle-point configuration for the exchange of a solute and vacancy, excluding one imaginary frequency corresponding to the motion along the diffusion path: $\nu^* = \prod \nu_i^{\mathrm{vac,sol}} / \prod \nu_i^{\mathrm{sad}}$.

Figure 3.19 illustrates the magnitudes and trends of the calculated ν^* for the solutes considered in the present work. Here, similar magnitudes of ν^* could be found within the same transition metal row, with the maximum difference being a factor of five. However, the values of ν^* for $5d$ transition metal solutes are uniformly almost one order of magnitude higher than the corresponding $3d$ and $4d$ solutes within the same column. This trend is consistent with what has been observed for the calculated diffusion activation energies ΔH_m as presented in Figure 3.13, where the $5d$ solute species in general have larger migration energies than the other solute species.

Furthermore, we note that Mantina *et al.* suggested a double-well approach for computing vibrational modes of transition states in solid-state diffusion [165]. This model employed a statistical mechanics approach to study the characteristic vibrational frequencies of hopping atom along the migration pathway. However, to obtain the migration pathway usually requires careful minimum energy path searching algorithm, for example the nudged elastic band [166, 167], which is too expensive for the high-throughput computation in the present work.

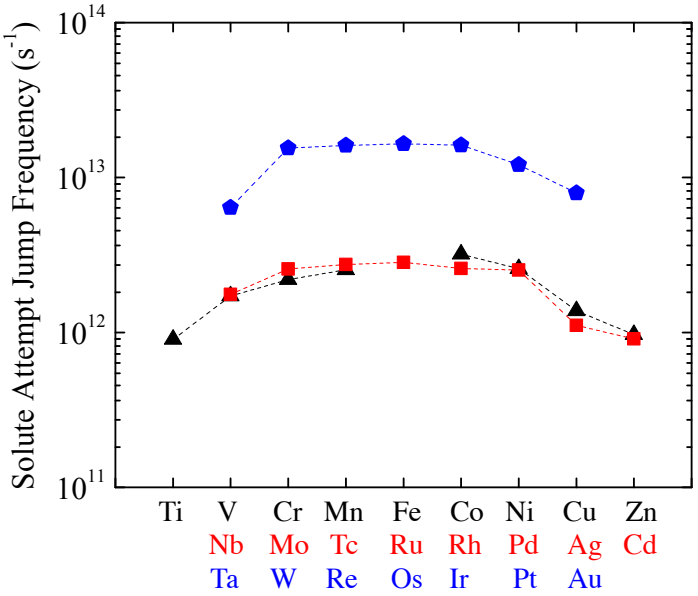

Figure 3.19: Calculated solute jump attempt frequency ν^* in ferromagnetic bcc Fe for $3d$ (black triangle), $4d$ (red square) and $5d$ (blue pentagon) transition metal series.

Solute Diffusion Prefactor

From the lattice constant a, solute diffusion correlation factor f_2, solute-vacancy binding entropy contribution $\exp(\Delta S_b/k_B)$ and solute jump attempt frequency ν^*, we can compute the prefactors for solute impurity diffusion. Here, all the calculations were done in the fully ordered ferromagnetic state of bcc Fe, and the calculated solute diffusion prefactors are plotted in Figuref 3.20 at representative temperatures of 800 K. Also for easy reference in the future, we summarize the values of Q^F and D_0 in Figure 3.21.

From Figure 3.20 we can see that the magnitudes of the prefactors for transition metal solute diffusion obtained from the present calculations are on the order of 10^{-1}-10^{+1} $\mathrm{cm^2 s^{-1}}$, except for an extremely small value of $D_0 = 0.02$ $\mathrm{cm^2 s^{-1}}$ obtained for solute Cd. Solutes from group VII to group X generally show relatively similar values of D_0 on the order of 10^{-1} $\mathrm{cm^2 s^{-1}}$, while much smaller values of D_0 are obtained at the beginning or end of the transition metal series. These relatively small values mainly are attributed to the low values for correlation factors f_2 as shown in Figure 3.17.

It is also important to address here that many previous estimations of solute diffusivities assume similar values of D_0 for different solutes, while the present calculations suggest that such an assumption would not be true for all solutes, especially for the solutes at the beginning or end of the transition-metal series which show anomalously low correlation factors. New empirical methods would thus be useful for a quick estimation of the magnitudes of D_0 for solute diffusivity in bcc Fe, given that the computations of D_0 from first-principles requires phonon calculations that are much more computationally expensive

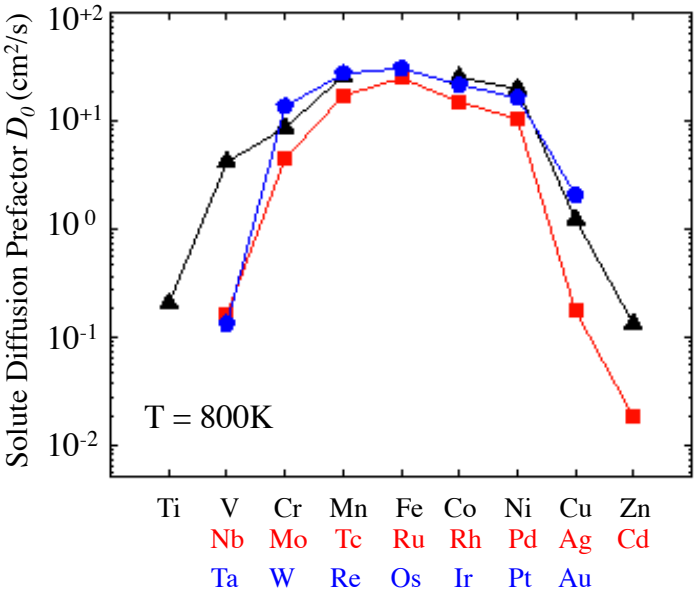

Figure 3.20: Calculated solute diffusion prefactor D_0 (at T = 800 K) for 3d (black triangle), 4d (red square) and 5d (blue pentagon) transition metal series.

than for diffusion activation enthalpy Q.

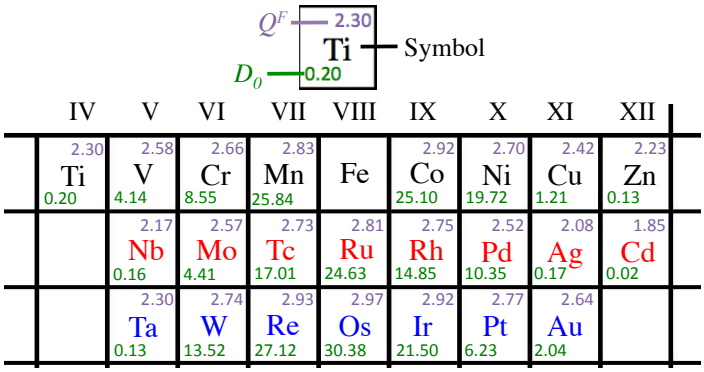

Figure 3.21: Summary of calculated values of Q^F (in unites of eV) and D_0 (at T = 800 K, in unites of cm^{2}s^{-1}) for solute impurity diffusion in the ferromagnetic state of bcc Fe

Early experimental work of Oono *et al.* [168] suggested a linear dependence of the logarithm of the diffusion prefactor D_0 with the diffusion activation energy in the paramagnetic state Q^P. By analogy, we plot the calculated D_0 (T = 800 K) vs. Q^F in Figure 3.22 and an interesting nearly-linear correlation is observed. Such a linear relationship could be

represented by the equation: $\ln(D_0)(cm^2s^{-1}) = 3.10 \cdot Q^F(eV) - 7.49$. It is found that the linear relation established here slightly overestimates the value of D_0 for the $5d$ transition metal solutes, while slightly underestimating the values for the $4d$ solutes. However, a good Pearson correlation coefficient $R^2 = 0.92$ has been achieved, indicating a very reasonable agreement could be derived between this linear relation predictions and calculated values. This relation could be used for a quick estimation of the solute diffusion prefactor from the diffusion activation energy calculations.

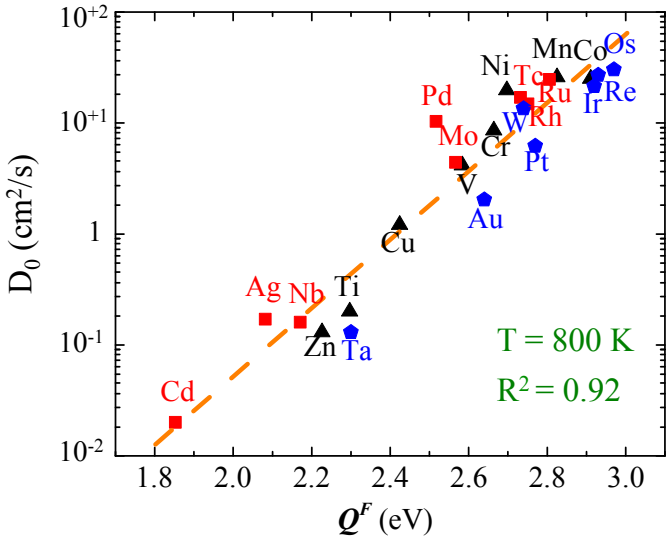

Figure 3.22: A semi-log plot of calculated values of D_0(T=800 K) versus Q_F. The dashed line represents a least-squares fit.

3.4.4 Solute Diffusivity Estimation Neglecting the Effect of Magnetic Disorder

Using the calculated Q^F and D_0, we can estimate the solute diffusivities neglecting the magnetic correction with the simple relation, i.e. $D = D_0 \cdot \exp(-Q^F/k_BT)$, where k_B is Boltzmanns constant and T is the temperature. We plot the calculated values of D at 800 K in Figure 3.23. Since the effect of magnetic disorder is neglected, instead of the absolute values, we will focus mainly on the trends in the calculated results.

It can be seen that the calculated values of D show non-monotonic dependence on the atomic number and d-band filling. The diffusion prefactor D_0 and diffusion activation energies Q^F show competing effects: solutes with higher Q^F also have higher D_0. The dominant contributions from the Arrhenius factor $\exp(-Q^F/k_BT)$ leads to the minimum values at the center of each transition metal series. In each group, we found that $Q_{5d} > Q_{3d} > Q_{4d}$ shown in Figure 3.16 results in the highest diffusivities for the $4d$ solutes among the transition metals in bcc Fe. The exception is for solute Au which is shown to have have a lower diffusion coefficient than the neighboring atom Pt. The anomaly found for Au may be due to larger errors inherent in the approximations underlying the calculations for

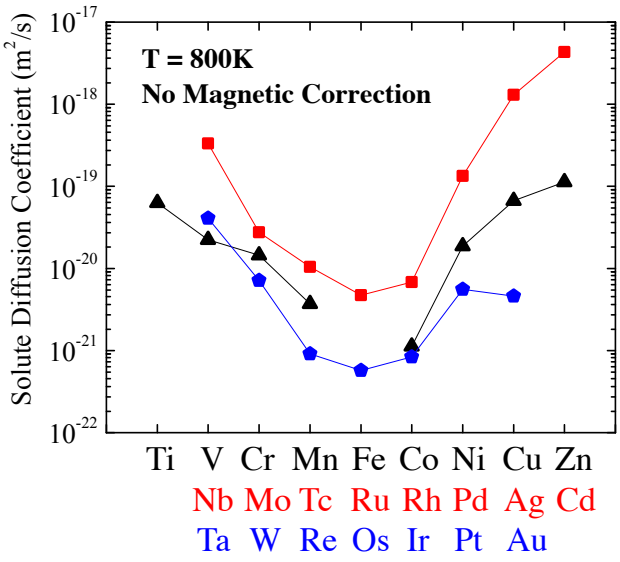

Figure 3.23: Solute diffusivities in bcc Fe calculated at $T = 800$ K, neglecting corrections for magnetic disorder.

this species. The work of Zhang *et al.* [169] has shown that conventional density functional theory calculations with semi-local approximations to the exchange-correlation energy are less accurate in describing Au, and a nonlocal term within the exchange correlation function is required to obtain accurate energetics. From Figure 3.21, we would expect the "slow diffusers" to be the 3*d* solute Co, and 5*d* solutes Re, Os and Ir, which in general have the diffusion coefficient lower than other solutes by at least a factor of five.

3.4.5 Comparison with Experimental Measurements

Though Figure 3.23 presents the basic trends of the solute diffusion coefficients in each transition metal series, to compare the absolute values of calculated diffusion coefficients with experimental measurements, it is necessary to know the value of α for each solute as shown in Equation 3.19. The value of α is a species-dependent parameter which quantifies the dependence of Q on magnetization. For several solutes, the values of α have been derived through fitting of the relationship between $T \ln [D/D_0^P]$ and $S^2(T)$ from the diffusion data over temperature ranges spanning the paramagnetic and ferromagnetic states. Given the value of α, along with computed D^F and D_0 and experimentally measured values of $s^2(T)$ [134, 170], the temperature dependence of the corresponding solute diffusion coefficients can be directly obtained, which allows a direct comparison between the calculated and measured diffusion coefficients.

We notice most experimental diffusion coefficient measurements for the transition metal solutes in bcc Fe focused on 3*d* transition metal series, while only for six solutes (Ti, Cr, Co, Ni, Cu and Zn), experiments have performed detailed study on the magnetic effects on solute diffusivity and reported the value of α. In addition, there are another three 4*d*

transition metal solutes (Nb, Mo and Ag) with one more $5d$ transition metal solute W where experimentally fitted values of α have been reported. In Ref. [1] a comparison between the calculated diffusion coefficients obtained with nominally the same computational framework and experimental measurements for Mo and W is presented. Therefore, in what follows, we will focus on comparisons for the other solutes.

$3d$ Transition Metal Solutes

For Ti-solute diffusion in bcc Fe, to our best knowledge, there is only one set of experimental data available for comparison. The measurement in Ref. [171] made use of high-purity Fe with large grain sizes and isotope concentration analysis is used to measure diffusion depth profiles as a function of time over the temperature range of 948 to 1174 K. Fitting of the experimentally measured values for the Ti-solute diffusion coefficient yields Q^P = 3.03 eV, D_0 = 2100 cm^{2}s^{-1} and α = 0.078, as summarized in Table 3.12 along with the present calculation results. Our calculated values (Q^F = 2.13 eV and D_0 = 0.20 cm^{2}s^{-1}) are somewhat smaller than those obtained from the fits to experimental data, while other calculations reported by Murali *et al.* [172] also gave relatively smaller values as Q^P = 2.31 eV and D_0 = 0.01 cm^{2}s^{-1}. However, we notice that the work of Murali *et al.* did not consider the effect of magnetic disorder on diffusion activation energy which leads to a significant underestimation of Ti diffusivities in the high-temperature region.

Table 3.12: Calculated activation energies in the fully ordered ferromagnetic state (Q^F) and paramagnetic state (Q^P), along with solute diffusion pre-factors (D_0) for solute diffusion of Ti in bcc Fe in comparison with available published experimental measurements.

Solute	Reference	Q^F (eV)	Q^P (eV)	D_0 (cm^{2}s^{-1})
Ti	Present work	2.30	2.13	0.20
	Klugkist and Herzig [171]	3.03	2.91	2100

Using the experimentally obtained value of $\alpha = 0.079$, the calculated temperature dependence of Ti-solute diffusion coefficients is plotted in Figure 3.24, in comparison with the experimental measurements. At 1042 K, the reported experimental value of the Ti solute diffusivity is 2.94×10^{-16} m^{2}s^{-1}, which is in very good agreement with our calculated value of 2.13×10^{-16} m^{2}s^{-1} at the same temperature. Coincidently, a good agreement is also reached between our calculated diffusivities and the measurements in the temperature region of 948-1042 K within a factor of two. Nevertheless, our predictions underestimate the Ti-solute diffusion coefficients at higher temperature within a factor of four close to the highest temperature corresponding to the α (bcc) to γ (fcc) transition temperature $T_{\alpha-\gamma}$. Considering that smaller magnitudes of Q and D have been obtained from previous calculations [172] and the present work, as well as limited experimental data, further experimental investigations of Ti solute impurity diffusivities in bcc Fe would seem warranted.

Next, regarding Cr-solute diffusion measurements, three different deposition methods, namely, dried salt solution, vapour deposition and electroplating method, were used by Bowen and Leak [173], Braun and Feller-Kniepmeter [174] and Lee *et al.* [175], respectively,

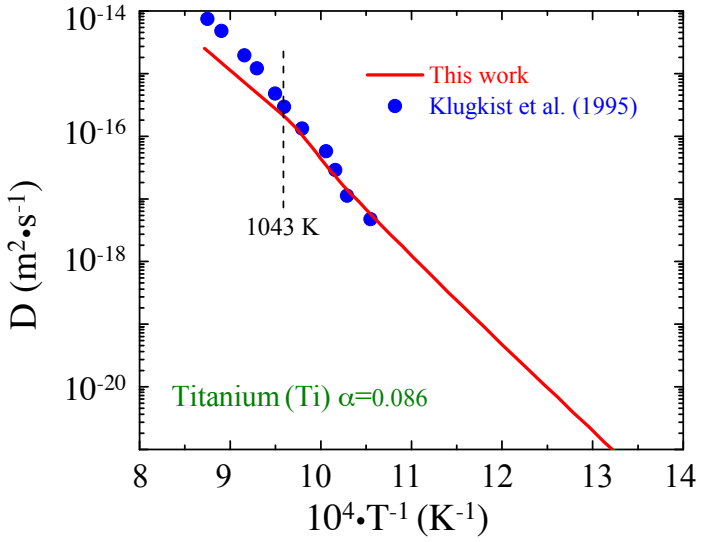

Figure 3.24: Diffusion coefficients of Ti calculated in the present work in comparison with available experimental data. In this plot and those that follow, the Curie temperature for bcc Fe (T_C = 1043 K) is indicated.

to prepare the isotope layers. For radioisotope diffusion depth profiles, early work done by Bowen and Leak [173] and Braun and Feller-Kniepmeter [174] made use of a residual activity method, while later work from Lee *et al.* [175] employed a radio-frequency sputter-microsectioning method. Their measured diffusion activation energies in the paramagnetic state Q^P range between 2.60 and 3.83 eV, as listed in Table 3.13. However, the large value of Q^P = 3.83 reported from Braun and Feller-Kniepmeter [174] coupled with a value of D_0 = 1690 cm^{2}s^{-1}, which is significantly larger than the normal values of D_0 ranging between 10^{-1} and 10^{+2} cm^{2}s^{-1}. A recent fit of the experimentally measured diffusion coefficients done by Lee *et al.* [175] suggested the value of α = 0.133. This value yields an estimation of Q^P = 2.35 eV from the present calculations of Q^F for Cr solute diffusion in bcc Fe, which is relatively smaller than experimental measurements. In terms of the value of D_0, our calculations yield values similar to those reported by Bowen and Leak [173], which are much smaller than other two values reported from experimental measurements. Considering the scatter between experimentally measured D_0 and Q^P, it is more meaningful to compare the overall diffusion coefficients, instead of simply the parameters derived from fits to experimental data.

Figure 3.25 compares the experimentally measured Cr solute diffusivities in bcc Fe with the present calculated results. We notice that all these available experiment measurements yield similar values for Cr-solute diffusion coefficients in the high temperature region, while the value reported by Lee *et al.* [175] is somewhat smaller than that from Braun and Feller-Kniepmeter [174] by a factor by up to five at the lowest temperature of 915 K. Though a generally smaller value of diffusion activation energy is estimated from our calculations, we found our calculated diffusion coefficients are still in good agreement with measurements

Table 3.13: Calculated activation energies in the fully ordered ferromagnetic state (Q^F) and paramagnetic state (Q^P), along with solute diffusion pre-factors (D_0) for solute diffusion of Cr in bcc Fe in comparison with available published experimental measurements.

Solute	Reference	Q^F (eV)	Q^P (eV)	D_0 (cm^2s^{-1})
Cr	Present work	2.66	2.35	8.55
	Bowen and Leak [173]		2.60	8.52
	Braun and Feller-Kniepmeter [174]		3.83	1690
	Lee [175]	3.14	2.77	37.3

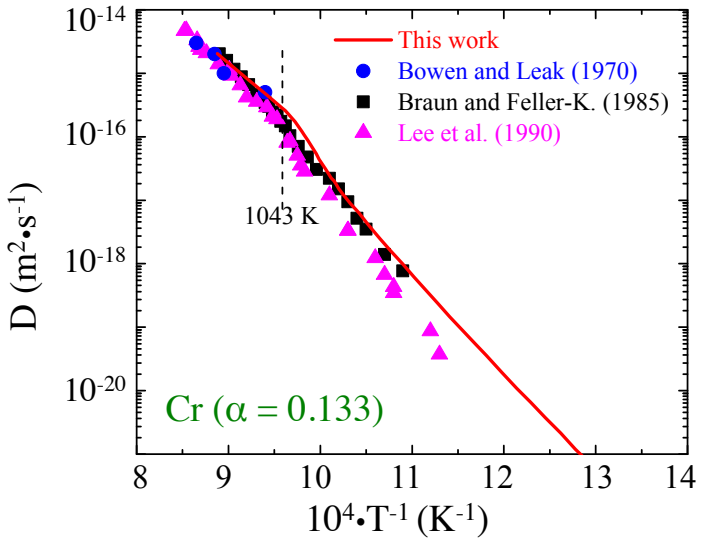

Figure 3.25: Diffusion coefficients of Cr calculated in the present work in comparison with available experimental data.

of Lee *et al.* [175] and Braun and Feller-Kniepmeter [174] in the high-temperature region. In the lower temperature region (below T_C), our calculated diffusion coefficients of Cr in bcc Fe are in somewhat better agreement with the values measured by Braun and Feller-Kniepmeter [174] with the maximal deviation corresponding to a factor of three at around 1020 K, which is slightly higher than the values reported from Lee *et al.* [175]. As we can see here, though there are some discrepancies of the Arrhenius parameters of D_0 and Q between our calculated and experimentally reported values, our predictions of Cr diffusion coefficients are in very reasonable agreement with the experimental measurements.

Further, computed Co solute diffusion coefficients in bcc Fe are compared with four sets of experimental measurements done by Borg and Lai [176], James and Leak [8], Hirano and Cohen [177] and Iijima *et al.* [178], as illustrated in Table 3.14 and Figure 3.26. Regarding the experimental measurement details, layers of radioactive Co were deposited onto coarse-grained Fe samples by vapor depositions [176] or by electroplating [8, 177, 178].

Residual activity measurements were employed for concentration measurement along the diffusion depth by Borg and Lai [176], James and Leak [8] and Hirano and Cohen [177], while the most recent report from Iijima *et al.* [178] made used of a radio-frequency sputtering method. A systematic analysis of the relation between $T \ln [D/D_0^P]$ and $s^2(T)$ was also done by Iijima *et al.*, leading to a value of $\alpha = 0.230$ for characterizing the effect of magnetic disorder on Co solute diffusion in bcc Fe [178], which is relatively higher than a direct estimation of $\alpha = 0.179$ based on the measured diffusion activation energy in paramagnetic Q^P and ferromagnetic Q^F states from the work of Hirano and Cohen [177]. Using the parameter of $\alpha = 0.230$, we obtain a value of $Q^P = 2.37$ eV from our calculated value of $Q^F = 2.92$ eV, which is much lower than the experimentally reported values in the range of 2.60-2.96 eV. It is noteworthy that our calculated value of D_0 is about one order of magnitude larger than the most recently published results from James and Leak [8], Hirano and Cohen [177] and Iijima *et al.* [178], while it is smaller than that from much earlier measurements done by Borg and Lai [176].

Table 3.14: Calculated activation energies in the fully ordered ferromagnetic state (Q^F) and paramagnetic state (Q^P), along with solute diffusion pre-factors (D_0) for solute diffusion of Co in bcc Fe in comparison available with published experimental measurements.

Solute	Reference	Q^F (eV)	Q^P (eV)	D_0 (cm^2s^{-1})
Co	Present work	2.92	2.37	25.10
	Borg and Lai [176]		2.96	118
	James and Leak [8]	2.70	2.66	6.38
	Hirano and Cohen [177]		2.42	1.83
	Iijima *et al.* [178]	3.20	2.60	2.76

From Figure 3.26 we can see that the experimental measurements of Co diffusion coefficients in the paramagnetic state of bcc Fe at high temperature are comparable to each other, while the measurements from Hirano and Cohen [177] gave relatively smaller values. In the ferromagnetic state of bcc Fe in the temperature region, the experimental results show much more scatter. Specifically, experimental measurements from Hirano and Cohen [177] at a temperature around 900 K are almost one order of magnitude higher than that measured by Iijima *et al.* [178]. Due to the large value of $\alpha = 0.230$, our calculated diffusion activation energy in the paramagnetic state is much smaller than those derived from experiments, which leads to the general overestimation of our calculated Co-solute diffusion coefficients in bcc Fe over the whole temperature range in comparison with most experimental measurements. In particular, at the highest temperature, close to $T_{\alpha-\gamma}$, our predicted diffusion coefficient of Co is higher than experimental measures by a factor of four while the maximal deviation occurs around the T_C where the calculated diffusion coefficient is almost an order of magnitude higher than the recent report from Iijima *et al.* [178]. In the ferromagnetic state, our calculated diffusion coefficients are closer to the values reported from Hirano and Cohen [177], but higher than other reported values.

Regarding Ni solute diffusion in bcc Fe , the impurity diffusion coefficients were first evaluated by Hirano *et al.* [179] using a residual activity method for measuring the isotope

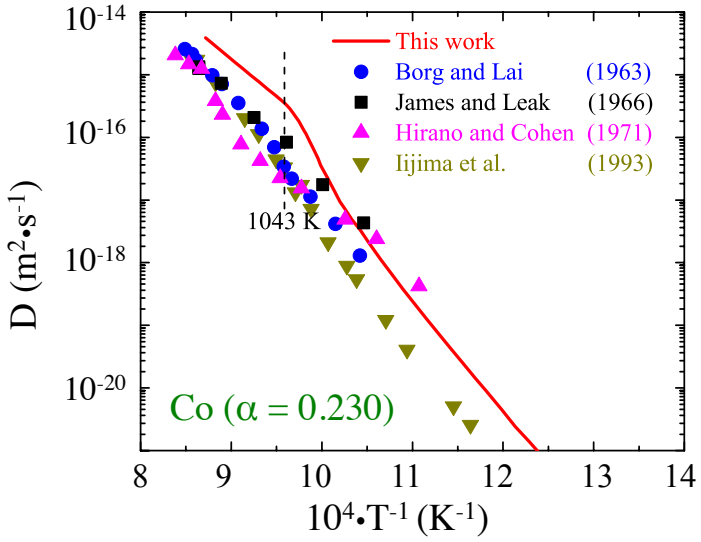

Figure 3.26: Diffusion coefficients of Co calculated in the present work in comparison with available experimental data.

concentration of the annealed sample with electroplated Ni radioisotope layers. Later work done by Borg and Lai [180] and Čermák [181] instead made use of a vapor deposition method for preparing the original samples. A summary of the temperature dependence of Ni solute diffusion coefficients in bcc Fe yields a fitted value of $\alpha = 0.120$ to best describe the effect of magnetic disorder. As shown in Table 3.15, this value of α yields the values of $Q^P = 2.41$ eV and $D_0 = 1.21$ cm^{2}s^{-1} from our calculations, which are close to the results derived from measurements of Hirano *et al.*: $Q^P = 2.43$ eV and D_0= 1.3 cm^{2}s^{-1}. However, these values are relatively smaller than those from Borga and Lai [180] and Čermák [181], respectively.

Table 3.15: Calculated activation energies in the fully ordered ferromagnetic state (Q^F) and paramagnetic state (Q^P), along with solute diffusion pre-factors (D_0) for solute diffusion of Ni in bcc Fe in comparison available published experimental measurements.

Solute	Reference	Q^F (eV)	Q^P (eV)	D_0 (cm^{2}s^{-1})
Ni	Present work	2.70	2.41	19.72
	Hirano *et al.* [179]	2.55	2.43	1.3
	Borg and Lai [180]		2.68	9.9
	Čermák *et al.* [181]		2.60	2.3

A comparison between the present calculations of Ni solute diffusion coefficients with experimental measurements is shown in Figure 3.27. A good agreement between our predictions and experimentally measured values of diffusivities can be seen in the paramagnetic state, with our calculations being between the experimental measurements with

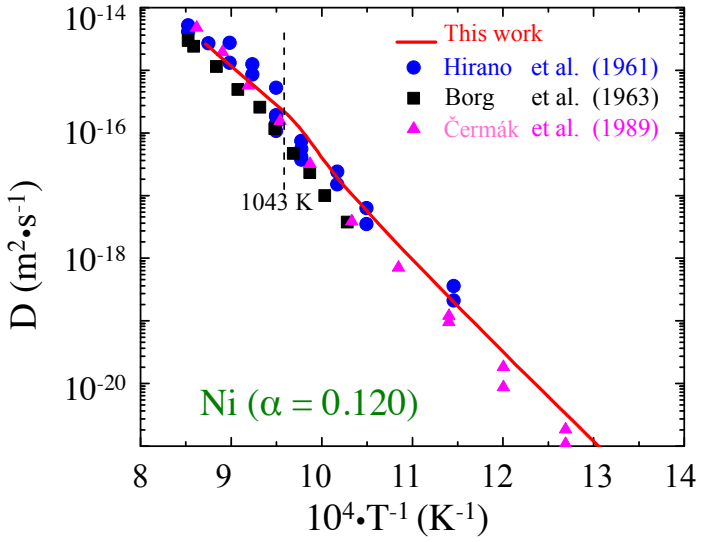

Figure 3.27: Diffusion coefficients of Ni calculated in the present work in comparison with available experimental data.

the upper bound from Hirano *et al.* [179] and lower bound from Borg and Lai [180]. In the lower temperature region, our predicted diffusivities are closer to the earlier measurement in Ref. [179], which are in general higher than those from Borga and Lai [180] and Čermák [181] by a factor of five. The discrepancies could originate from the difference of grain sizes in the Fe samples, the accuracy of the instruments as well as surface stress effects as discussed in Ref. [181].

We next focus on the Cu-solute diffusion. Our calculated results and four sets of solute diffusion Arrhenius parameters are presented in Table 3.16 and Figure 3.28. All of the measurements made use of vapor deposition methods to prepare the sample for the radioactive Cu radioisotope layers, while for the diffusion depth measurement, different techniques have been used, such as a weigh difference method [182], residual activity method [183] and electron probe microanalysis [184, 185]. With a relatively short penetration plot, the Cu solute diffusion coefficients earlier obtained by Anand and Agarwala [182] are smaller than other measurements at high temperature region above T_C by a factor up to five. A present fitting over all experimental measurements gives the value of $\alpha = 0.09$. Using this value, we can estimate the value of $Q^P = 2.22\ eV$ from our calculations, which is generally smaller than the reported values in the range of 2.52-2.94 eV from experimental measurements. Our calculated value of $D_0 = 1.21\ \mathrm{cm^2 s^{-1}}$ for Cu diffusion is of the same order of magnitude as the results derived from Ref. [182, 184, 183], whereas it is significantly smaller than the value reported by Sajie and Feller-Kniepmeter [185].

The comparison between our calculated Cu diffusion coefficients in bcc Fe shows excellent agreement with the most recently published experimental results in the paramagnetic phase, whereas an overestimation in comparison with the measured values in the ferromagnetic state by no more than a factor of five is obtained. The overestimation may

Table 3.16: Calculated activation energies in the fully ordered ferromagnetic state (Q^F) and paramagnetic state (Q^P), along with solute diffusion pre-factors (D_0) for solute diffusion of Cu in bcc Fe in comparison with available published experimental measurements.

Solute	Reference	Q^F (eV)	Q^P (eV)	D_0 (cm^2s^{-1})
Cu	Present work	2.42	2.22	1.21
	Anand and Agarwala [182]	2.57	2.51	0.57
	Speich *et al.* [184]		2.59	8.6
	Rothman *et al.* [183]		2.52	3.35
	Sajie and Feller-Kniepmeter [185]		2.94	300

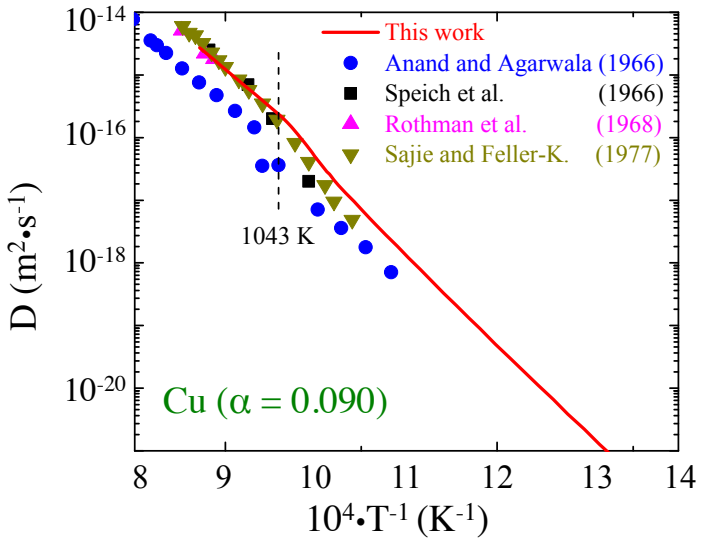

Figure 3.28: Diffusion coefficients of Cu calculated in the present work in comparison with available experimental data.

be due to he smaller diffusion activation energy we obtained from calculations.

The last 3*d* transition metal solute considered here is Zn. For Zn-solute diffusion in bcc Fe, the measurements in Ref. [186] made use of single crystalline Fe and solute diffusivities were measured by tracer analysis over the temperature range of 848-1169K, employing electron probe microanalyis techniques. The corresponding diffusion activation energies in the ferromagnetic and paramagnetic states, along with the diffusion prefactor derived from the work are listed in Table 3.17. Also a fit of the temperature dependence of diffusion coefficients spanning over the ferromagnetic and paramagnetic states suggests a value of $\alpha = 0.120$ [187] to account for the effect of magnetic disorder on Zn-solute diffusivities in bcc Fe. We found the calculated quantities display values much smaller than those obtained from experiments, in particular, the calculated D_0 for Zn in the present work is two orders of magnitude smaller than the reported values.

Table 3.17: Calculated activation energies in the fully ordered ferromagnetic state (Q^F) and paramagnetic state (Q^P), along with solute diffusion pre-factors (D_0) for solute diffusion of Zn in bcc Fe in comparison available published experimental measurements.

Solute	Reference	Q^F (eV)	Q^P (eV)	D_0 (cm^2s^{-1})
Zn	Present work	2.23	2.01	0.13
	Richter and Feller-Kniepmeter [186]	3.01	2.72	60

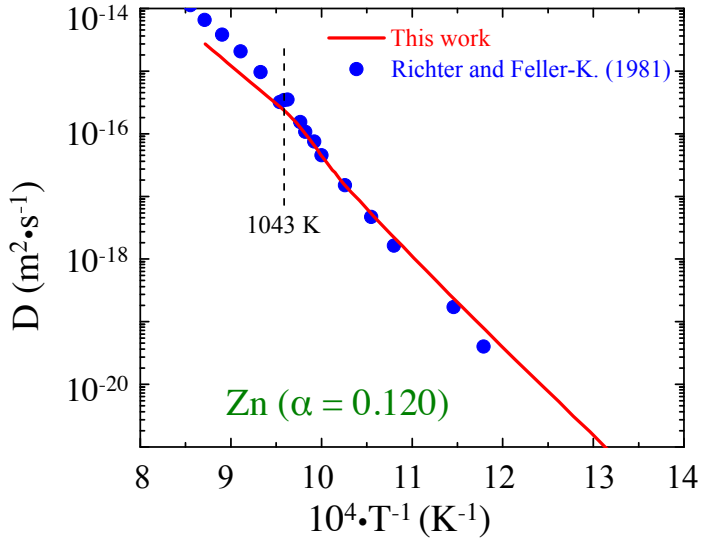

Figure 3.29: Diffusion coefficients of Zn calculated in the present work in comparison with available experimental data.

The calculated temperature dependence of the solute-diffusion coefficients for Zn is plotted in Figure 3.29, in comparison with the experimental results from Richter and Feller-Kniepmeter [186]. At 1043 K, the reported experimental value of the Zn solute diffusivity is 3.45×10^{-16} m^2s^{-1}, which is in excellent agreement with our calculated value of 2.35×10^{-16} m^2s^{-1} at the same temperature. The calculated diffusion coefficients of Zn in bcc Fe show overall good agreement with the experimentally measured values in the ferromagnetic phase, while they are relatively smaller than the measurements in the paramagnetic phase, with at most a factor of four at the highest temperature.

4*d* **Transition Metal Solutes**

Eight 4*d* transition metal solute (Nb-Cd) diffusion coefficients in bcc Fe have been examined in this work. The solute impurity-diffusion coefficients were experimentally measured for Nb, Mo and Ag. Previous calculations in Ref. [1] using nominally the same computational framework have been shown to be in a good agreement with experimental measurements for Mo. Hence, we will focus here on the other two solutes, namely, Nb and

Ag.

For solute species Nb, the solute impurity diffusion coefficient measurements of Geise and Herzig [188] made use of a microtome to obtain the concentration profile along the diffusion depth covering the temperature range of 993-1162 K, and subsequent experiments done by Herzig *et al.* [189] presented the results in the lower temperature range of 833-1000 K. The diffusion coefficients they reported are relatively higher than the values given by Oono *et al.* [190], which made use of an electroplating method for preparing samples for annealing and ion-beam sputter-microsectioning method for measuring isotope concentration. Also, an in-depth analysis on the magnetic disorder effect of Nb-solute diffusion was done by Oono *et al.* [190], giving a value of $\alpha = 0.061$ from a fit to the diffusivity data. Based on this value of α, we obtain the value of $Q^P = 2.05$ eV from the calculated Q^F in the present work. It is shown in Table 3.18 that this calculated value of Q^P is somewhat smaller than the values obtained by Geise and Herzig [188] and Oono *et al.* [190]. It is worth noticing that the most recent results from Oono *et al.* yielded an anomalously large value of $D_0 = 1400$ cm^{2}s^{-1} [190], which would require further detailed investigation. The D_0 obtained in the present calculation is also smaller than the experimentally reported value by Geise and Herzig [188].

Table 3.18: Calculated activation energies in the fully ordered ferromagnetic state (Q^F) and paramagnetic state (Q^P), along with solute diffusion pre-factors (D_0) for solute diffusion of Nb in bcc Fe in comparison with available published experimental measurements.

Solute	Reference	Q^F (eV)	Q^P (eV)	D_0 (cm^{2}s^{-1})
Nb	Present work	2.17	2.05	0.16
	Geise and Herzig [188]		2.61	50.2
	Heizig [189]	2.87		
	Oono *et al.* [190]	3.29	3.10	1400

The experimental measurements of Nb-solute diffusion coefficients show significant scatter, where almost an order of magnitude difference exists between the measurements from Heizig *et al.* [189] and Oono *et al.* [190]. It is of interest that though our Arrhenius parameters show poorer agreement with experiments, the predicted diffusion coefficients still are in good agreement with the values measured by Oono *et al.* in the paramagnetic state. Also the calculations in the ferromagnetic state yield the diffusion coefficients between the values obtained by Heizig *et al.* and Oono *et al.*. Such a significant discrepancy between experiments for the Nb diffusivity in bcc Fe warrants further investigation and study.

The diffusivity measurements for Ag have been undertaken by Bondy *et al.* [191] and Eguchi *et al.* [192] in the temperature range of 973-1173 K. Bondy *et al.* [191] made use of vapor deposition and radioactive isotope tracers with serial sectioning method, while Eguchi *et al.* [192] made use of electroplated samples with the diffusion depth measured by residual activity methods. Based on the diffusion activation energies in the paramagnetic ($Q^P = 2.68$ eV) and ferromagnetic state ($Q^F = 2.88$ eV) from the work of Eguchi *et al.*, we can estimated a value of $\alpha = 0.072$. Our calculated values of $Q^P = 1.94$ eV and $D_0 = 0.17$ cm^{2}s^{-1} are relatively smaller than the values obtained from experiments, as shown

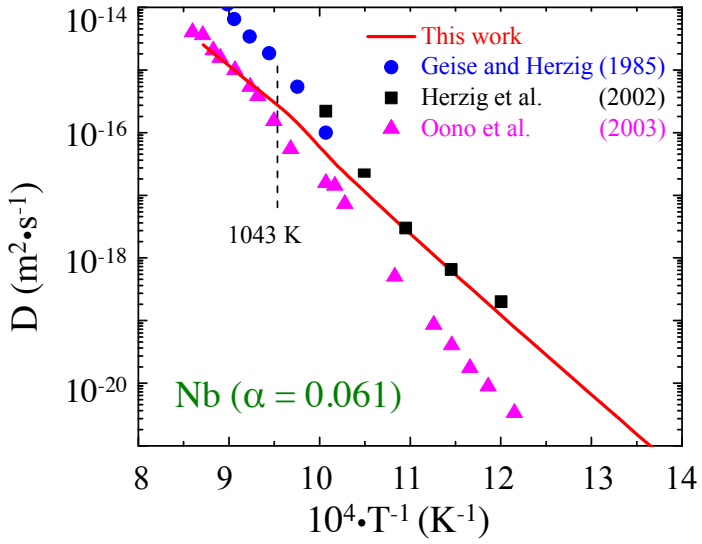

Figure 3.30: Diffusion coefficients of Nb calculated in the present work in comparison with available experimental data.

in Table 3.19. Collectively, our predicted diffusion coefficients over the temperature range are comparable with the experimental measurements. The values of Ag-solute diffusion coefficient we predicted in the paramagnetic state are between the measurements done by Bondy *et al.* and Eguchi *et al.*. In the ferromagnetic state, the calculated values are slightly higher than the results from Eguchi *et al.* by a factor of up to three.

Table 3.19: Calculated activation energies in the fully ordered ferromagnetic state (Q^F) and paramagnetic state (Q^P), along with solute diffusion pre-factors (D_0) for solute diffusion of Ag in bcc Fe in comparison with available published experimental measurements.

Solute	Reference	Q^F (eV)	Q^P (eV)	D_0 ($\mathrm{cm^2 s^{-1}}$)
Ag	Present work	2.08	1.94	0.17
	Bondy *et al.* [191]		2.99	1950
	Eguchi *et al.* [192]	2.88	2.68	38

3.4.6 Discussion and Summary

With aid of the solute-dependent parameter α to account for the effect of magnetic disorder on solute diffusion activation energy obtained from experiments, we have computed the transition metal solute diffusion coefficients within a framework combining density-functional-theory calculations, harmonic transition-state theory, and the Le Claire nine-frequency model. Combining the reported work in Ref. [1] using nominally the same computational approach, the agreement between the predicted and experimentally measured

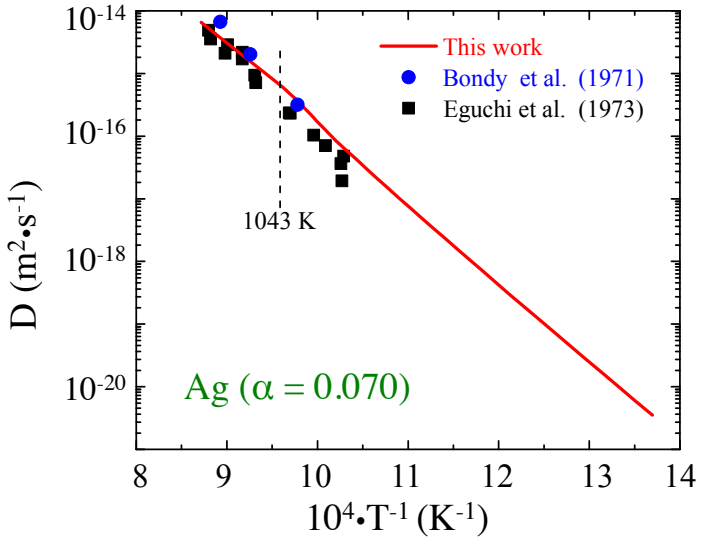

Figure 3.31: Diffusion coefficients of Ag calculated in the present work in comparison with available experimental data.

results over the relevant temperature range is highly encouraging, where our predicted and measured solute diffusion coefficients, for most solutes, are found to agree within a factor of five in the temperature range 800-1184 K, spanning a temperature range through the Curie temperature $T_c = 1043$ K.

For solute species Cr, Ni and Ag, very good agreement between our calculated diffusion coefficients and values reported from experimental measurements are observed over the whole temperature range of interest. For Ti and Zn, our prediction is close to the experimental measurements in the low-temperature ferromagnetic state. However, for both solutes, there is only one set of data reported by experiments and more experimental measurements would be desirable. For Cu, Mo and W-solutes, better agreement between calculated and measured temperature-dependent diffusion coefficients are presented in the high-temperature paramagnetic state, while our predictions overestimate the measured values by no more than a factor of five in the ferromagnetic state. The largest deviations from our predictions in comparison with experimental measurements occur for the solute Co. Our calculations yield an overestimation by almost one order of magnitude at T_c for Co-solute diffusion coefficients, and the calculated results are generally higher in comparison with experimental measures in the high temperature region. Also we found significant differences between experimental measurements for the Nb-solute diffusion coefficient results, while our calculated results are between them. A summary of the calculated results, as the ratios of the solute diffusivities to the self-diffusivity of Fe at a representative temperature of 1000 K, are plotted in Figure 3.32

For the solutes considered here, the value of α employed is based on the fit of experimental data over temperature ranges spanning the paramagnetic and ferromagnetic states. Given these values, it has been suggested [19] that there is a linear correlation

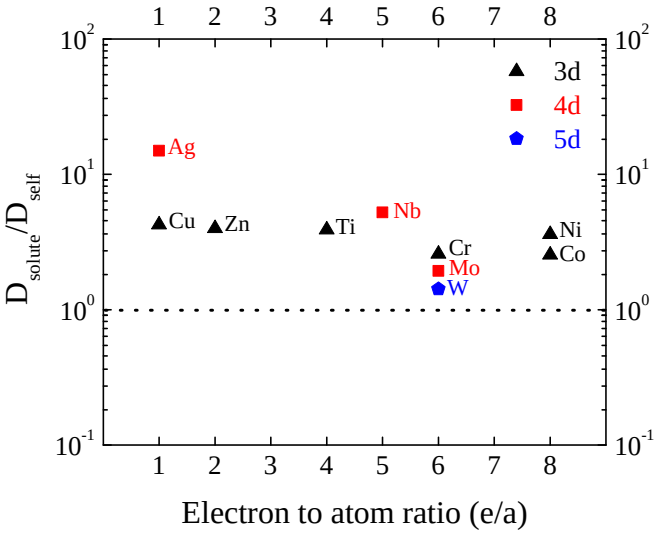

Figure 3.32: Calculated ratio of solute diffusion coefficient relative to self diffusivities in bcc Fe plotted for a variety of transition metal solutes as a function of electron to atom ratio at 1000 K. The black triangle, red square and blue pentagon correspond to $3d$, $4d$ and $5d$ transition metal solutes, respectively.

between the magnitudes of α and ΔM_{12}, the sum of the change in the local magnetic moments induced on the Fe atoms in the first- and second-neighbor shells of a solute atom:

$$\Delta M_{12} = \sum_{i=1}^{8} \Delta M_i^{1st} + \sum_{i=1}^{6} \Delta M_i^{2nd} \tag{3.24}$$

In Figure 3.33 the results for measured values of α for self- and solute (Ti, W, Nb, Mo, Cr and Co) diffusion are plotted with green circle symbols, versus the calculated values of the quantity ΔM_{12} defined in Equation 3.24. The dashed line represents the linear relationship suggested by Iijima [19] as: $\alpha = 0.057\Delta M_{12} + 0.159$. Nevertheless, we found that the reported values of α for Zn, Cu and Ni, which are plotted with red triangle symbols in Figure 3.33, do not match well such an empirical relation. We conclude that this linear relation cannot be generalized for obtaining the values of α for solutes with filled d shells, to predict the temperature dependence of solute diffusion coefficients.

The "spin-wave" approach was presented in Section 3.3, and shown to yield good predictions for the effect of magnetic disorder on self diffusion in bcc Fe. Some preliminary investigations have been performed by the authors and collaborators to further study the effect of magnetic disorder on solute impurity diffusion. It is noteworthy that the "spin-wave" approach is designed to account for the so-called transverse fluctuations for the magnetic systems, in which the Heisenberg model would be a good approximation for the spin-spin interactions. However, the approach is not designed to account for longitudinal fluctuations, where the magnitude of the local spin moment of each atom changes in the magnetically disordered system. We have found that in most cases the presence of a solute

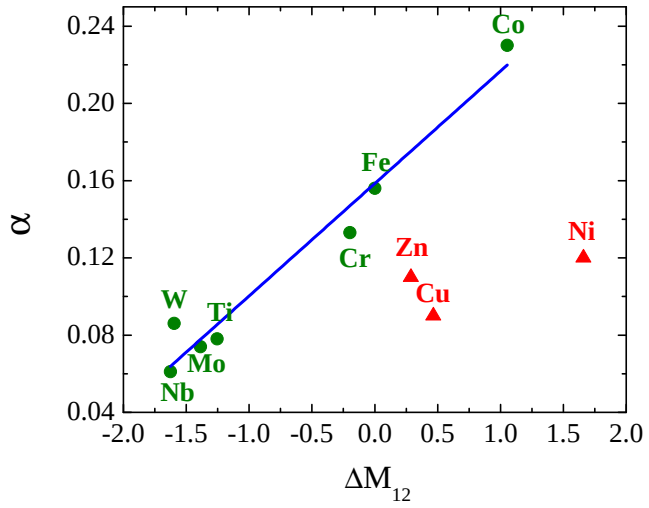

Figure 3.33: The linear relationship between α and ΔM_{12} suggested in Ref. [19]. The green circle symbols represent solute follow the linear relation, while the red triangle symbols represent solute do not satisfy the relation.

atom gives rise to a significant coupling between longitudinal and transverse fluctuations, which would significantly affect the magnetic interactions in these systems. Figure 3.33 demonstrates that the presence of solute and vacancy disturbs the local magnetic structure of the systems, and our preliminary calculations using the spin-wave approach suggest that longitudinal fluctuations contribute strongly to the changes in energy arising from magnetic disorder in the presence of solutes. The situation is found to be further complicated by the large coupling between local magnetic moments and structural relaxations in many cases. To progress further in the first-principles description of the effects of magnetic disorder on solute diffusion would thus require a methodology for treating transverse and local longitudinal fluctuations on an equal footing.

Although such a first-principles method has not yet been developed, Figure 3.21 shows the general trends of solute diffusivities in bcc Fe based on calculated diffusion activation energy Q and D_0 in the fully ordered ferromagnetic state, which could be used to estimate the solute diffusivities in the low temperature region. The calculated diffusion coefficients show clear trends versus atomic number featuring minimum values at the center of the transition metal series. In particular, the solute species Co, Re, Os and Ir appear to be potential candidates as "slow diffusers" in bcc Fe. Therefore, these solute species may be of interest as potential additions to precipitation-strengthened ferritic alloys for slowing high-temperature coarsening rates.

Furthermore, it is noteworthy that the present diffusivity calculations have not considered the solutes with significant size mismatch with Fe. Preliminary calculations for both La and Y solutes have led to interesting qualitative differences, relative to the transition-metal solutes considered before, in the nature of the vacancy-solute interactions.

We focus here on Y, which has been studied previously in both Fe and Ni-Al alloys due to its role in oxide-dispersion strengthening in the former, and its effects on corrosion resistance in the latter [193, 194].

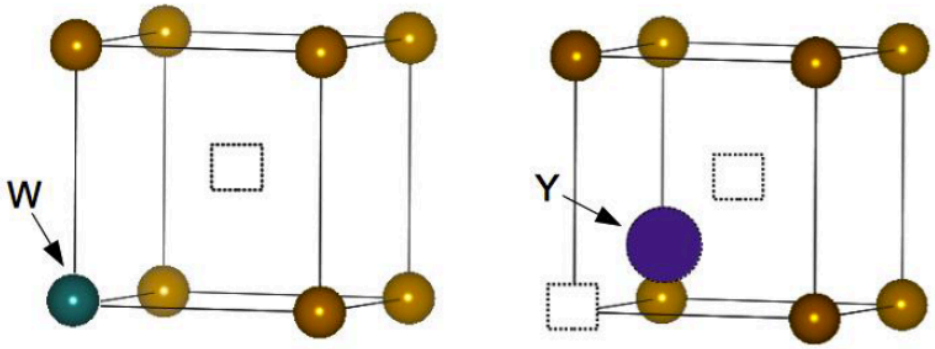

Figure 3.34: Comparison of the stable geometries for solute-vacancy nearest-neighbor pairs in the case of W and Y solute in bcc Fe.

.

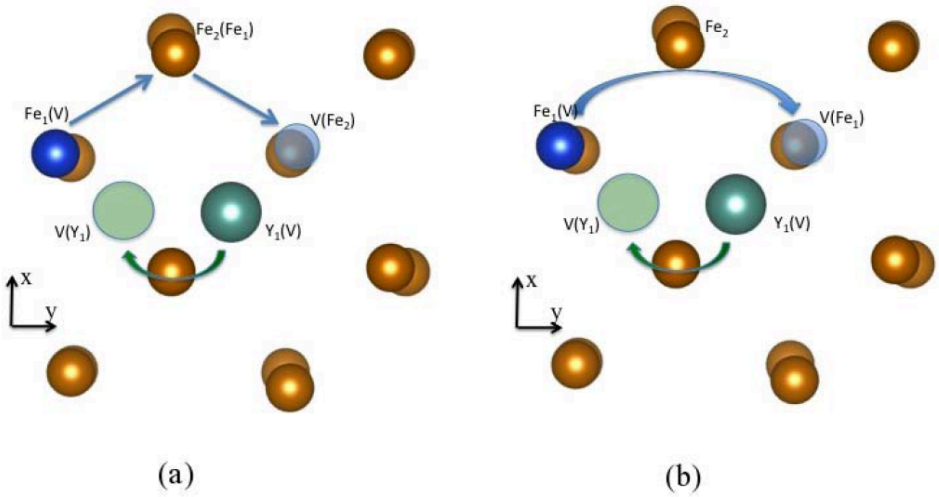

Figure 3.35: Ring-like diffusion mechanism for Y in bcc Fe. The parentheses are used to distinguish the location of the different species before and after Y diffusion.

Figure 3.34 contrasts the results obtained for Y-vacancy interactions in bcc Fe with the more typical case of a W solute. In the case of W, the solute is stable at a position very near the ideal bcc Fe-substitutional site, and a solute-vacancy hop involves overcoming a saddle-point barrier located half-way between the solute and vacancy sites. In contrast, an Y solute placed next to a vacancy is strongly bound in the interstitial position, as illustrated in Figure 3.34. Thus, the position that is a saddle point for the vacancy-solute exchange in the case of W becomes a deep energy minimum in the case of Y. This trend implies a much

more complex solute diffusion mechanism for Y solute.

To further investigate the mechanism for diffusion of an Y solute in bcc Fe, we performed a set of calculations investigating plausible pathways. The hopping of an Y solute to a neighboring position requires the motion of both the solute and a neighboring Fe atom. The motion of an Fe atom is required in order for one of the two vacancies, illustrated by boxes in Figure 3.34, to jump to a second neighbor position and remain a nearest-neighbor to the hopping Y atom. Two such mechanisms have been considered and are illustrated in Figure 3.35. In both diffusion pathways, the Y diffuses between two nearest-neighbor interstitial sites, but Figure 3.35 (a) involves only nearest-neighbor hops of the Fe atoms, while Figure 3.35 (b) describes a jump of the Fe atom between second-neighbor sites. The migration energies of the two possible diffusion pathways using nudged elastic band calculations are approximately 3.43 and 3.59 eV, respectively. The complex ring-like diffusion mechanisms and high migration energy imply potentially very low diffusivity of Y atoms in the bcc Fe.

These initial computational results strongly suggest that it would be worthwhile to produce some initial Fe-based alloys with Y solute added, to investigate experimentally where the Y ions are located in the microstructure and whether they do indeed slow down the coarsening rate of the precipitates. Due to their high energy in the Fe matrix, these atoms may segregate to the precipitate core, the precipitate/matrix interface, or other extended defects such as dislocations or grain boundaries. In the first case, the dissolution of a small precipitate to enable the growth of a larger one in coarsening would involve the transport of the Y through the matrix. In this case, the slow diffusion of Y is expected to dramatically reduce the coarsening rate. In the second case, the Y impurities may provide strong pinning of the interfaces, such that coarsening becomes limited by the interface mobility, rather than the solute diffusion through the matrix. Initial exploratory experimental investigations of precipitation-strengthened ferritic alloys with Y additions would help identify which of these different possibilities may occur, and would help guide further computational work related to the use of Y or related rare-earth atoms as a potential means for improving the high-temperature stability of the alloys considered in our work.

3.4.7 Summary

A computational framework has been described for modeling self and impurity solute diffusion in bcc Fe. The effect of magnetic disorder on bcc Fe self diffusion was studied using a density functional theory based approach coupled with the "spin-wave" formalism. The results showed excellent agreement between calculations and experimental measurements. Transition metal solute impurity diffusivities in bcc Fe also have been studied in detail. Competing effects of diffusion activation energies and prefactors have been demonstrated. For transition metal solutes, both quantities exhibit maximum values in the center of the transition metal series. Calculations suggested solutes Co, Re, Os and Ir as slow-diffusing solutes in bcc Fe which is desirable for optimization of coarsening rates for precipitation-strengthened ferritic alloys operating at high temperatures. Also the calculated diffusion coefficients for most solutes are shown to be comparable to experimental measurements, such that the computational approach outlined above may be useful for helping to guide further development of kinetic databases for Fe-based multicomponent

alloys.

3.5 Point Defects in Intermetallic Phases

One issue that arises in the use of precipitation-strengthened ferritic alloys for high-temperature applications is the creep resistance of the ordered intermetallic phases that form the precipitates in the bcc Fe matrix. If these materials themselves have low creep resistance, they may not be effective in pinning dislocations at high temperatures.

The topic of creep resistance of ordered intermetallic phases is one that has been actively investigated for several decades. First-principles computational methods are of interest in this context, as they provide a framework for computing the density of point defects and other properties that relate to creep strength. To help further the design of intermetallic-strengthened ferritic alloys, we have initiated the work to develop automated tools for computing equilibrium point defects in intermetallic compounds. The tools will be described in detail in Appendix A. In this section we present results representing applications of these tools in the study of intermetallic phases relevant to the ferritic alloys that motivated an effort covered in this chapter.

3.5.1 Computational Details

In what follows we will compute equilibrium point-defect concentrations within the dilute-solution thermodynamic formalism. Since the details of the thermodynamic formalism are presented in Appendix A, here we give only the computational details surrounding the calculations of defect formation energies based on density-functional theory.

The required point-defect calculations were performed within the generalized gradient approximation of Perdew, Burke and Ernzerhof (PBE) [58] using the Projector Augmented Wave (PAW) method [83, 84] as implemented in the Vienna ab initio simulation package (VASP) [153, 154, 155, 156]. A value of 400 eV is used for plane-wave cutoff [84] and a Monkhorst-Pack sampling [157] of reciprocal space, with k-point grids equivalent to 12×12×12 for a conventional B2 unit cell were employed. The non-defect (pristine) structures were fully relaxed with conjugate gradient method. The point-defect structures were obtained by relaxing atomic positions of structure with lattice constants derived from the pristine structure optimizations. The convergence criteria for energy and forces in the self-consistent iterations and structure optimizations, respectively, were set to 10^{-5} eV and 10^{-2} eV/Å.

3.5.2 Intermetallic Equilibrium Defect Concentration

The B2-NiAl crystal structure is isomorphic to CsCl with Ni and Al each occupying one sub-lattice as shown in Figure 3.36 (a). Adopting conventional notation for point defects, there are two vacancy defects, i.e. V_{Ni} and V_{Al}, and two antisite vacancy defects, i.e. Ni_{Al} and Al_{Ni}, respectively, where the subscript denotes sublattice site. Calculated equilibrium concentrations of these point defects at the temperature of T = 1000 K are shown in Figure 3.37. As the composition changes from Ni to Al rich, the dominant defect changes from Ni_{Al} antisite to V_{Ni} constitutional vacancies. The concentrations of these two

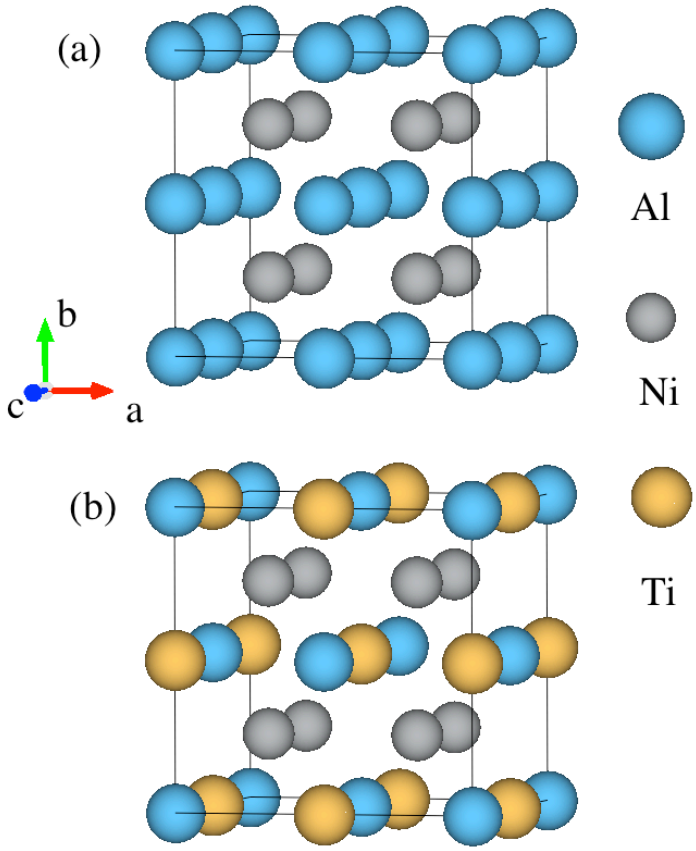

Figure 3.36: Crystal structures of (a) B2-NiAl and (b) $L2_1$-Ni_2AlTi.

defects are at least one order of magnitude larger than the other two defects. Our calculated results agree well with experimental observations from Bradley and Taylor [195] where it was reported that excess Ni would form Ni_{Al} while excess Al is achieved through the creation of V_{Ni}. The relative order of the magnitude for the four defect concentrations as found in with previous calculations from Korzhavyi *et al.* [196] and Mishin [197], while the reported values of defect concentrations as a function of stoichiometry are qualitatively consistent with previous calculations to within an order of magnitude. The difference between calculations may be associated with the choice of pseudopotentials, supercell size and relaxation schemes.

In the alloy design effort that motivated this work, Ti additions to the ferritic alloys have been found to lead to changes in microstructure and properties. Specifically, such additions have been shown to give rise to the formation of precipitates with the ordered $L2_1$ Heusler phase based on composition Ni_2AlTi [198, 199].

The $L2_1$ structure for Ni_2AlTi has three sets of sublattices, as shown in Figure 3.36 (b). It has cubic space group $Fm\bar{3}m$ (space group No. 225) where the Ni atoms occupy the Wyckoff positions A (0, 0, 0) and C (1/2, 1/2, 1/2), and the Al and Ti atoms occupy B (1/4, 1/4, 1/4) and D (3/4, 3/4, 3/4), respectively. Calculated equilibrium point defect

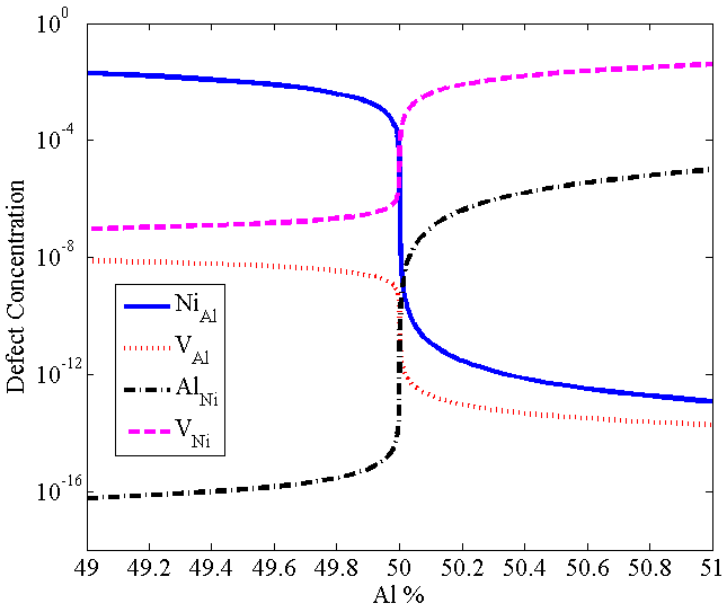

Figure 3.37: Equilibrium constitutional and thermal defect concentrations in B2-NiAl at T = 1000 K.

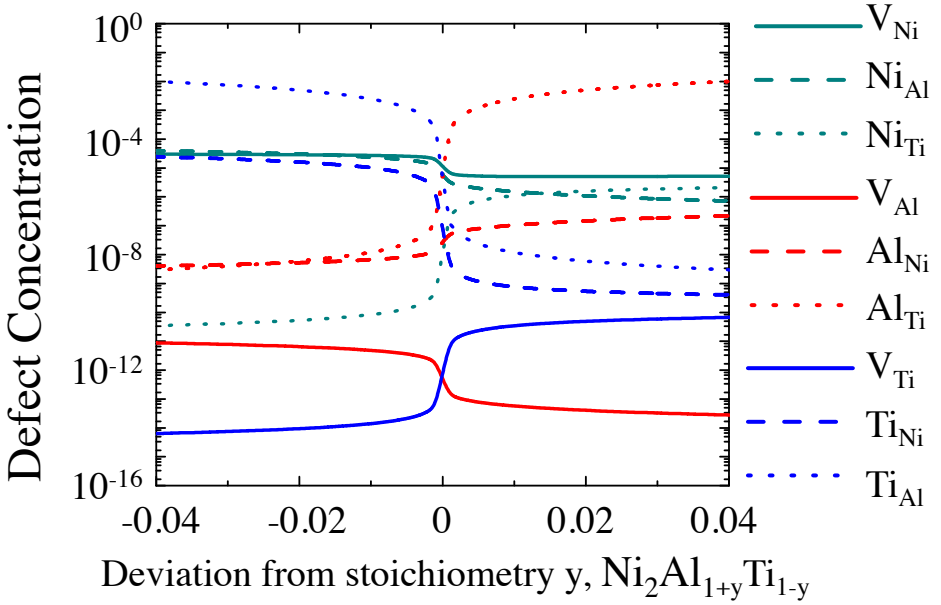

Figure 3.38: Equilibrium constitutional and thermal defect concentrations in $L2_1$ (a) Ni_2AlZr and (b) Ni_2AlHf at T = 1000 K.

concentrations at the temperature of T = 1000 K as a function of composition are plotted in Figure 3.38. It is known experimentally [198, 199] that this $L2_1$ phase can accommodate significant deviations in Al and Ti concentrations, while the Ni mole fraction is fixed at 50 at.%. We thus consider point-defect concentrations for compositions $Ni_2Al_{1+y}Ti_{1-y}$. For both Ti- and Al-rich compositions the majority defects are found to be antisites, rather than vacancies.

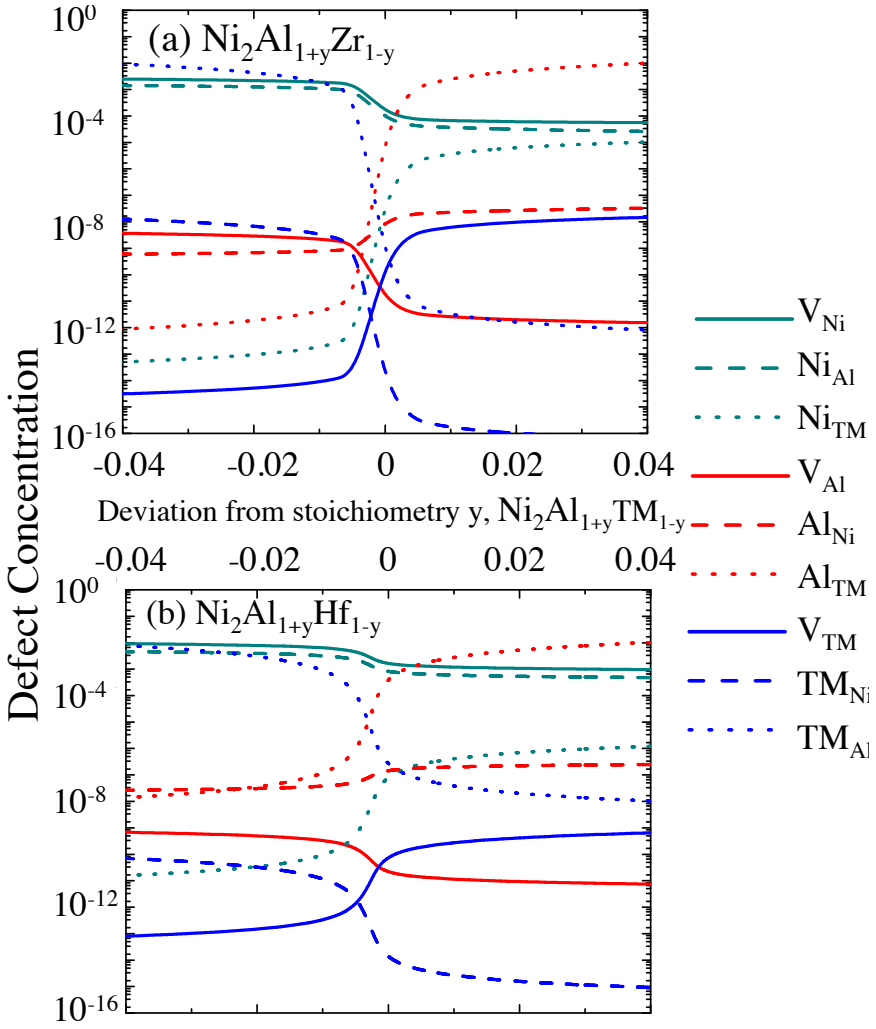

Figure 3.39: Equilibrium constitutional and thermal defect concentrations in $L2_1$-Ni_2AlTi at T = 1000 K.

We also performed similar calculations for the $L2_1$ (Ni_2AlTM) structures with other group III elements (TM = Zr or Hf), in order to find the basic trends of defect properties for alloy design. The defect concentrations as a function of composition at the temperature of T = 1000 K are shown in Figure 3.39. We find both elements give rise to a significant increase of V_{Ni} defect concentrations (by at least an order of magnitude), which could potentially lead to increased diffusion kinetics in the precipitates relative to Ni_2AlTi.

Chapter 4

First-pinciples Modeling of Electron Diffusion: Polaron diffusion in α-MoO_3

4.1 Forward

In this chapter, we focus on the electronic diffusion in α-MoO_3. This study was motivated by the current development of α-MoO_3 for energy storage and transport applications [200, 36, 201, 202, 203], such as Li-ion battery and electrochemical supercapactiors.

α-MoO_3 possesses a layered crystal structure, in which the MoO_3 two-dimensional bilayer sheets are bonded by electrostatic and van der Waals interactions. The latter are known to be a challenge to accurately describe by conventional density functional theory methods that are based on local or semi-local exchange-correlation potentials [204, 205]. Furthermore, like other transition metal oxide semiconductor, the kinetics of Faradaic charge transfer and the electron transport in α-MoO_3 is known to be slow [206, 44, 36]. In this case, modeling of bulk crystalline α-MoO_3 system, in order to unravel the underlying electronic structure and transport properties, would be of importance for optimizing material design and improving device performances.

It is the purpose of the present work to understand these material properties of interest using computational approaches. Density functional theory based first-principles methods are employed to study bulk α-MoO_3. The remainder of this chapter is organized as follows. In Section 4.2, we employ different first-principles methods to study the atomic and electronic structures of α-MoO_3. Section 4.3 focuses on the electronic diffusion through a small-polaron mechanism in α-MoO_3, followed by studying the effect of polaron-lithium binding in Section 4.4, in order to understand the electronic conductivity of the material. Conclusions of the present study are presented in Section 4.5

Content in Section 4.2, including the figures and tables, were partially published by Hong Ding, Keith Ray, Vidvuds Ozolins and Mark Asta in Phys. Rev. B, 85 (2012), 012104 [207], and is reproduced here with permission of the co-authors and publishers.

Content in Sections 4.3.2 and 4.4, including the figures and tables, were partially

4.2 Atomic and Electronic Structure

4.2.1 Introduction

To study the electronic diffusion in any semiconductor, first and foremost, it is important to understand its atomic structure. As shown in Figure 4.2.1, the crystal structure of α-MoO_3 has a unique layered structure. It is composed of sheets of distorted, edge-shared MoO_6 octahedra. Each octahedron contains three symmetry-distinct oxygen ions, which occupy 4*c* Wyckoff positions in the *Pbnm* orthorhombic space group [209]. The MoO_3 sheets are stacked along the *b* lattice direction of the orthorhombic unit cell, and are weakly bonded across a region commonly referred to as the "van-der-Waals gap".

Due to the technological interest in α-MoO_3, it has been the topic of several previous theoretical studies, based on electronic density-functional theory (DFT) within the local-density (LDA) [210] and generalized-gradient (GGA) approximations [211], GGA plus Hubbard-U corrections for onsite Coulomb interactions [212], and Hartree-Fock (HF) with a DFT-based correction for electron correlation [213]. Theoretical calculations and X-Ray photoemission experiments [214], establish a mixed ionic and covalent character for the Mo-O bonding within the sheets, characterized by a strong degree of hybridization between Mo 4*d* and O 2*p* electrons [215]. The interactions between the MoO_3 sheets are governed by both electrostatic and van der Waals (vdW) contributions as discussed in Ref. [216].

Due to the fact that vdW interactions are not accurately described by traditional GGA and LDA calculations, the equilibrium spacing between the MoO_3 sheets is not accurately predicted by these methods (see below). For studies of the electronic-structure and bonding properties of α-MoO_3, a practical solution to this problem has been to fix the *b* lattice constant at the experimentally measured value [214, 217]. This approach is not feasible, however, for computational studies of defects and processes where large variations in the interlayer spacing may arise. An example is lithium-ion intercalation, where variations in Li content are coupled with large expansions in the interlayer spacing [218, 200]. For applications of this type, a method with computational efficiency comparable to DFT is required, which accurately characterizes both the equilibrium bond lengths and bond stiffnesses of the host α-MoO_3 compound. In the present work we assess the accuracy of recently proposed vdW corrected DFT-based methods for this purpose, through a comparison between theoretical results and experimental measurements for equilibrium lattice constants, bond lengths.

4.2.2 Computational Details

Several approaches have been developed for describing van der Waals interactions within the framework of DFT [219]. In the present work we focus on two classes of approaches that feature computational requirements comparable to traditional DFT methods. The first is the DFT-D approach [61], in which the contribution to the totally energy

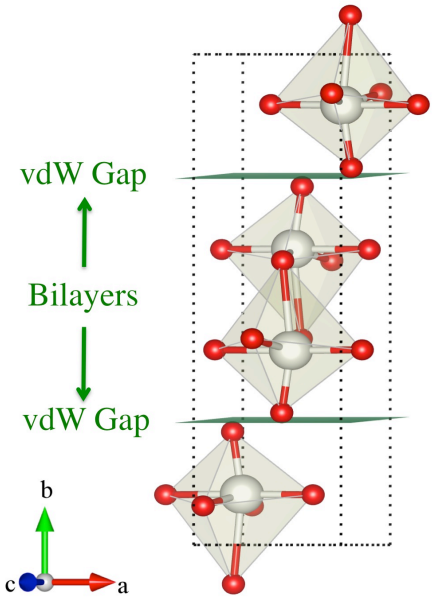

Figure 4.1: Structure of the orthorhombic α-MoO_3 compound. (a) Mo (white) and O (red) octahedra are illustrated, as well as the vdW gap (green layer).

associated with dispersion interactions is described by a classical pair potential with the C_{ij}/R_{ij}^6 form. Three generations of the method have been developed [63], using different approaches for calculating the C_{ij} coefficients. The first uses an average of empirical coefficients from different hybridization states for each atom, while in the second (DFT-D2), the PBE0 hybrid method [220] is used to obtain atomic ionization energies and polarizabilities in the determination of C_{ij}. In both methods these coefficients are obtained from mixing rules, using values tabulated in terms of the chemical identity of the atoms i and j alone. The DFT-D3 method makes use of time-dependent DFT [63] to calculate the C_{ij} coefficients through the averaged dipole polarizability as a function of frequency. Furthermore, it interpolates between results for different local environments to capture differences due to bonding geometry. In this method the C_{ij} coefficients are derived taking into account structural information as well as the chemical identity of the atoms.

The second class of approaches considered in this work is the so-called van der Waals density functionals (vdW-DF) [65], in which the vdW contribution to the total energy is described through modifications to the correlation energy functional within DFT. Specifically, the DFT exchange-correlation functional is divided into three parts: $E_{xc} = E_{lc} + E_{nl} + E_x$, where E_{lc} is a local correlation energy described within the local density approximation, E_{nl} is the nonlocal correlation energy, and E_x is a semi-local exchange functional. The E_{nl} contribution is given by the integral: $E_{nl} = \frac{1}{2}\int d\mathbf{r}d\mathbf{r}'n(\mathbf{r})\phi(\mathbf{r},\mathbf{r}')n(\mathbf{r}')$, over electron densities, n at $\mathbf{r}$ and $\mathbf{r}'$, multiplied by an integration kernel, ϕ, which is derived from the adiabatic-connection theorem through a series of approximations [65]. We consider

three different exchange functionals for use with the vdW-DF approach, as reported in the literature. These are revPBE as in the original vdW-DF [65], PW86 as in vdW-DF2 [70], and optB88 [221], a new exchange functional based on the B88 exchange functional [222]. RevPBE and optB88 are both paired with the same E_{nl}, while the E_{nl} used with PW86 has a changed parameter which relates how the length scale in E_{nl} is set by a corresponding GGA calculation. In vdW-DF2 and vdW-DF this parameter comes from energy expansions appropriate for molecules or a slowly varying electron gas, respectively.

All the calculations performed in this work made use of the projector-augmented-wave (PAW) method[223, 224], as implemented in the Vienna ab initio simulation package (VASP)[153, 154, 155, 156]. The wavefunctions were expanded in a plane wave basis with an energy cutoff of 600 eV. For calculations of the structure of the MoO_3 compound we sampled the Brillouin zone employing a 7×5×7 mesh, using the Methfessel-Paxton scheme[225] with a smearing width of 0.1 eV. The PAW potentials employed in this work are those labeled "Mo" and "O" in the VASP PAW-PBE library. Internal coordinates were relaxed until energy and atomic forces converged to within 0.01 meV/atom and 0.005 eV $Å^{-1}$, respectively. The equilibrium lattice parameters were computed using conjugate-gradient minimization with the calculated stress tensors. Based on several numerical tests the convergence of the results presented below is estimated to be 0.02Å for a and c, 0.05Å for b. For the DFT-D calculations we employed the D2 method, with values of the dispersion coefficients (C_{ij}) given in Ref. [226], and a value of $s_6 = 0.75$. In the vdW-DF calculations we employed the VASP implementation developed by Klimeš *et al.* [227], which makes use of an algorithm for efficiently evaluating the integral for E_{nl} due to Pérez and Soler [66].

To better describe the electronic properties, DFT+U and hybrid-functional methods have been used previously to study α-MoO_3 [212, 228]. Herein, these two approaches are also employed to study the electronic properties with the lattice parameters fixed at experimentally measured values for pure α-MoO_3. The DFT+U calculations are based on the formalism of Dudarev *et al.*[229], in which the total energy of the system is expressed as:

$$E^{\mathrm{DFT+U}} = E^{\mathrm{DFT}} + \frac{U_{\mathrm{eff}}}{2} \sum_{\sigma} Tr[\rho^{\sigma} - \rho^{\sigma}\rho^{\sigma}], \tag{4.1}$$

where E^{DFT} corresponds in this work to the DFT energy in the Perdew-Burke-Ernzerhof (PBE) generalized gradient approximation [138, 230], ρ^{σ} denotes the spin (σ) dependent on-site density matrix, and the parameter multiplying the last term on the right-hand side of Equation 4.1 is defined as $U_{\mathrm{eff}} \equiv U - J$ in terms of the Hubbard-model U and J parameters. In the DFT+U calculations undertaken in this work, use was made of a value of $U_{\mathrm{eff}} = 6$ eV. This value is similar to that derived by Coquet and Willock ($U_{\mathrm{eff}} =$ 6.3 eV) [212] by comparing the results of periodic plane-wave DFT+U and wavefunction-based cluster calculations of oxygen defect formation on the (010) surface of α-MoO_3. The value of U_{eff} used here is, however, considerably smaller than that suggested by Lutfalla *et al.* [231] (8.6 eV) by fitting the experimental enthalpy for the hydrogen reduction reaction of MoO_3 to MoO_2: $MoO_3 + H_2 \rightarrow MoO_2 + H_2O$.

In the hybrid-functional calculations we employ the formalism developed by Heyd, Scuseria and Ernzerhof (HSE)[81, 232, 233], where the exchange-correlation energy (E_{xc}^{HSE06})

is formulated as:

$$E_{xc}^{\mathrm{HSE06}} = E_x^{\mathrm{DFT}}(\mu) + E_c^{\mathrm{DFT}} - \frac{1}{4}E_x^{\mathrm{DFT,SR}}(\mu) + \frac{1}{4}E_x^{\mathrm{HF,SR}}(\mu). \tag{4.2}$$

with E_x^{DFT} and E_c^{DFT} denote the exchange and correlation energies in DFT under the PBE-GGA. In this formalism 25% of the short-range part of the DFT exchange energy ($E_x^{\mathrm{DFT,SR}}(\mu)$) is replaced by the exact nonlocal Hartree-Fock exchange ($E_x^{\mathrm{HF,SR}}(\mu)$) evaluated with a short-range screened Coulomb kernel, where μ is an adjustable screening parameter determining the distance $2/\mu$ at which $E_x^{\mathrm{HF,SR}}$ becomes negligible. In this work, μ is set as 0.2 Å, which is the shortest screening distance recommended by Krukau *et al.*[234] for the HSE06 scheme.

4.2.3 Results

Atomic Structure

Table 4.1: A comparison of lattice constants (in the unit of Å) of α-MoO_3 calculated in the current and previous calculations, and measured experimentally. The asterisk superscript denotes calculated results where the b lattice parameter was fixed at the experimentally measured value.

Method		a	b	c
DFT	LDA[210]	3.73	13.04	3.48
	PW91[211]	3.97	14.67	3.72
	HF[213]	3.91	14.27	3.68
	PBE*[214]	4.02	13.86	3.76
DFT-D	DFT-D2	3.93	13.88	3.71
	DFT-D2+U	3.91	13.90	3.73
vdW-DF	vdW-DF	4.05	14.86	3.73
	vdW-DF2	4.04	14.69	3.75
	optB88	3.94	14.08	3.73
	optB88+U	3.91	13.96	3.77
Exp.	Ref. [235] (T=300 K)	3.962	13.860	3.697
	Ref. [236] (T=300 K)	3.963	13.865	3.693
	Ref. [236] ($T \to 0$ K)	3.958	13.750	3.700

Table 4.1 compares the current results for the equilibrium lattice constants with those obtained by DFT-based approaches in previous calculations and experimental measurements. The temperature-dependent experimental data reported in Ref. [236] shows an anomalously large thermal expansion coefficient for the b lattice parameter. In what follows, we will therefore assess the level of agreement between experiment and theory using the extrapolations of the measured lattice constant values to zero temperature presenting in

Ref. [236]. The LDA results, taken from Ref. [210], feature theoretical lattice constants that are smaller than these measured values by 6 percent for a and c, and about 5 percent for b, respectively. For calculations where the value of the b lattice constant is unconstrained, it is seen that GGA (PW91) predicts values for a and c that agree to within 1 percent of the measured values, while the calculated b lattice constant is roughly 7 percent larger. The Hartree-Fock based results from Ref. [213] give values that are 1 and 0.5 percent smaller than measured values for a and c, and 4 percent larger for b, respectively. Thus, the previous LDA, GGA and HF calculations give rise to predictions for the interlayer spacing that are accurate to no better than 4 percent in comparison with experimental measurements.

Table 4.2: Calculated Mo-O bond lengths (in units of Å) obtained by the DFT-D2 and optB88 based methods are compared with previous calculations and experimental results. The labeling of the bonds in the first column corresponds to the notation introduced in Figure 4.2.1.

	Calculation					Experiment	
	DFT-D2	DFT-D2+U	optB88	optB88+U	PBE+U	Ref. [235]	Ref. [236]
$d_{\text{Mo-O1}}$	1.70	1.69	1.70	1.70	1.69	1.68	1.63
$d_{\text{Mo-O2}}$	1.77	1.79	1.78	1.80	1.78	1.74	1.74
$d^*_{\text{Mo-O2}}$	2.19	2.18	2.19	2.17	2.21	2.25	2.24
$d_{\text{Mo-O3}}$	1.95	1.96	1.96	1.97	1.96	1.95	1.96
$d^*_{\text{Mo-O3}}$	2.40	2.39	2.39	2.39	2.38	2.31	2.30

We consider next the vdW-corrected DFT results obtained here. The PBE-based DFT-D2 method is seen to provide an excellent level of agreement with experiment for each of the three lattice constants, with the calculated values being 0.5 percent larger for a, 0.3 percent larger for c, and 1 percent larger for b. The vdW-DF results are found to vary significantly between the original vdW-DF implementation, and the vdW-DF2 and optB88 parametrizations.

The original vdW-DF functional gives lattice constants that are uniformly larger than the measured values, by 1, 4 and 0.7 percent for a, b and c, respectively. The vdW-DF2 approach leads to a slightly worse prediction for each of the lattice constants relative to the original vdW-DF. Of the three vdW-DFs considered in this work, the best level of agreement between experiment and calculations is obtained with the optB88 functional. This approach gives rise to predictions for a and c within 0.8 percent of measurements, and the b lattice constant is 2 percent larger than the experimental value. The improved accuracy of the optB88 functional obtained here for α-MoO_3 is similar to that found for metallic, covalent and ionically bonded solids in Ref. [227], where the improvements of the optB88 functional for solids relative to the original vdW-DF and vdW-DF2 methods is attributed to a smaller exchange enchancement factor for small reduced gradients.

Table 4.2 lists the bond lengths (bonding notations corresponding to Figure 4.2) obtained from the present calculations, previous calculations [214], and experimental measurements. The results obtained by the DFT-D2 and vdW-DF methods show excellent agreement with available experimental data, as well as previous PBE calculations, with the exception of $\mathrm{d}^*_{\mathrm{Mo-O_2}}$ and $\mathrm{d}^*_{\mathrm{Mo-O_3}}$ where the vdW-corrected calculations are smaller and

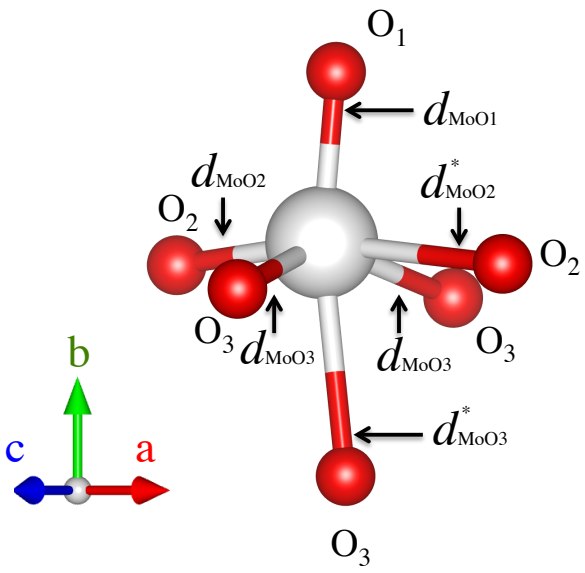

Figure 4.2: The geometry of a MoO_6 octahedron with symmetrically-distinct bond lengths labeled.

larger than measurements by approximately 0.06 and 0.09 Å, respectively.

The effects of parameters U in DFT+U calculations on lattice parameter and bond lengths are also shown in Table 4.1 and Table 4.2 for DFT-D2+U and optB88+U methods. These predicted quantities are in qualitative agreement with other calculations, showing that the Hubbard-U parameter mostly affects electronic structure of α-MoO_3, while having relatively small effects on the atomic structure. These two functionals will be used below to discuss the effects of cell-volume and cell-shape relaxations on the polaron-Li-ion bonding energies as presented in Section 4.4.2

Electronic Structure

The effects of U on atomic and electronic structure of α-MoO_3 have been evaluated here. Figure 4.3 shows calculated electronic density of states (DOS) for MoO_3 obtained in the present work using DFT+U and HSE06 methods. The results are qualitatively similar to each other and to previously published calculations [237, 238, 239, 217]. The results feature a conduction band with predominantly Mo 4*d* character and a valence band with states having primarily O 2*p* character near the Fermi level, and states with significant hybridization between O *p* and Mo *d* states at higher binding energies. Consistent with previous calculations, the value of the bandgap (E_g) of 2.09 eV computed by DFT+U is approximately ten percent larger than that derived by GGA-PBE calculations. The DFT+U calculations underestimate the experimentally measured band gap, which has been reported

to be in the range of band gaps (E_g) as listed in Table 4.3. Previously reported DFT-D2 and optB88 also yield nominally the same features of the electronic structure and band gap predictions.

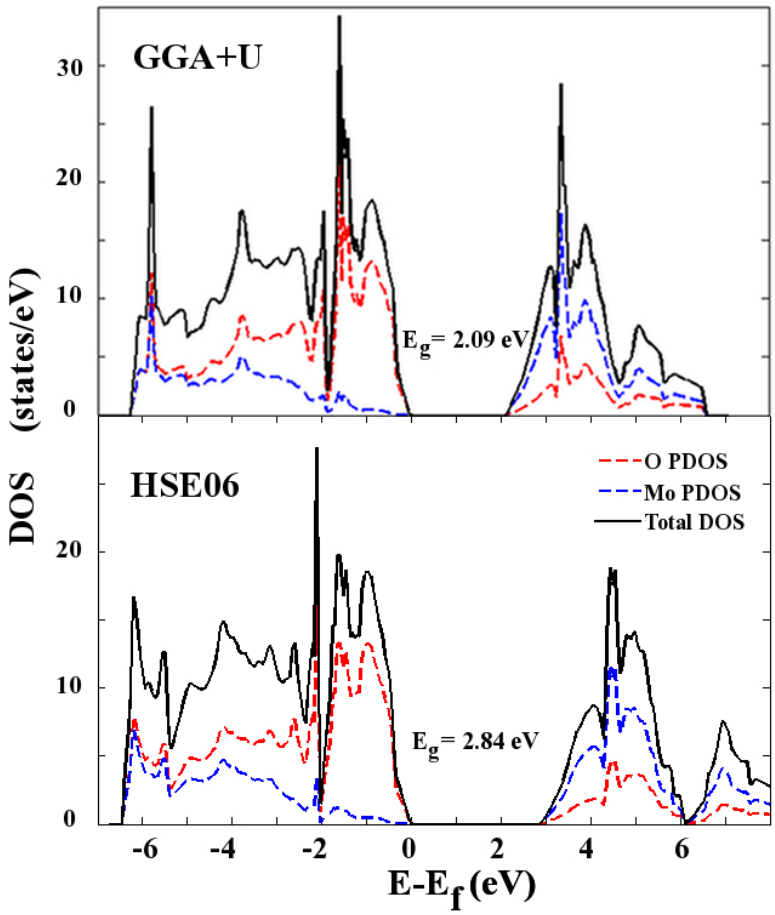

Figure 4.3: Comparison of projected density of states (per formula unit) of α-MoO_3 calculated by the DFT+U and HSE06 methods.

Table 4.3: Band gaps (E_g) of α-MoO_3 measured by experiments.

Reference	Method	E_g (eV)
Deb [240]	Electrical Conductivity	3.66
	Photoconductivity	3.56
Pandit *et al.* [241]	Electrical Conductivity	3.5
Kröger *et al.* [242]	Inverse Photoemission Spectroscopy	3.0
Juryska [243]	Optical Absorption	2.8
Itoh *et al.* [244]	Optical Absorption	3.87
Sabhapathi *et al.* [245]	Optical Absorption	3.25

While the shape and character of the states for the HSE06-computed DOS are very similar to those obtained with the DFT+U method, the band gap has a significantly larger value of 2.84 eV, which is closer to experimental measurements. In addition, the HSE06 functional predicts a larger valence-band width than DFT+U: 6.5 eV versus 6.3 eV, respectively; the HSE06 value is in better agreement with but still smaller than the value of 6.98 eV derived from the X-ray photoemission data of Itoh *et al.* [244].

4.3 Diffussion of Isolated Polarons

Due to its attractive electrochemical properties and layered crystal structure, α-MoO_3 has been investigated extensively as a Li-ion intercalation compound for energy storage applications. Recently, the interest in this compound for such applications has expanded due to the development of synthesis techniques for producing nanoscale and mesoporous forms of the material [246, 247, 36, 201, 248]. The high specific area achievable through such synthesis routes has led to enhanced performance in battery applications, as well as recent demonstrations of the successful use of this compound as an electrode material for electrochemical pseudocapacitors [37, 39]. For such applications, the performance of α-MoO_3 is limited by its intrinsically low electronic conductivity (σ_e), and a number of different strategies have been developed for improving this property, e.g., through oxygen reduction [249, 250], extrinsic doping [251, 252], and the development of composite material architectures [253, 254]. To guide such efforts, an expanded understanding of the intrinsic mechanisms underlying electronic transport in α-MoO_3, and the ways they can be influenced by variations in composition and structure, is desirable.

Depending on the synthesis procedure, intrinsic room-temperature electronic conductivities in α-MoO_3 have been reported to vary over several orders of magnitude, from values of $\sigma_e \approx 10^{-10}$ to $\sigma_e \approx 10^{-4}$ S·cm^{-1} [206, 44, 36]. Similarly large variations in σ_e can be effected through extrinsic doping. For example, in a recent investigation by Berthumeyrie *et al.* [45], dielectric spectroscopy techniques were used to study variations in the mechanisms underlying electronic transport in Li_xMoO_3 as a function of the Li content x. At room-temperature the measured values of σ_e were reported to vary from 10^{-10} to 0.46 S·cm^{-1} as x ranged from 0 to 0.45 in "classical powder" (CP) samples consisting of micron-scale particles, and from 3×10^{-6} S·cm^{-1} for $x = 0$ to 9×10^{-3} or 0.2 S· cm^{-1} (depending on crystallographic direction) for $x = 0.28$ in "nanobelt" (NB) samples. At the smallest lithium intercalation levels, electron diffusion were concluded to be governed by an adiabatic small polaron hopping mechanism in both samples, consistent with conclusions drawn from earlier studies of electron conductivity in pristine MoO_3[255]. With increasing values of x, the spectroscopy results of Berthumeyrie *et al.* suggest a transition from a dominant polaron mechanism to a bipolaron mechanism in the CP samples, which was not observed in the NB samples. The differences found between NB and CP samples were suggested to be due to an enhanced role of surface-related effects in the former.

To provide expanded insights into the electronic diffusion mechanisms in lithium ion intercalated α-MoO_3, we present the results of a computational study of the electronic mobilities of electron small polarons in this Section and their interaction with Li interstitial ions in Section 4.4. We employ both density-functional theory with Hubbard-U corrections

(DFT+U) [229, 256] and hybrid functional [81, 232, 233] methods to compute the orbital occupancies and atomic structural changes associated with small polaron formation, the activation energies for adiabatic polaron transfer, and the binding energies of electron small polarons to Li ions.

4.3.1 Computational Details

Calculations including polarons made use of a $3 \times 1 \times 3$ supercell containing 36 formula units (108 ions). In the DFT+U supercell calculations, the Brillouin-zone sampling was performed using a $3 \times 3 \times 3$ k-point grid in combination with the Methfessel-Paxton scheme [225] and a smearing of 0.1 eV.

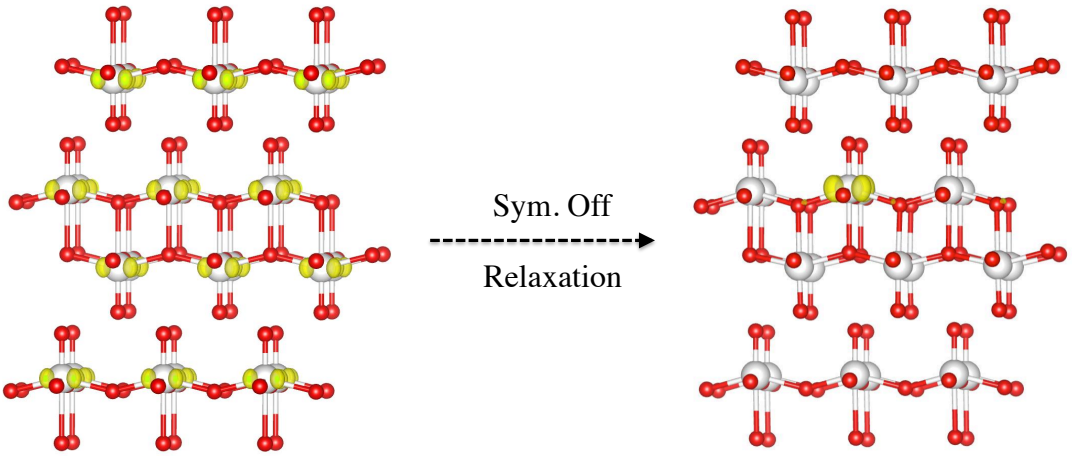

Figure 4.4: Illustration of the computational approach for obtaining an electron small polaron in the α-MoO_3 structure. The yellow isosurface corresponds to induced charged density due to the excessive electron in the system. Initially the excessive electron evenly delocalised on each Mo ions, while the relaxation without symmetry constraints leads to the localization of the electron to form a small polaron.

For hybrid-functional calculations the same size supercells were employed, but with a single k-point (Γ) used to sample the Brillouin zone. Several tests were performed to estimate the convergence of the DFT+U results with respect to supercell size, plane-wave cutoff and k-point density; these tests indicate that the polaron migration energies and the changes in bond length associated with polaron defect formation are converged with respect to these parameters to within a precision of approximately 0.02 eV and 0.03 Å, respectively.

The present computational study focuses on electron small polarons that result from the occupation of one of the unoccupied $4d$ orbitals in the Mo^{6+} ion, to form a Mo^{5+} ion. In the calculations, small polarons are formed through the introduction of an extra electron in the computational cell (with charge-compensating positive background charge).

Since it is possible for the electron forming the polaron defect to occupy different $4d$ orbital states, we undertook a detailed investigation of the preferred occupancy using an occupation matrix control (OMC) approach [257].

The formation of a polaron couples with the *local* structure distortion as illustrated in Figure 4.4, therefore, the symmetry of pristine α-MoO_3 is turned off during the relaxation procedures. For the DFT+U calculations, all atomic coordinates were relaxed until the forces on the ions were converged to within 0.01 eV/Å, holding the lattice parameters fixed at the experimentally-measured values, while for the hybrid calculations all atomic positions were fixed at the values obtained from the DFT+U relaxations.

For calculations of the adiabatic polaron migration energies, we employed the approach proposed by Maxisch *et al.* [258] and Ong *et al.* [259]. In this approach, energies are computed on the Born-Oppenheimer surface, for a set of configurations with atomic coordinates ($\{q\}$) linearly interpolated between those corresponding to the initial and final states, $\{q_i\}$ and $\{q_f\}$, respectively:

$$\{q_x\} = (1 - x)\{q_i\} + (x)\{q_f\}, \tag{4.3}$$

with x varying in the range from 0 to 1. For calculations of polaron migration energies away from intercalated Li ions, the initial and final states are equivalent by symmetry, such that the energy calculated for $x = 0.5$ in Figure 4.3 provides the estimate of the migration energy barrier. A schematic illustration of the approach is given in Figure 4.5.

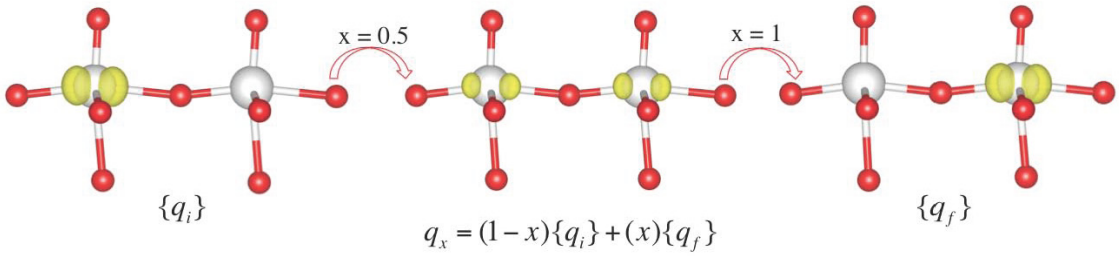

Figure 4.5: An illustration of the approach used to compute adiabatic polaron migrations energies from calculations on the Born-Oppenheimer surface for atomic coordinates linearly interpolated between those corresponding to polaron occupation on the left-most Mo ion and on the right-most Mo-ion.

4.3.2 Isolated Polaron

We consider the electronic and atomic structure associated with the formation of the electron small polaron defect, which will be referred to as a Mo^{5+} ion in what follows. Figure 4.6 shows the change in charge density associated with the formation of Mo^{5+} from the Mo^{6+} ion in bulk MoO_3. The shape of the added electron charge density is consistent with occupation in a state that has predominantly $4d_{xz}$ character, as confirmed from an analysis of projected densities of states.

From extensive tests performed with the occupation-matrix-control method referenced in the previous section, it was verified that occupancy of the $4d_{xz}$ orbital leads to the lowest energy for the Mo^{5+} ion in this structure. The defect state associated with this polaron defect is found to be highly localized; in the DFT+U calculations with U_{eff} = 6 eV this state sits at an energy approximately 1.5 eV below the conduction-band edge. The location of this defect state in the bandgap depends on the value of U_{eff} employed in the DFT+U calculations; the defect band moves approximately 0.2 eV lower (higher) in energy when U_{eff} increases (decreases) from 6 eV to 7 eV (5 eV).

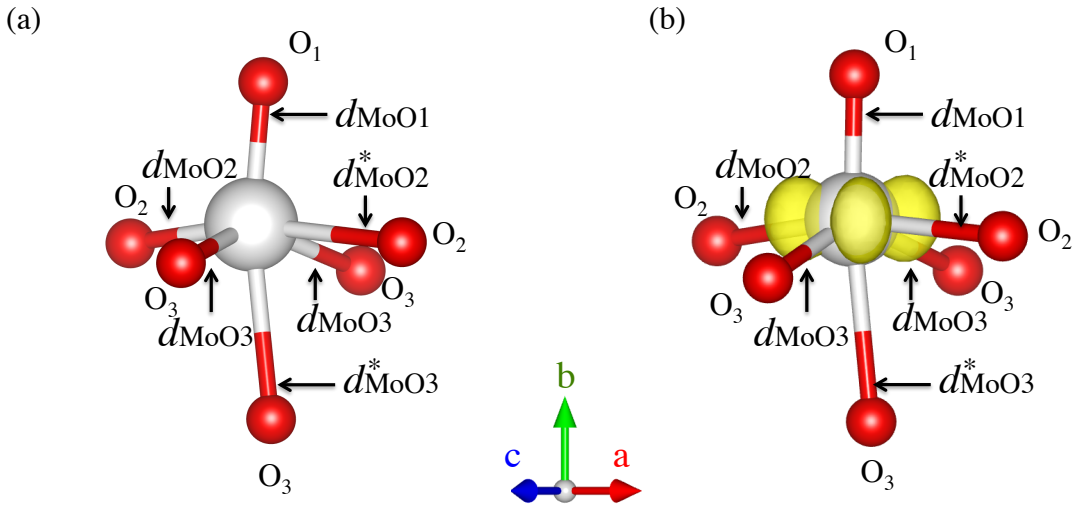

Figure 4.6: The geometry of a (a) pristine MoO_6 octahedron and (b) that with a localized electron small polaron on the Mo ion is illustrated; the yellow isosurface corresponds to induced charge density due to the electron small polaron, plotted at a value of the electron density equal to 0.025 eÅ^{-3}.

Table 4.4: DFT+U calculated Mo-O bond lengths (in units of Å) for Mo^{5+} and Mo^{6+} sites in α-MoO_3 are listed and compared with values reported in previous publications.

	Polaron site (Mo^{5+})	Nonpolaron site (Mo^{6+})
d_{MoO1}	1.67	1.69
d_{MoO2}	1.97	1.78
d^*_{MoO2}	2.20	2.21
d_{MoO3}	2.01	1.96
d^*_{MoO3}	2.40	2.38

Previous DFT and crystal field theory calculations have demonstrated that the ordering of the d-orbital energy levels for Mo^{5+} in the α-MoO_3 structure is highly sensitive to the nature of the structural distortions associated with the octahedral arrangement of the oxygen ions around the cation [260]. It is thus of interest to analyze the nature of the

bonding environment before and after the introduction of the polaron defect, as summarized in Table 4.4. In bulk α-MoO_3, there exist three symmetry-distinct oxygen-ion positions, labeled as O1, O2 and O3 in Figure 4.6, following the notation introduced by Corà *et al.* [237]. As a consequence, there are five different types of bonds in a given MoO_6 octahedron, labeled as: d_{MoO1}, d_{MoO2}, d^*_{MoO2}, d_{MoO3} and d^*_{MoO3}, respectively (see Figures 4.6 and 4.4). As shown in Table 4.5, the bonding for a bulk Mo^{6+} ion in MoO_3 is characterized by the formation of a relatively short bond with the terminal oxygen (O1), and relatively long bonds to two of the O2 and O3 ions.

Table 4.5 lists the bond lengths surrounding the polaron on the Mo^{5+} ion. The formation of this polaron defect leads to distortions of the bond lengths with neighboring oxygen ions. A comparison with the results for Mo^{6+} shows that the most pronounced bondlength distortion occurs for the corner-shared O2 ion. The main effect of polaron formation is to extend the length of the Mo-O2 (d_{MoO2}) bond, by approximately 0.2 Å, presumably due to the electrostatic repulsion between the charge in the d_{xz} orbital and the nearest-neighbor O2 ion in the *a*-*c* plane.

4.3.3 Diffusion Barriers of Isolated Polarons

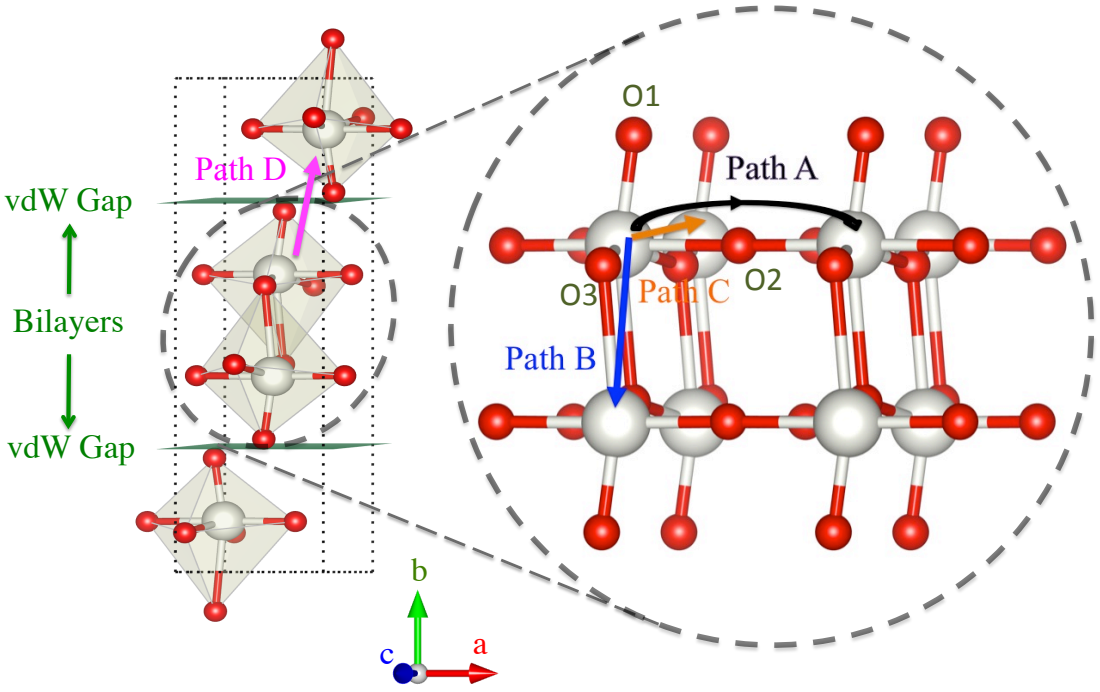

Figure 4.7: The structure of α-MoO_3 and the local geometry of the MoO_6 octahedra within the bilayer sheets. Also shown are three polaron hopping directions within the bilayer sheets for paths A (black), B (blue) and C (orange) and one path normal to the van der Waals gaps for path D (magenta).

Based on the stacking bilayer structure of α-MoO_3 through "van der Waals" gaps, we label four distinct paths for polaron diffusion to neighboring Mo sites in Figure 4.7. Path A involves a hop along the a crystallographic direction, to the nearest-neighbor Mo site within the same a-c plane in the bilayer sheet; the Mo ions on each side of this path are linked by a corner-shared oxygen ion, and are separated by a jump distance of 3.96 Å. Path C also connects two Mo ions within the same a-c plane that are linked by corner-shared oxygen ions, and involves a hop along the c direction by a shorter distance of 3.70 Å. Path B connects two Mo ions in different a-c planes within the bilayer sheets that are linked across the shared edge of neighboring octahedra; this path involves the shortest hop distance of 3.39 Å. We note that path B has been referred to in the literature as a "zig-zag" path [45] as it involves motion along the direction c and up and down along b direction within the bilayer sheet. Finally, path D involves polaron migration across the van der Waals gap along the b direction, with the largest hop distance of 4.96 Å.

Table 4.5: Polaron diffusion distances d (in units of Å) and the corresponding barriers ΔE (in units of eV) along different directions as labeled in Figure 4.7.

Path	d	ΔE	
		DFT+U	HSE06
A	3.96	0.17	0.11
B	3.39	0.42	0.21
C	3.70	0.23	0.35
D	4.96	0.51	0.48

Figure 4.8 shows the calculated energies along the migration paths defined by Equation 4.3 for each of the four jumps described above. The energy versus the reaction coordinate x obtained from the DFT+U calculations is plotted with solid symbols connected by lines. For comparison, the activation energy at the estimated saddle point sites computed by hybrid functionals are shown by open symbols. Comparing first the different calculated results, it can be seen that the HSE06 activation energies are consistently lower than those obtained by DFT+U, by up to 15 % in magnitude. A fraction of this difference originates from the different k-point sampling used in the DFT+U and HSE06 calculations. When the k-point grid for the DFT+U method is changed from $3 \times 1 \times 3$ to $1 \times 1 \times 1$ (as used in the HSE06 calculations), the calculated activation energy along path A is calculated to decrease by 0.02 eV; the remainder of the 0.06 eV difference between HSE06 and DFT+U results shown in 4.8 can thus be attributed to the different functionals. While the activation energies calculated by HSE06 are uniformly lower than those computed by DFT+U, the differences in calculated energies for other points along the reaction coordinate show no systematic trend. Specifically, the HSE06 values for the energies (relative to the binding state) at reaction coordinates of $x = 0.25$ and 0.75 for paths A and B are approximately 0.01 eV lower than the values from DFT+U, while for paths C and D they are up to 0.02 eV higher.

A major feature of the results shown in 4.8 is the high anisotropy in the activation energies along the different crystallographic directions, and it is important to note that the relative ordering of the activation energies for these different paths is predicted to be

the same by both DFT+U and HSE06 methods. The calculated results give the lowest energy barrier for hopping along path A, in the a crystallographic direction. The next lowest-energy hop is along path C, along the crystallographic c direction. Thus, polaron migration is predicted to be fastest between Mo ions that lie within the same plane of the bilayer sheet, which are all linked by corner-shared oxygen ions. Importantly, the path involving the shortest jump distance, namely the zig-zag path B, involves a significantly higher activation energy (by 0.1 to 0.2 eV) than migration along either paths A or C. The results thus suggest that the presence of a corner-shared oxygen ion significantly facilitates polaron migration, despite the larger jump distances for paths A and C relative to B.

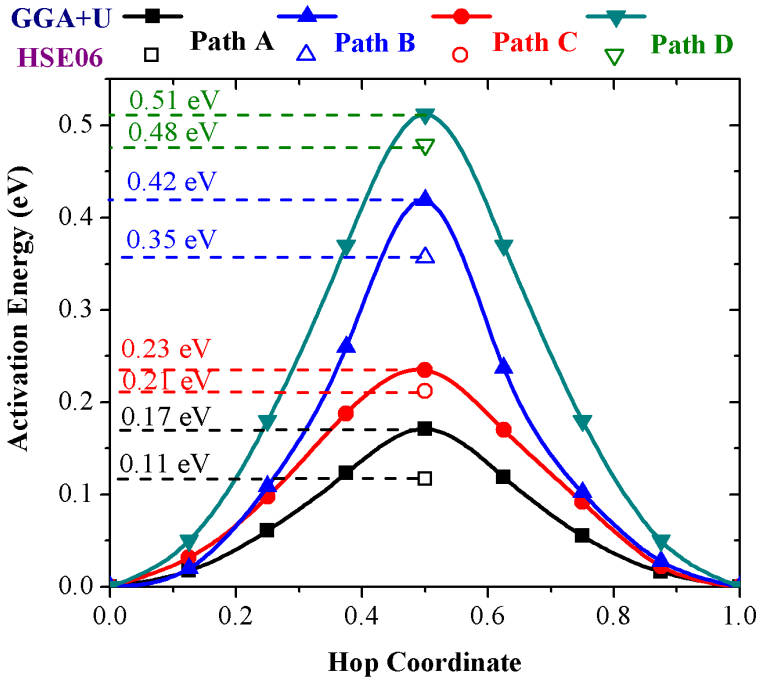

Figure 4.8: Polaron migration energies calculated with DFT+U (filled) and HSE06 (unfilled) methods along the different migration paths in α-MoO_3 illustrated in Figure 4.7.

The highest anisotropy is found between the low-energy jumps along the a and c crystallographic directions within the bilayer sheets, and hopping along path D, across the van der Waals gaps. With the calculated polaron hopping barriers labeled in Figure 4.8, we can roughly estimate the anisotropy of polaron mobilities within and across the bilayer sheets using the expression for the hop frequency $\nu = \nu^* \exp(-\Delta E/k_B T)$, assuming that the attempt frequency ν^* varies relatively weakly amongst the different paths. With this assumption, the room temperature mobility parallel to the bilayer sheets is predicted to be approximately five orders of magnitude faster than that normal, due to the high activation energy for hopping across the van der Waals gaps. These estimates are in reasonable agreement with experimental measurements that report room-temperature electron conductivities of 10^{-10} and 10^{-4} S$\cdot$ cm^{-1} perpendicular to and within the MoO_3 bilayer sheets,

respectively [261, 36]. It is also worth noting that Berthumeyrie *et al.* [45] report a measured polaron hopping activation energy of 0.43 eV in "classical particle" samples. Considering that the measurements on these samples are likely to represent an average over crystallographic orientations, and that the nature of the averaging will depend on the texture of the grains in the sample, a direct comparison with the present results is difficult. However, the value of 0.43 eV does lie within the range of computed values for the polaron hopping barriers reported in Figure 4.8.

4.4 Diffusion of a Polaron Bound to Lithium

4.4.1 Computational Details and Results

Calculations including polarons and intercalated Li ions made use of the similar computational settings of the isolated polaron as described in Section 4.3.1. The PAW potentials for lithium employed in this work is that labeled "Li_sv" in the VASP PAW-PBE library. To investigate the interaction energies between intercalated Li ions and electron small polarons, we extended the DFT+U calculations, through the incorporation of single Li atoms directly in the $3 \times 1 \times 3$ supercells, giving an overall composition of $Li_{0.028}MoO_3$. Two intercalation sites were considered for the Li ions in these calculations, as illustrated in Figure 4.9. One site is located within the two-dimensional van der Waals gaps within the α-MoO_3 structure, and will be referred to in what follows as an interlayer position. The second is located within one-dimensional channels and will be referred to as the intralayer position. When Li atoms are positioned in either site, and a neighboring MoO_6 octahedron is distorted to facilitate polaron formation, the calculations converge to a state in which the valence electron from Li is transferred to the targeted Mo^{6+} site, leading to the formation of Li^+ and Mo^{5+} ions. Based on the bonding distortion configurations of isolated polaron, in studies of polaron-Li-ion binding, we were able to control the position of the polaron relative to the Li ion by selectively perturbing the Mo-O bond lengths in the desired MoO_6 octahedron as discussed in Table 4.5.

When the Mo^{5+} polaron is located as a nearest neighbor to the intercalated Li^+ ion, the DFT+U calculations predict that the intralayer site is slightly lower in energy, by approximately 0.05 eV. However, this result is influenced by the relative magnitudes of the binding energy between Li^+ and Mo^{5+} ions in the two sites. Specifically, by comparing the energy differences between states in which the polaron is nearest and furthest from a Li^+ ion in each site, we derive estimates of the binding energy E_b given in Table 4.6. It can be seen that the binding between the polaron and Li^+ ion is stronger for the intralayer site by approximately 0.08 eV. The larger binding energy in the intralayer site correlates with the shorter distance between Li^+ and Mo^{5+} ions in this site (2.79 Å) versus the interlayer site (4.69 Å). As a consequence of the different values for the binding energies, if the polaron is completely dissociated from the intercalated Li^+ ion, the site stability reverses, with the interlayer site being weakly favored. It is worth noting that despite the slightly higher Li-ion concentration used in our supercell calculations (0.028 Li to Mo fraction), the magnitude of the Li-polaron binding energies computed by DFT+U are in reasonable agreement with the estimate of 0.22 eV derived from dielectric spectroscopy measurements on $Li_{0.01}MoO_3$ samples by Berthumeyrie *et al.* [45].

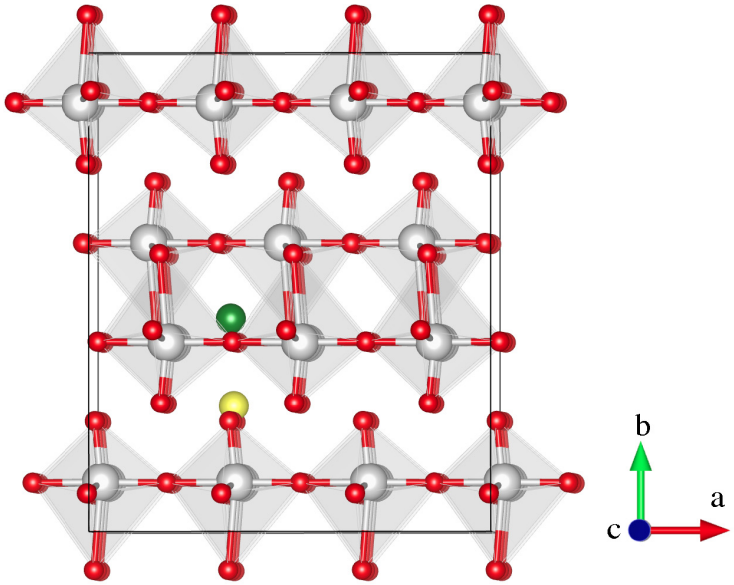

Figure 4.9: Lithium intercalation sites in a α-MoO_3 supercell. The yellow sphere denotes the interlayer site within the interlayer van der Waals gap, and the green sphere denotes the intralayer site within the one-dimensional channels formed between MoO_6 octahedron within the bilayer sheets.

Table 4.6: Calculated migration barriers (E_m) for electron small polarons bound to neighboring Li^+ ions, and binding energies (E_b) between polarons and Li^+ ions, as obtained by the DFT+U method in $3 \times 1 \times 3$ supercells with composition $Li_{0.028}MoO_3$. Calculated results are compared with experimental measurements reported for $Li_{0.01}MoO_3$. All energies are reported in units of eV.

Intercalation Site	E_m		E_b	
	Path A	Path C	Cal.	Exp. [45]
Interlayer	0.23	0.29	0.26	0.22
Intralayer	0.27	0.34	0.34	

Also listed in Table 4.6 are results obtained by DFT+U for the activation energies for hopping of a polaron away from the nearest neighbor of a Li^+ ion along the low-energy paths A and C. From a comparison of the results in Figure 4.6 with those plotted in Table 4.8, it can be seen that the migration energy of polarons bound to Li ions in the iterlayer site increases by approximately 0.06 eV. A slightly larger increase is found for polarons bound to Li ions in interlayer sites, where migration energies along both paths A and C are raised by approximately 0.1 eV.

4.4.2 Lattice Relaxation Effect

The computational results presented above were obtained from DFT+U calculations in which the lattice parameters of the supercell were fixed at experimentally measured values for pure the bulk α-MoO_3. However, previous experimental observations suggest that the lithium intercalation into α-MoO_3 give rise to lattice expansions [36, 201]. The current calculations also have shown that the magnitude of the lattice expansions for lithium intercalation in interlayer sites is relatively larger than that in interlayer sites as shown in Figure 4.9.

To investigate the effect of cell-volume and cell-shape relaxations we have performed calculations with the optB88 [59] and DFT(PBE)+D2 [62] functionals, which explicitly account for vdW contributions to the energy. In these calculations we also include Hubbard-U corrections with U_{eff} = 6 eV. For calculations with fixed lattice constants, the optB88+U and DFT+U+D2 results are in qualitative agreement with the DFT+U results for Li-polaron binding energies described above.

Specifically, both of the vdW-corrected functionals predict a stronger binding energy between Li and electron small polarons in the intralayer relative to the interlayer site (by 0.06 eV for optB88+U and 0.11 eV for DFT+U+D2). Further, both of these functionals predict that the difference in binding energy is sufficient to reverse the site preference for intercalated Li ions, with interlayer (intralayer) sites being energetically favorable when the polaron is far from (near to) Li in calculations with fixed lattice parameters. When the lattice parameters of the supercell are allowed to relax, the calculated magnitudes and differences in binding energy between polarons and Li ions in interlayer and intralayer sites are relatively similar to those listed in Table 4.6, with E_b values of 0.20 (interlayer) and 0.30 (intralyer) eV from optB88+U, and 0.17 (interlayer) and 0.30 (intralayer) eV from DFT+U+D2. However, the two different vdW-corrected functionals differ in their predictions of the site preferences for the intercalated Li ions when the supercell lattice parameters are relaxed: optB88+U predicts that the interlayer position is favored both when polarons are near and far from the intercalated Li (by 0.03 and 0.13 eV, respectively), while DFT+U+D2 (like DFT+U) predicts that the interlayer site is preferred (by 0.06 eV) when the polaron is far from Li and that the intralayer site is preferred (by 0.07 eV) when it is near. While the details of the calculations differ depending on the functional used, collectively the computational results suggest that site selection of Li^+ ions is likely to be governed by a balance of competing thermodynamic effects, including configurational entropy (enhanced by dissociation of Li^+ ions from polarons [262]), binding energies (favoring association of Li ions and polarons), and coherency and particle-size effects that impose boundary conditions on the elastic relaxations.

4.5 Summary

Different density functional theory-based methods have been applied to the calculation of the atomic structure of the bulk α-MoO_3 compound. We found the DFT-D2 and optB88 methods yield calculated lattice parameters and bond lengths that agree well with experimental measurements. The present results show an encouraging level of accuracy in the application of these van der Waals corrected density functional theory methods for

characterizing both bonded and non-bonded interatomic interactions in α-MoO_3.

A better description of the electronic structure for α-MoO_3 could be achieved through employing methods for correcting self-interaction errors in density functional theory, including DFT+U and hybrid-functional methods. These methods also have been used to study the properties of electron small polarons in α-MoO_3.The calculations establish that the small polaron forms in an electronic state that has predominantly Mo $4d_{xz}$ character. Polaron formation gives rise to a pronounced elongation in the bond length with the nearest-neighbor corner-shared oxygen ion within the *a*-*c* plane. The adiabatic barriers for polaron hopping in α-MoO_3 are calculated by DFT+U to be 0.17 eV and 0.23 eV for hopping within the same *a*-*c* plane within the bilayer sheets along the *a* and *c* crystallographic directions, respectively. Hopping between the nearest-neighbor Mo ions, along the zig-zag chains within the bilayers is calculated to involve a significantly larger hopping barrier of 0.42 eV. The largest barrier for polaron transport is calculated to be 0.51 eV, for hopping across the van der Waals gap, along the *b* direction. HSE06 calculations yield slightly smaller activation energies relative to DFT+U, but with very similar anisotropies.

The binding energy of polarons to intercalated Li ions is calculated by DFT+U to be approximately 0.3 eV in $Li_{0.028}MoO_3$ supercells, when Li resides within the one-dimension interlayer channel positions. The energy differences between Li in interlayer and intralayer positions is thus influenced by binding with polarons. This energy difference is also found to depend on the nature of the elastic relaxations, as well as the functionals used in the calculations. Overall the computed results suggest that the site preference for intercalated Li ions in α-MoO_3 is likely to be governed by a balance of thermodynamic factors including temperature and particle size.

Part III

Concluding Remarks

Chapter 5

Summary, Conclusions and Future Work

5.1 Summary and Conclusions

In this dissertation, we have explored the capability of first-principles modeling of the diffusion properties in complex materials. The basic theory and methodology was discussed in Chapter 2, and applied for modeling two different diffusion processes in emerging advanced materials: (i) atomic diffusion in ferritic alloys presented in Chapter 3, and (ii) electronic diffusion in α-MoO_3 for electrochemical applications presented in Chapter 4.

For ferritic alloys, first-principles methods are employed to investigate (1) Fe self diffusivity modeling and the associated effect of magnetic disorder, (2) transition metal solute diffusivity in bcc Fe, and (3) point defects in Ni-Al based intermetallic precipitates. We found that:

(1) Self-diffusion activation energies in both ferromagnetic and paramagnetic bcc Fe can be calculated with the spin-wave approach. Combined with the diffusion prefactor calculated within the framework of harmonic transition-state theory, the present first-principles computational framework yields results for the self-diffusion coefficient in good agreement with experimental measurements spanning over the Curie temperature. The comparison between Fe and Co for the vacancy formation energies in both ferromagnetic and paramagnetic states suggests that the magnitude of the effect of the magnetic phase transition on self diffusivity is correlated with d-band filling.

(2) The transition metal solute diffusion coefficients in bcc Fe are calculated in the present work, showing an overall good agreement with available experimental results. Our calculations demonstrate the competing effect between diffusion activation energies and prefactors, with both quantities exhibiting maximum values in the center of the transition metal series. Solute species Co, Re, Os, Ir and Y are suggested as potential candidates for slow diffusers in bcc Fe.

(3) The intrinsic point defects in the off-stoichiometry region of B2-NiAl and $L2_1$-Ni_2AlTM (TM= Ti, Zr or Hf) have been investigated. Results for B2-NiAl show a lower concentration of vacancies in the Ni-rich region compared to that in the Al-rich region. Comparisons among three $L2_1$ intermetallic alloys Ni_2AlTM (TM= Ti, Zr and Hf) show

that the magnitude of vacancy concentration in off-stoichiometry regions is associated with transition metal species, where Ni_2AlTi gives the lowest vacancy concentration. It would be more desirable to have B2-NiAl precipitates in the Ni-rich region and $L2_1$-Ni_2AlTi for the hierarchical structure in the creep-resistant alloy design.

For α-MoO_3, a material of interest as an electrode in batteries and pseudocapacitors, first-principles methods are employed to study (1) The atomic and electronic structure, (2) Isolated electron polaron formation and diffusion, and (3) Lithium-induced polaron binding and lattice expansion. We found that:

(1) Accurate predictions of the first-principles modeling for the atomic structure of α-MoO_3 require corrections for the van der Waals force. The calculated lattice parameters and bond lengths resulting from DFT-D2 and optB88 methods agree well with experimental measurements. Calculations also suggest that a Hubbard-U correction (DFT+U) or hybrid functionals (HSE06) yield a better description of the electronic structure for α-MoO_3.

(2) The formation of an isolated electron small polaron in α-MoO_3 is confirmed in the first-principles modeling by DFT+U and HSE06 methods. Calculations establish that the small polaron occupies the Mo $4d_{xz}$ orbital, coupled with elongation of the nearest-neighbor corner-shared O-Mo bond. The adiabatic barrier calculations for polaron hopping show that electronic hopping within the *a*-*c* plane has smaller activation energy barriers than the other nearest-neighbor directions, suggesting a high degree of anisotropy in the polaron mobilities in the crystal.

(3) The binding energy between an electron small polaron and intercalated Li ions is calculated using DFT+U, which affects the corresponding polaron hopping activation energies. Calculations show that Li ions that reside within the one-dimensional interlayer channel positions have lower energy compared to Li ions that reside in the two-dimensional interlayer sites within the van der Waals gaps, although the energy differences depend on the nature of lattice relaxations and functionals used in the calculations.

5.2 Directions for future work

Based on the work presented in this dissertation, several research areas which are of interest for continuing work are listed below:

(1) The present work has developed a computational framework to account for the effect of magnetic disorder on self-diffusivity of bcc Fe. The effect of magnetic disorder is also observed in solute impurity diffusion, thus, it would be of interest to extend the present framework to study the corresponding effects of magnetic disorder in ferritic alloys. However, one of the challenges is that the "spin-wave" method employed here is mostly designed to account for the transverse magnetic fluctuations, while the presence of solute atoms in the system may result in the longitudinal magnetic fluctuations. In this context, developing a methodology that considers both transverse and local longitudinal fluctuations would be interesting for future studies

(2) The work presented in Section 3.4 focuses on the solute impurity diffusion coefficient calculations in dilute limit. An extension of the current work to the non-dilute systems would be highly interesting. We noticed some pioneering work focusing on developing several time coarse-graining methods for studying the concentration dependent diffusion

coefficients [263, 264], which would be worthwhile to be employed for future diffusivity calculations for multicomponent alloys.

(3) The work in Chapter 4 presents the electronic diffusion properties through "small polaron hopping" mechanisms in α-MoO_3. Since the intercalated lithium ion would also donate the extra electron, forming the lithium-polaron binding, it would be reasonable to speculate that the Li ion diffusion may couple with the polaron motion. A computational investigation of the lithium ion and polaron coupled diffusion would give special insight into the ionic and electronic conduction for electrode material applications.

Bibliography

[1] S. Huang, *et al.*, *Acta Materialia* **58**, 1982 (2010).

[2] C.-K. Loong, J. Carpenter, J. Lynn, R. Robinson, H. Mook, *Journal of Applied Physics* **55**, 1895 (1984).

[3] J. Lynn, *Physical Review B* **11**, 2624 (1975).

[4] F. Buffington, K. Hirano, M. Cohen, *Acta Metallurgica* **9**, 434 (1961).

[5] G. Hettich, H. Mehrer, K. Maier, *Scripta Metallurgica* **11**, 795 (1977).

[6] Y. Iijima, K. Kimura, K. Hirano, *Acta Metallurgica* **36**, 2811 (1988).

[7] M. Lübbehusen, H. Mehrer, *Acta Metallurgica et Materialia* **38**, 283 (1990).

[8] D. James, G. Leak, *Philosophical Magazine* **14**, 701 (1966).

[9] D. Graham, D. Tomlin, *Philosophical Magazine* **8**, 1581 (1963).

[10] J. Geise, C. Herzig, *Zeitschrift Fur Metallkunde* **78**, 291 (1987).

[11] R. Borg, C. Birchenall, *Transactions of the American Institute of Mining, Metallurgical, and Petroleum Engineers* **218**, 980 (1960).

[12] C. M. Walter, N. L. Peterson, *Physical Review* **178**, 922 (1969).

[13] J. Kuera, B. Million, J. Rikov, V. Foldyna, A. Jakobov, *Acta Metallurgica* **22**, 135 (1974).

[14] K. Hirano, R. Agarwala, B. Averbach, M. Cohen, *Journal of Applied Physics* **33**, 3049 (1962).

[15] W. Bussmann, C. Herzig, W. Rempp, K. Maier, H. Mehrer, *Physica Status Solidi (a)* **56**, 87 (1979).

[16] F. C. Nix, F. E. Jaumot, *Physical Review* **82**, 72 (1951).

[17] C. Kittel, *Introduction to Solid State Physics* (John Wiley & Sons, Inc., New York, 1986), 6th edn.

[18] A. D. Le Claire, *Philosophical Magazine* **21**, 819 (1970).

[19] Y. Iijima, *Journal of Phase Equilibria and Diffusion* **26**, 466 (2005).

[20] A. Fick, *Annalen der Physik* **170**, 59 (1855).

[21] A. Fick, *The London, Edinburgh, and Dublin Philosophical Magazine and Journal of Science* **10**, 30 (1855).

[22] R. Brown, *The Philosophical Magazine, or Annals of Chemistry, Mathematics, Astronomy, Natural History and General Science* **4**, 161 (1828).

[23] A. Einstein, *Annalen der Physik* **322**, 549 (1905).

[24] M. von Laue, *Nobel lecture* (1915).

[25] J. Frenkel, *Zeitschrift für Physik* **35**, 652 (1926).

[26] C. Wagner, W. Schottky, *Zeitschrift fr Physikalische Chemie B* **11**, 163 (1930).

[27] A. Smigelskas, E. Kirkendall, *Transactions of the American Institute of Mining, Metallurgical, and Petroleum Engineers* **171**, 130 (1947).

[28] Z. Teng, *et al.*, *Scripta Materialia* **63**, 61 (2010).

[29] S. Huang, *et al.*, *Metallurgical and Materials Transactions A* **43**, 1497 (2012).

[30] N. Q. Vo, C. H. Liebscher, M. J. Rawlings, M. Asta, D. C. Dunand, *Acta Materialia* **71**, 89 (2014).

[31] H. L. Lukas, S. G. Fries, B. Sundman, *Computational Thermodynamics: the Calphad Method*, vol. 131 (Cambridge University Press Cambridge, 2007).

[32] J. Andersson, T. Helander, L. Höglund, P. Shi, B. Sundman, *Calphad* **26**, 273 (2002).

[33] P. E. Turchi, *et al.*, *Calphad* **31**, 4 (2007).

[34] Thermo-Calc Software AB, Stockholm, SWE, *MOB2, Mobility Database*.

[35] S. Huang, *et al.*, *Acta Materialia* **58**, 1982 (2010).

[36] L. Mai, *et al.*, *Advanced Materials* **19**, 3712 (2007).

[37] T. Brezesinski, J. Wang, S. Tolbert, B. Dunn, *Nature Materials* **9**, 146 (2010).

[38] W. Tang, *et al.*, *Chemical Communications* **47**, 10058 (2011).

[39] R. Liang, H. Cao, D. Qian, *Chemical Communications* **47**, 10305 (2011).

[40] Z. Wang, S. Madhavi, X. W. Lou, *The Journal of Physical Chemistry C* **116**, 12508 (2012).

[41] B. Kang, G. Ceder, *Nature* **458**, 190 (2009).

[42] M. Park, X. Zhang, M. Chung, G. B. Less, A. M. Sastry, *Journal of Power Sources* **195**, 7904 (2010).

[43] V. Etacheri, R. Marom, R. Elazari, G. Salitra, D. Aurbach, *Energy & Environmental Science* **4**, 3243 (2011).

[44] C. Julien, A. Khelfa, O. Hussain, G. Nazri, *Journal of Crystal Growth* **156**, 235 (1995).

[45] S. Berthumeyrie, *et al.*, *The Journal of Physical Chemistry C* **114**, 19803 (2010).

[46] E. Schrödinger, *Physical Review* **28**, 1049 (1926).

[47] M. Born, R. Oppenheimer, *Annalen der Physik* **389**, 457 (1927).

[48] P. Hohenberg, W. Kohn, *Physical Review* **136**, B864 (1964).

[49] R. G. Parr, W. Yang, *Density-Functional Theory of Atoms and Molecules*, vol. 16 (Oxford university press, 1989).

[50] W. Kohn, L. J. Sham, *Physical Review* **140**, A1133 (1965).

[51] S. Vosko, L. Wilk, M. Nusair, *Canadian Journal of Physics* **58**, 1200 (1980).

[52] M. Pant, A. Rajagopal, *Solid State Communications* **10**, 1157 (1972).

[53] P. A. Dirac, *Mathematical Proceedings of the Cambridge Philosophical Society* (Cambridge Univ Press, 1930), vol. 26, pp. 376–385.

[54] D. M. Ceperley, B. Alder, *Physical Review Letters* **45**, 566 (1980).

[55] J. P. Perdew, A. Zunger, *Physical Review B* **23**, 5048 (1981).

[56] A. D. Becke, *Physical Review A* **38**, 3098 (1988).

[57] J. P. Perdew, *et al.*, *Physical Review B* **46**, 6671 (1992).

[58] J. P. Perdew, K. Burke, M. Ernzerhof, *Physical Review Letters* **77**, 3865 (1996).

[59] J. Klimeš, D. R. Bowler, A. Michaelides, *Journal of Physics: Condensed Matter* **22**, 022201 (2010).

[60] J. Klimeš, D. R. Bowler, A. Michaelides, *Physical Review B* **83**, 195131 (2011).

[61] S. Grimme, *Journal of Computational Chemistry* **25**, 1463 (2004).

[62] S. Grimme, *Journal of Computational Chemistry* **27**, 1787 (2006).

[63] S. Grimme, J. Antony, S. Ehrlich, H. Krieg, *The Journal of Chemical Physics* **132**, 154104 (2010).

[64] S. Grimme, *Wiley Interdisciplinary Reviews: Computational Molecular Science* **1**, 211 (2011).

[65] M. Dion, H. Rydberg, E. Schröder, D. Langreth, B. Lundqvist, *Physical Review Letters* **92**, 246401 (2004).

[66] G. Pérez, J. Soler, *Physical Review Letters* **103**, 096102 (2009).

[67] Y. Zhang, W. Yang, *Physical Review Letters* **80**, 890 (1998).

[68] O. A. Vydrov, T. Van Voorhis, *Physical Review Letters* **103**, 063004 (2009).

[69] O. A. Vydrov, T. Van Voorhis, *The Journal of Chemical Physics* **133**, 244103 (2010).

[70] K. Lee, É. Murray, L. Kong, B. Lundqvist, D. Langreth, *Physical Review B* **82**, 081101 (2010).

[71] K. Berland, P. Hyldgaard, *Physical Review B* **89**, 035412 (2014).

[72] O. A. Vydrov, G. E. Scuseria, *The Journal of Chemical Physics* **121**, 8187 (2004).

[73] C. Froese Fischer, *Computer Physics Communications* **43**, 355 (1987).

[74] L. Hedin, *Physical Review* **139**, A796 (1965).

[75] L. Hedin, S. Lundqvist, *Solid State Physics* **23**, 1 (1970).

[76] B. Himmetoglu, A. Floris, S. Gironcoli, M. Cococcioni, *International Journal of Quantum Chemistry* **114**, 14 (2014).

[77] A. D. Becke, *The Journal of Chemical Physics* **98**, 1372 (1993).

[78] K. Kim, K. Jordan, *The Journal of Physical Chemistry* **98**, 10089 (1994).

[79] J. P. Perdew, M. Ernzerhof, K. Burke, *The Journal of Chemical Physics* **105**, 9982 (1996).

[80] C. Adamo, V. Barone, *The Journal of Chemical Physics* **110**, 6158 (1999).

[81] J. Heyd, G. E. Scuseria, M. Ernzerhof, *The Journal of Chemical Physics* **118**, 8207 (2003).

[82] R. M. Martin, *Electronic Structure: Basic Theory and Practical Methods* (Cambridge university press, 2004).

[83] P. E. Blchl, *Physical Review B* **50**, 17953 (1994).

[84] G. Kresse, D. Joubert, *Physical Review B* **59**, 1758 (1999).

[85] H. Hellmann, *Deuticke, Leipzig and Wien, 350s* (1937).

[86] R. P. Feynman, *Physical Review* **56**, 340 (1939).

[87] A. A. Maradudin, E. W. Montroll, G. H. Weiss, I. Ipatova, *Theory of Lattice Dynamics in the Harmonic Approximation*, vol. 12 (Academic press New York, 1963).

[88] G. Leibfried, W. Ludwig, *Solid State Physics* **12**, 275 (1961).

[89] S. Baroni, P. Giannozzi, A. Testa, *Physical Review Letters* **58**, 1861 (1987).

[90] D. G. Truhlar, B. C. Garrett, S. J. Klippenstein, *The Journal of Physical Chemistry* **100**, 12771 (1996).

[91] G. H. Vineyard, *Journal of Physics and Chemistry of Solids* **3**, 121 (1957).

[92] T. Pollock, A. Argon, *Acta Metallurgica et Materialia* **40**, 1 (1992).

[93] A. Borgenstam, L. Höglund, J. Ågren, A. Engström, *Journal of phase equilibria* **21**, 269 (2000).

[94] CompuTherm, LLC, Stockholm, SWE, *TC-PRISMA: Thermodynamic and Diffusion Calculations*.

[95] CompuTherm, LLC, Madisonm, USA, *PanFe-Thermodynamic Database for Multi-component Iron Alloys*.

[96] C. Domain, C. S. Becquart, *Physical Review B* **65**, 024103 (2001).

[97] C. Domain, C. Becquart, *Physical Review B* **71**, 1 (2005).

[98] K. L. Wong, H.-J. Lee, J.-H. Shim, B. Sadigh, B. D. Wirth, *Journal of Nuclear Materials* **386**, 227 (2009).

[99] X.-S. Kong, *et al.*, *Acta Materialia* **66**, 172 (2014).

[100] C. Zhang, *et al.*, *Journal of Nuclear Materials* **455**, 354 (2014).

[101] H. Ding, V. I. Razumovskiy, M. Asta, *Acta Materialia* **70**, 130 (2014).

[102] H. Ding, S. Huang, G. Ghosh, P. K. Liaw, M. Asta, *Scripta Materialia* **67**, 732 (2012).

[103] J. Philibert, *Atom Movements Diffusion and Mass Transport in Solids (Les Editions de Physique, Les Ulis, France, 1991)* (Editions de Physique, 1991).

[104] H. Bakker, H. Mehrer, *Diffusion in Solid Metals and Alloys* (Springer-Verlag, 1990).

[105] B. Fultz, *Progress in Materials Science* **55**, 247 (2010).

[106] R. J. Borg, *Journal of Applied Physics* **35**, 567 (1964).

[107] D. J. Dever, *Journal of Applied Physics* **43**, 3293 (1972).

[108] L. Girifalco, *Journal of Physics and Chemistry of Solids* **23**, 1171 (1962).

[109] L. Ruch, D. R. Sain, H. L. Yeh, L. Girifalco, *Journal of Physics and Chemistry of Solids* **37**, 649 (1976).

[110] J. Crangle, G. Goodman, *Proceedings of the Royal Society of London. A. Mathematical and Physical Sciences* **321**, 477 (1971).

[111] H. Potter, *Proceedings of the Royal Society of London. Series A* **146**, 362 (1934).

[112] H. Mehrer, *Journal of Nuclear Materials* **69**, 38 (1978).

[113] G. Neumann, C. Tuijn, *Pergamon Materials Series* **14**, 259 (2008).

[114] H. Nitta, Y. Iijima, *Philosophical magazine letters* **85**, 543 (2005).

[115] H. Wen, P.-W. Ma, C. Woo, *Journal of Nuclear Materials* (2013).

[116] A. Glensk, B. Grabowski, T. Hickel, J. Neugebauer, *Physical Review X* **4**, 011018 (2014).

[117] T. Garnier, M. Nastar, P. Bellon, D. R. Trinkle, *Physical Review B* **88**, 134201 (2013).

[118] J. Bocquet, *Philosophical Magazine* **94**, 3603 (2014).

[119] A. I. Lichtenstein, M. I. Katsnelson, G. Kotliar, *Physical Review Letters* **87**, 067205 (2001).

[120] M. Cyrot, *Physical Review Letters* **25**, 871 (1970).

[121] J. Hubbard, *Physical Review B* **19**, 2626 (1979).

[122] J. Hubbard, *Physical Review B* **20**, 4584 (1979).

[123] H. Hasegawa, *Journal of the Physical Society of Japan* **49**, 963 (1980).

[124] B. L. Gyorffy, A. J. Pindor, J. Staunton, G. M. Stocks, H. Winter, *Journal of Physics F: Metal Physics* **15**, 1337 (1985).

[125] P. Soven, *Physical Review* **156**, 809 (1967).

[126] B. Gyorffy, *Physical Review B* **5**, 2382 (1972).

[127] P. Söderlind, A. Landa, B. Sadigh, *Physical Review B* **66**, 205109 (2002).

[128] P. Söderlind, A. Landa, B. Sadigh, L. Vitos, A. Ruban, *Physical Review B* **70**, 144103 (2004).

[129] B. Alling, T. Marten, I. A. Abrikosov, *Physical Review B* **82**, 184430 (2010).

[130] F. Körmann, A. Dick, B. Grabowski, T. Hickel, J. Neugebauer, *Physical Review B* **85**, 125104 (2012).

[131] P. Steneteg, B. Alling, I. A. Abrikosov, *Physical Review B* **85**, 144404 (2012).

[132] A. Zunger, S.-H. Wei, L. G. Ferreira, J. E. Bernard, *Physical Review Letters* **65**, 353 (1990).

[133] A. V. Ruban, V. I. Razumovskiy, *Physical Review B* **85**, 174407 (2012).

[134] H. H. Potter, *Proceedings of the Royal Society A* **146**, 362 (1934).

[135] A. Baldereschi, *Physical Review B* **7**, 5212 (1973).

[136] D. J. Chadi, M. L. Cohen, *Physical Review B* **8**, 5747 (1973).

[137] H. J. Monkhorst, J. D. Pack, *Physical Review B* **13**, 5188 (1976).

[138] J. P. Perdew, K. Burke, M. Ernzerhof, *Physical Review Letters* **77**, 3865 (1996).

[139] I. Seki, K. Nagata, *Journal of the Iron and Steel Institute of Japan* **45**, 1789 (2005).

[140] G. H., Vineyard, *Journal of Physics and Chemistry of Solids* **3**, 121 (1957).

[141] J. Neuhaus, W. Petry, A. Krimmel, *Physica B: Condensed Matter* **234**, 897 (1997).

[142] P. Olsson, C. Domain, J. Wallenius, *Physical Review B* **75**, 014110 (2007).

[143] The converged initial phase cutoff (parameter ENINI in VASP) has been found to be around 350 eV in this work, while the value of 250 eV was used before. According to our tests, this cutoff difference is the primary source of the discrepancies between the results reported here and in Ref. [133].

[144] L. De Schepper, *et al.*, *Physics Letters A* **95**, 121 (1983).

[145] H.-E. Schaefer, *et al.*, *Scripta Metallurgica* **11**, 803 (1977).

[146] M. Mantina, *et al.*, *Physical Review Letters* **100**, 215901 (2008).

[147] M. R. LaBrosse, L. Chen, J. K. Johnson, *Modelling and Simulation in Materials Science and Engineering* **18**, 015008 (2010).

[148] P. G. Shewmon, *Diffusion in Solids* (The Minerals Metals and Materials Society, 1989), second edn.

[149] R. Bozorth, *Ferromagnetism* (Van Nostrand, New York, 1951).

[150] A. Janotti, M. Krčmar, C. L. Fu, R. C. Reed, *Physical Review Letters* **92**, 085901 (2004).

[151] D. Simonovic, M. H. F. Sluiter, *Physical Review B* **79**, 054304 (2009).

[152] M. Mantina, Y. Wang, L. Chen, Z. Liu, C. Wolverton, *Acta Materialia* **57**, 4102 (2009).

[153] G. Kresse, J. Hafner, *Physical Review B* **47**, 558 (1993).

[154] G. Kresse, J. Hafner, *Physical Review B* **49**, 14251 (1994).

[155] G. Kresse, J. Furthmller, *Computational Materials Science* **6**, 15 (1996).

[156] G. Kresse, J. Furthmuller, *Physical Review B* **54**, 11169 (1996).

[157] H. J. Monkhorst, J. D. Pack, *Physical Review B* **13**, 5188 (1976).

[158] T. Ohnuma, N. Soneda, M. Iwasawa, *Acta Materialia* **57**, 5947 (2009).

[159] S. Choudhury, *et al.*, *Journal of Nuclear Materials* **411**, 1 (2011).

[160] C. Domain, C. Becquart, L. Malerba, *Journal of Nuclear Materials* **335**, 121 (2004).

[161] O. I. Gorbatov, P. A. Korzhavyi, A. V. Ruban, B. Johansson, Y. N. Gornostyrev, *J. Nucl. Mater.* **419**, 248 (2011).

[162] M. Mantina, S. Shang, Y. Wang, L. Chen, Z. Liu, *Physical Review B* **80**, 184111 (2009).

[163] C. Zacherl, A computational investigation of the effect of alloying elements on the thermodynamic and diffusion properties of fcc ni alloys, with application to the creep rate of dilute ni-x alloys, Ph.D. thesis, The Pennsylvania State University (2012).

[164] D. Murali, B. Panigrahi, M. Valsakumar, C. Sundar, *J. Nucl. Mater.* **419**, 208 (2011).

[165] M. Mantina, *et al.*, *Journal of Physics: Condensed Matter* **24**, 305402 (2012).

[166] H. Jonsson, G. Mills, K. W. Jacobsen (1998).

[167] G. Henkelman, H. Jonsson, *The Journal of Chemical Physics* **113**, 9978 (2000).

[168] N. Oono, H. Nitta, Y. Iijima, *Materials Transactions* **44**, 2078 (2003).

[169] Y. Zhang, G. Kresse, C. Wolverton, *Physical Review Letters* **112**, 075502 (2014).

[170] J. Crangle, G. M. Goodman, *Proceedings of the Royal Society of London A* **321**, 477 (1971).

[171] P. Klugkist, C. Herzig, *Physica Status Solidi (a)* **148**, 413 (1995).

[172] D. Murali, B. Panigrahi, M. Valsakumar, C. Sundar, *Journal of Nuclear Materials* **419**, 208 (2011).

[173] A. Bowen, G. Leak, *Metallurgical Transactions* **1**, 1695 (1970).

[174] R. Braun, M. Feller-Kniepmeier, *Physica Status Solidi (a)* **90**, 553 (1985).

[175] C. Lee, Y. Iijima, T. Hiratani, K. Hirano, *Materials Transactions* **31**, 255 (1990).

[176] R. Borg, D. Lai, *Acta Metallurgica* **11**, 861 (1963).

[177] K. Hirano, M. Cohen, *Transactions of the Japan Institute of Metals* **13**, 96 (1972).

[178] Y. Iijima, K. Kimura, C. Lee, K. Hirano, *Materials Transactions* **34**, 20 (1993).

[179] K. Hirano, M. Cohen, B. Averbach, *Acta Metallurgica* **9**, 440 (1961).

[180] R. Borg, D. Lai, *Acta Metallurgica* **11**, 861 (1963).

[181] J. Cermak, M. Lubbehusen, H. Mehrer, *Zeitschrift fr Metallkunde* **80**, 213 (1989).

[182] M. S. Anand, R. P. Agarwala, *Journal of Applied Physics* **37**, 4248 (1966).

[183] S. J. Rothman, N. L. Peterson, C. M. Walter, L. J. Nowicki, *Journal of Applied Physics* **39**, 5041 (1968).

[184] G. R. Speich, J. A. Gula, R. M. Fisher, *The Electron Microprobe* (Wiley, New York, 1966).

[185] G. Salje, M. FellerKniepmeier, *Journal of Applied Physics* **48**, 1833 (1977).

[186] I. Richter, M. Feller-Kniepmeier, *Physica Status Solidi (a)* **68**, 289 (1981).

[187] G. Neumann, C. Tuijn, *Self-Diffusion and Impurity Diffusion in Pure Metals: Handbook of Experimental Data*, G. Neumann, C. Tuijn, eds. (Pergamon, 2008), vol. 14 of *Pergamon Materials Series*, pp. 259 – 316.

[188] J. Geise, C. Herzig, *Zeitschrift fr Metallkunde* **76**, 622 (1985).

[189] C. Herzig, J. Geise, S. Divinski, *Zeitschrift für Metallkunde* **93**, 1180 (2002).

[190] N. Oono, H. Nitta, Y. Iijima, *Materials Transactions* **44**, 2078 (2003).

[191] A. Bondy, V. Levy, C. Acad, *Science Series C* **272**, 19 (1971).

[192] T. Eguchi, Y. Iijima, K. Hirano, *Cryst Lattice Defects* **4**, 265 (1973).

[193] R. Klueh, J. Shingledecker, R. Swindeman, D. Hoelzer, *Journal of Nuclear Materials* **341**, 103 (2005).

[194] J. Antill, K. Peakall, Influence of an alloy addition of yttrium on the oxidation behaviour of an austenitic and a ferritic stainless steel in carbon dioxide, *Tech. rep.*, Atomic Energy Research Establishment, Harwell, Eng. (1967).

[195] A. Bradley, A. Taylor, *Proceedings of the Royal Society of London. Series A-Mathematical and Physical Sciences* **159**, 56 (1937).

[196] P. A. Korzhavyi, *et al.*, *Physical Review B* **61**, 6003 (2000).

[197] Y. Mishin, *Acta Materialia* **52**, 1451 (2004).

[198] C. Liebscher, V. Radmilovic, U. Dahmen, M. Asta, G. Ghosh, *Journal of Materials Science* **48**, 2067 (2013).

[199] Z. Sun, *et al.*, *Scripta Materialia* **68**, 384 (2013).

[200] Y. Iriyama, T. Abe, M. Inaba, Z. Ogumi, *Solid State Ionics* **135**, 95 (2000).

[201] S.-H. Lee, *et al.*, *Advanced Materials* **20**, 3627 (2008).

[202] T. Brezesinski, J. Wang, S. H. Tolbert, B. Dunn, *Nature Materials* **9**, 146 (2010).

[203] J. S. Chen, Y. L. Cheah, S. Madhavi, X. W. Lou, *The Journal of Physical Chemistry C* **114**, 8675 (2010).

[204] Y. Andersson, *et al.*, *Electronic Density Functional Theory* (Springer, 1998), pp. 243–260.

[205] W. Kohn, Y. Meir, D. E. Makarov, *Physical review letters* **80**, 4153 (1998).

[206] A. Pandit, M. Prasad, T. Ansari, R. Singh, B. Wanklyn, *Solid State Commun.* **80**, 125 (1991).

[207] H. Ding, K. G. Ray, V. Ozolins, M. Asta, *Physical Review B* **85**, 012104 (2012).

[208] H. Ding, *et al.*, *The Journal of Physical Chemistry C* **118**, 15565 (2014).

[209] H. C. Zeng, *Journal of Crystal Growth* **186**, 393 (1998).

[210] M. Chen, U. V. Waghmare, C. M. Friend, E. Kaxiras, *The Journal of Chemical Physics* **109**, 6854 (1998).

[211] X. Sha, L. Chen, A. C. Cooper, G. P. Pez, H. Cheng, *The Journal of Physical Chemistry C* **113**, 11399 (2009).

[212] R. Coquet, D. J. Willock, *Physical Chemistry Chemical Physics* **7**, 3819 (2005).

[213] F. Corà, A. Patel, N. M. Harrison, C. Roetti, C. R. A. Catlow, *Journal of Materials Chemistry* **7**, 959 (1997).

[214] D. O. Scanlon, *et al.*, *The Journal of Physical Chemistry C* **114**, 4636 (2010).

[215] A. B. Anderson, Y. Kim, D. W. Ewing, R. K. Grasselli, M. Tenhover, *Surface Science* **134**, 237 (1983).

[216] A. Sayede, T. Amriou, M. Pernisek, B. Khelifa, C. Mathieu, *Chemical Physics* **316**, 72 (2005).

[217] R. Coquet, D. Willock, *Physical Chemistry Chemical Physics* **7**, 3819 (2005).

[218] J. W. Bullard, R. L. Smith, *Solid State Ionics* **160**, 335 (2003).

[219] A. Tkatchenko, *et al.*, *MRS bulletin* **35**, 435 (2010).

[220] C. Adamo, V. Barone, *The Journal of Chemical Physics* **110**, 6158 (1999).

[221] J. Klimeš, D. Bowler, A. Michaelides, *Journal of Physics: Condensed Matter* **22**, 022201 (2010).

[222] A. Becke, *Physical Review A* **38**, 3098 (1988).

[223] P. E. Blöchl, *Physical Review B* **50**, 17953 (1994).

[224] G. Kresse, D. Joubert, *Physical Review B* **59**, 1758 (1999).

[225] M. Methfessel, A. T. Paxton, *Physical Review B* **40**, 3616 (1989).

[226] S. Grimme, *Journal of Computational Chemistry* **27**, 1787 (2006).

[227] J. c. v. Klimeš, D. R. Bowler, A. Michaelides, *Physical Review B* **83**, 195131 (2011).

[228] H. Peelaers, C. G. Van de Walle, *Journal of Physics: Condensed Matter* **26**, 305502 (2014).

[229] S. L. Dudarev, G. A. Botton, S. Y. Savrasov, C. J. Humphreys, A. P. Sutton, *Physical Review B* **57**, 1505 (1998).

[230] J. P. Perdew, K. Burke, M. Ernzerhof, *Physical Review Letters* **78**, 1396 (1997).

[231] S. Lutfalla, V. Shapovalov, A. T. Bell, *Journal of Chemical Theory and Computation* **7**, 2218 (2011).

[232] J. Heyd, G. E. Scuseria, *The Journal of Chemical Physics* **121**, 1187 (2004).

[233] J. Heyd, G. E. Scuseria, M. Ernzerhof, *The Journal of Chemical Physics* **124**, 219906 (2006).

[234] A. V. Krukau, O. A. Vydrov, A. F. Izmaylov, G. E. Scuseria, *The Journal of Chemical Physics* **125**, 224106 (2006).

[235] H. Sitepu, *Powder Diffraction* **24**, 315 (2009).

[236] H. Negishi, S. Negishi, Y. Kuroiwa, N. Sato, S. Aoyagi, *Physical Review B* **69**, 064111 (2004).

[237] F. Corà, A. Patel, N. M. Harrison, C. Roetti, C. R. A. Catlow, *Journal of Materials Chemistry* **7**, 959 (1997).

[238] A. Sayede, T. Amriou, M. Pernisek, B. Khelifa, C. Mathieu, *Chem. Phys.* **316**, 72 (2005).

[239] D. O. Scanlon, *et al.*, *The Journal of Physical Chemistry C* **114**, 4636 (2010).

[240] S. Deb, *Proceedings of the Royal Society of London. Series A. Mathematical and Physical Sciences* **304**, 211 (1968).

[241] A. Pandit, M. Prasad, T. Ansari, R. Singh, B. Wanklyn, *Solid State Communications* **80**, 125 (1991).

[242] M. Kröger, *et al.*, *Applied Physics Letters* **95**, 123301 (2009).

[243] R. Juryska, *Physica Status Solidi (b)* **72**, K161 (1975).

[244] M. Itoh, K. Hayakawa, S. Oishi, *Journal of Physics: Condensed Matter* **13**, 6853 (2001).

[245] V. Sabhapathi, *et al.*, *Physica Status Solidi (a)* **148**, 167 (1995).

[246] J. Zhou, S. Deng, N. Xu, J. Chen, J. She, *Applied Physics Letters* **83**, 2653 (2003).

[247] G. Li, L. Jiang, S. Pang, H. Peng, Z. Zhang, *The Journal of Physical Chemistry B* **110**, 24472 (2006).

[248] B. Yan, *et al.*, *The Journal of Physical Chemistry C* **113**, 20259 (2009).

[249] C. Rozzi, F. Manghi, F. Parmigiani, *Physical Review B* **68**, 075106 (2003).

[250] C.-T. Lin, *et al.*, *Journal of Applied Physics* **107**, 053703 (2010).

[251] X. K. Hu, *et al.*, *Chemistry of Materials* **20**, 1527 (2008).

[252] Z. Hu, *et al.*, *The Journal of Physical Chemistry C* **116**, 3962 (2012).

[253] M. F. Hassan, Z. Guo, Z. Chen, H. K. Liu, *J. Power Sources* **195**, 2372 (2010).

[254] X.-Y. Xue, Z.-H. Chen, L.-L. Xing, S. Yuan, Y.-J. Chen, *Chemical Communications* **47**, 5205 (2011).

[255] I. Navas, *et al.*, *Journal of Physics D: Applied Physics* **42**, 175305 (2009).

[256] V. I. Anisimov, J. Zaanen, O. K. Andersen, *Physical Review B* **44**, 943 (1991).

[257] F. Zhou, V. Ozoliņš, *Physical Review B* **80**, 125127 (2009).

[258] T. Maxisch, F. Zhou, G. Ceder, *Physical Review B* **73**, 104301 (2006).

[259] S. P. Ong, V. L. Chevrier, G. Ceder, *Physical Review B* **83**, 075112 (2011).

[260] M. Labanowska, *ChemPhysChem* **2**, 712 (2001).

[261] C. Julien, G. Nazri, *Solid State Ionics* **68**, 111 (1994).

[262] F. Zhou, T. Maxisch, G. Ceder, *Physical Review Letters* **97**, 155704 (2006).

[263] A. V. der Ven, H.-C. Yu, G. Ceder, K. Thornton, *Progress in Materials Science* **55**, 61 (2010).

[264] Q. Xu, A. Van der Ven, *Acta Materialia* **59**, 1095 (2011).

[265] N. Stoloff, C. Liu, S. Deevi, *Intermetallics* **8**, 1313 (2000).

[266] G. Frommeyer, R. Fischer, J. Deges, R. Rablbauer, A. Schneider, *Ultramicroscopy* **101**, 139 (2004).

[267] A. Lasalmonie, *Intermetallics* **14**, 1123 (2006).

[268] C. Woodward, M. Asta, G. Kresse, J. Hafner, *Physical Review B* **63**, 094103 (2001).

[269] S. P. Ong, *et al.*, *Computational Materials Science* **68**, 314 (2013).

[270] Sympy development team, http://sympy.org/.

[271] Numpy developers, http://numpy.org/.

[272] A. Jain, *et al.*, *APL Materials* **1**, 011002 (2013).

[273] G. Kresse, J. Hafner, *Physical Review B* **47**, 558 (1993).

[274] G. Kresse, J. Hafner, *Physical Review B* **49**, 14251 (1994).

[275] A. Jain, *et al.*, *Computational Materials Science* **50**, 2295 (2011).

[276] Y. Mishin, D. Farkas, *Philosophical Magazine A* **75**, 169 (1997).

[277] C. Jiang, *Acta Materialia* **55**, 4799 (2007).

Appendix A

Appendix

A.1 Introduction

Intermetallic compounds are a class of ordered alloy phases, consisting of two or more metallic elements, where each metal species occupies specific crystal lattice sites. The mechanical properties and phase stability of these materials have been actively investigated in a variety of contexts, including the design of materials for high-temperature structural applications. In this context, equilibrium point-defect concentrations, and site preferences for solute additions are important considerations for modeling phase stability and mechanical properties such as creep strength [265, 266, 267].

In intermetalic compounds that have relatively close-packed crystal structures, the dominant intrinsic point defects are expected to be substitutional antisites and vacancies. The concentration of these intrinsic defects is generally a strong function of the temperature and overall alloy composition. Additionally, solute impurities with sizes similar to those of the constituent atomic species are expected to form as substitutional defects, but which sublattice is preferred and whether such substitution triggers formation of additional intrinsic defects are important issues related to phase stability and mechanical behavior. Due to the importance of point-defect properties for the stability and mechanical behavior of intermetallic compounds, the inherent difficulty in their direct experimental measurement presents a significant challenge in the context of alloy design. This section describes the development of a computational tool that is intended to automate the process of performing first-principles predictions of point defect concentrations as a function of temperature and composition.

The present work is based on dilute-solution formalisms that have been well described in the literature for predicting intrinsic point defect equilibria and solute site preference. The purpose of developing an automated computational tool, here referred to as PyDII, is to build a user-friendly toolkit for predicting these properties based on density functional theory (DFT) calculations. The statistical model used in PyDII to compute defect concentrations is based on the method developed in Ref. [268], through minimization of a grand potential for intermetallic systems. The scripts used to generate the inputs and parse the outputs from DFT computational work is based on the open Python Materials Genomics (pymatgen) library [269]. The PyDII tool is developed as part of pymatgen and

is intended to be useful for the research community interested in studying the intrinsic intermetallic defects and conducting high-throughput screening of solute additions to produce desired changes in intrinsic properties. The following serves as a concise overview of the method and a "user-guide" for the use of this computational tool.

The rest of this section is organized as follows. Section A.2 describes the computational algorithm and workflows of PyDII. The implementation details are described in Section A.3 where technical requirements, input and output of PyDII are discussed. Several examples are illustrated in Section A.4. The discussion on future developments is presented in Section A.5.

The work presented in this appendix is prepared by H. Ding, B. Medasani, W. Chen, A. Canning, K. Persson, M. Haranczyk and M. Asta for a manuscript submitting to Comput. Phys. Commun..

A.2 Methodology

A.2.1 Constitutional and thermal defect

A low-temperature expansion based formalism described in Ref. [268] is implemented here in a high-throughput framework. Below, we present a short review of the methodology.

For an intermetallic crystal structure with N lattice sites, the site occupation, $c_i(p)$, with $p \in [1, N]$, is defined as 1 if lattice site p is occupied by element i, or 0 otherwise. The total number of sites occupied by the i^{th} element, N_i, in the system is given by the sum over all lattice occupation values, i.e. $N_i = \sum_p (c_i(p))$.

To predict the equilibrium concentration of point defects we employ a dilute-solution thermodynamic formalism. Such formalisms have been described by several different authors in the literature and in what follows we will make use of the development described in Ref. [268], where a first-order low-temperature expansion yields the configurational grand potential Ω due to the constitutional and thermal defeats as

$$\Omega = E^0 - \sum_i \mu_i \sum_p c_i^0(p) - k_B T \sum_p \sum_\epsilon \exp\{-[\delta E^\epsilon(p) - \sum_i \mu_i \delta c_i^\epsilon(p)]/k_B T\}. \quad \text{(A.1)}$$

Here, μ_i is the chemical potential of element i, k_B is Boltzmann's constant and T is temperature. E^0 and c_i^0 denote the ground-state energy and composition of element i on lattice site p for a perfectly ordered, stoichiometric alloy, respectively. For each possible defect ϵ at lattice site p, the corresponding changes in energy and site-composition are represented by $\delta E^\epsilon(p)$ and $\delta c_i^\epsilon(p)$, respectively. Using the same notation as in Ref. [268], hereafter, $\delta E^\epsilon(p)$ and $\delta E^\epsilon(p) - \sum_i \mu_i \delta c_i^\epsilon(p)$ will be referred as the defect "excitation energy" and defect formation energy, respectively. Using the thermodynamic relationship $\langle c_i \rangle = -\partial\Omega/\partial\mu_i$, Equation A.1 further yields

$$\langle c_i(p) \rangle = c_i^0(p) + \sum_\epsilon \delta c_i^\epsilon(p) \cdot \exp\{-[\delta E^\epsilon(p) - \sum_j \mu_j \delta c_j^\epsilon(p)]/k_B T\}, \quad \text{(A.2)}$$

where $\langle c_i(p) \rangle$ denotes the average concentration of element i at site p. At a given temperature, we can derive the defect concentrations of interest after substituting element

chemical potentials, μ_i. More commonly, we are interested in knowing the equilibrium point-defect concentrations as a function of the overall alloy concentration. Specifically, let $X_i = N_i / \sum_i N_i$ be the mole fraction of species i, where $N_i = \sum_p \langle c_i(p) \rangle$ is the number of atoms of species i on the lattice. In general, specifying the $M-1$ independent mole fractions, where M is the number of atom species, provides from Equation A.2 a total of $M-1$ equations for the M values of μ_i. In this formalism, the vacancy is treated as an additional species, for which equilibrium is dictated by setting the grand-potential Ω in Equation A.1 equal to zero (corresponding to thermodynamic equilibrium relative to the number of lattice sites under zero stress conditions). There results then M equations to determine the M values of μ_i, from which the equilibrium point defect concentrations $\langle c_i(p) \rangle$ can be determined from Equation A.2.

The left panel of Figure A.1 is the flow chart describing the calculations of constitutional and thermal defect concentrations. The intermetallic compound information like crystal structure, symmetrically distinct sites, and stoichiometric concentration are derived from either experimental or computational entries in a database. The defect module of Pymatgen is used to generate the proper-size supercell and defect structures and corresponding DFT setting. After finishing the DFT calculations, the post processing codes are first used for obtaining the defect "excitation energy" and solving for the chemical potential of each species at a given temperature and composition. The resulting values of the chemical potentials can be further substituted into Equation A.2 to compute the corresponding defect concentrations.

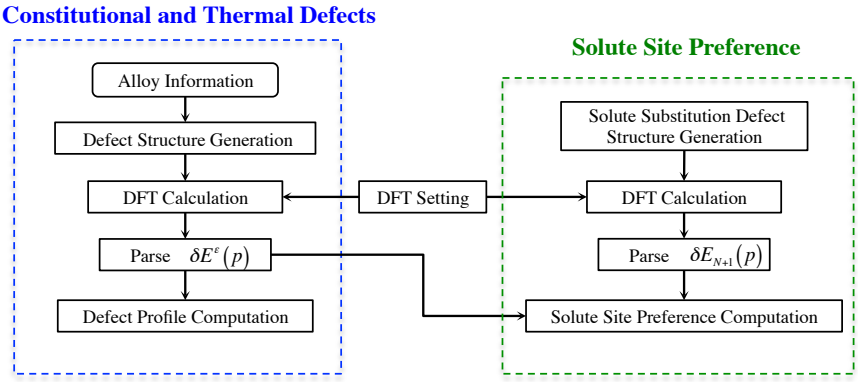

Figure A.1: Flow chart describing the workflow for the constitutional/thermal defect and solute site preference computation

A.2.2 Solute Site Preference

The solute site preference is a simple extension of the above mentioned constitutional and thermal defect computation. Given an external element $(M+1)$ in the dilute limit is introduced into the compound, the site preference of the solute over the N different

lattice sites can be considered within the current computational framework. In addition to the vacancy and antisite defect computations that have been done before, another set of N defect structures representing the substitutional defects of external element on each lattice site could be established and calculated, by regarding the external element as the element $M+1$ in the compound. The external element introduces one extra chemical potential into Equation A.2, requiring an additional equation to compute the chemical potentials. The extra constraint could be introduced by imposing a small but fixed amount of the mole fraction (like 0.5% or 1%) for the external element in the alloy. Herein, the introduction of this $(M+1)^{th}$ constraint into the system would yield another set of chemical potentials for the alloy at a given temperature and composition. Similar to the previous defect concentration computation, by substituting the chemical potentials back to Equation A.2, the corresponding defect concentration could be derived, and the site preference could be presented by comparing the solute occupation over each lattice sites, i.e. $\langle c_{M+1}(p)\rangle / \langle c_{M+1}(p^{'})\rangle$. The work flow for the calculations of solute site preference computation is presented in the right panel of Figure A.1, while additional N external element substitution structure calculations would be set for the defect structure computations.

A.3 Running the code

In this section, we will describe one basic approach to do the required calculations. The software developed for this purpose is in Python, so the user proficient in python can modify the codes according to their situations. The software is developed as part of pymatgen and has a dependency on sympy [270] and numpy [271] python packages. The software was developed and tested for Linux and Mac OS X, however it is expected to work on Windows also.

To determine the intermetallic defect property, the most important input is the crystal structure, which gives basic information about symmetry, lattice site, stoichiometric concentration etc. Materials Project [272] has provided free access to crystal structure information of many intermetallics through its Materials Application Programming Interface (MAPI) [269]. In the Materials Project database, each structure is assigned a unique id called mpid (Materials Project Id). The mpid is of the format "mp-1234" with "mp-" prefixed to a positive integer. In what follows, the $B2$-NiAl (mp-1487) would be taken as an example for running these defect property calculations.

A.3.1 Equilibrium Constitutional and Thermal Dects

First, we generate the defect supercells and the bulk supercell using the defect structure generator within pymatgen. Then the input files for the Vienna Ab-initio Simulation Package (VASP) [273, 274], a first-principles DFT package are generated using the VASP IO module of pymatgen [275]. The two steps are combined into a single command:

```
▷ gen_def_structure      --mpid       ⟨mpid⟩
                    [    --mapi_key   ⟨mapi_key⟩                  ]
                    [    --cellmax    ⟨max_no_atoms_in_supercell⟩ ]
```

This command will create the corresponding "mp-id" folder which contains one bulk and several defect structure computation folders. The cellmax parameter is the maximal number of atoms in the defect supercell. If not given, a default value of 128 is used according to our convergence tests convergence tests for metal systems. Among those computation folders in the "mp-id" folder, one "bulk" folder would contain the files for the supercell calculations of pristine crystal structure, and the other folders can be classified into two categories according to the type of defects: vacancy and antisite. To distinguish the lattice sites, we enumerate the lattices site from 1 to n, where n is the total number of symmetrically distinct lattice sites in the perfect crystal structure. Each defect supercell calculation is put in one folder; for the case of NiAl (mp-1487) where there are two distinct lattice sites, there would be four defect folders, corresponding to one antisite and one vacancy defect on each sublattice: besides the structure file (POSCAR) in each folder, other

Defect Type	Folder Name
Vac_{Al}	vacancy_1_sitespecie-Al,
Vac_{Ni}	vacancy_2_sitespecie-Ni,
Ni_{Al}	antisite_1-sitespecie-Al_subspecie-Ni
Al_{Ni}	antisite_2_sitespecie-Ni_subspecie-Al

files (e.g. INCAR, KPOINTS, POTCAR) with computation details could be automatically generated according to user's settings in pymatgen. The default settings chosen for each of the files should be based on convergence tests.

Provided that all the DFT calculations including defect and bulk structures are successfully completed, the next step is to parse the results to obtain the defect "excitation energies", $\delta E^{\epsilon}(p)$, which are simply the energy differences between the pristine and defect structures. To accomplish this task, a typical command-line would be

```
▷ gen_def_energy      --mpid       ⟨mpid⟩
                  [   --mapi_key   ⟨mapi_key⟩   ]
```

Once the command has successfully parsed the energies for all the defects, it replies with:

DFT calculations successful for ⟨mp-id⟩

The output file "ext_ene_mp-id.json" contains the defect "excitation energies", as well as other structure information for the next step to calculate defect concentration. The data in the json file is used to derive the constitutional and thermal defect concentrations at a given temperature around the stoichiometric concentration region (defaulted for ± 0.5%), type:

```
▷ gen_def_profile      --mpid   ⟨mpid⟩
                   [   --temp   ⟨T⟩      ]
```

Here, temperature parameter ⟨T⟩ indicates the temperature of interest (in units of K), with a default value of 1000 K. This will create the output file "def_con_mp-id.json", which stores the defect concentrations, defect formation energies, and elemental chemical potentials as a function of composition.

A.3.2 Solute Site Preference

As an extension of constitutional and thermal defect concentration calculation, external solute site preference calculation could be started by the following command :

```
▷ gen_sol_pref_structure    --mpid       ⟨mpid⟩
                            --solute     ⟨solute_element⟩
                        [   --mapi_key   ⟨mapi_key⟩        ]
```

This will help create additional N computation folders inside the "mp-id" directory, corresponding to the configurations where the external solute occupies each of original n sublattice sites. The external specie of interest could be specified by the chemical symbol of the element from the input of ⟨solute_element⟩.

For example, for the NiAl example the command "gen_sit_prefence --mpid 1487 --solute Mo' would generate the following two additional folders in "mp-1487" directory for next-step DFT calculations:

Defect Type	Folder Name
Mo_{Al}	sitepre_1_sitespecie-Al_subspecie-Mo
Mo_{Ni}	sitepre_2_sitespecie-Ni_subspecie-Mo

After finishing the additional N DFT calculations in the folders, similarly, the solute defect "excitation energies" on each lattice site could be obtained using the command:

```
▷ gen_sol_def_energy    --mpid       ⟨mpid⟩
                        --solute     ⟨solute_element⟩
                    [   --mapi_key   ⟨mapi_key⟩        ]
```

A set of solute "excitation energies" for the $n+1$ solute occupying the site p, $\delta E_{n+1}(p)$, would be be stored in "ext_energy_⟨mpid⟩_solute-⟨solute_name⟩.json" file, with the reply:

DFT calculations for solute ⟨solute_element⟩ on ⟨mp-id⟩ are successful

Along with the previous output file "ext_energy_⟨mpid⟩ .json", the site preference of the external solute could be analyzed by typing:

```
▷ gen_sol_site_pref      --mpid    ⟨mpid⟩
                         --solute  ⟨solute_element⟩
                  [      --temp    ⟨T⟩                ]
```

Here, the temperature parameter also has a default value of 1000 K. The command outputs the percentage of external solute occupying one specific lattice site as a function of stoichiometry ratio at the given temperature.

A.4 Example

Three examples are presented here; the first two show the equilibrium intrinsic defect computations for NiAl (mp-1487) and Al_3V (mp-2554) and the third example demonstrates the site preference calculations of Ti, Mo and Fe solutes in NiAl (mp-1487) crystal structure.

A.4.1 Equilibrium Constitutional and Thermal Defects

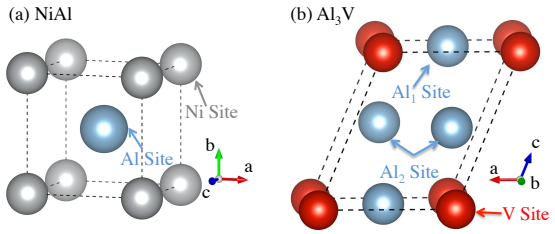

Figure A.2: Crystal structure of (a) NiAl with one Ni and one Al site (b) Al_3V with two symmetrically distinct Al and one V site.

NiAl (mp-1487)

The well-studied $B2$-NiAl (mp-1487) crystal structure, as shown in Figure A.2 (a), is used to verify that our codes produce output consistent with previously published calculations [196, 276]. In the B2-NiAl structure, Ni and Al atoms occupy the corner and center lattice sites of a cubic cell in the $Pm\bar{3}m$ (221) space group. Four different defect calculations are considered here, as Vac_{Al}, Vac_{Ni}, Al_{Ni} and Ni_{Al}, along with the bulk structure. Equilibrium concentrations of these defects at the temperature of $T = 1000\ K$ are plotted in Figure A.3 (a). The relative order of the magnitude for the four defect concentrations as found in with previous calculations from Korzhavyi *et al.* [196] and Mishin [197], while the reported values of defect concentrations as a function of stoichiometry are qualitatively consistent with previous calculations to within an order of magnitude. The difference between calculations may be associated with the choice of pseudopotentials, supercell size and relaxation schemes.

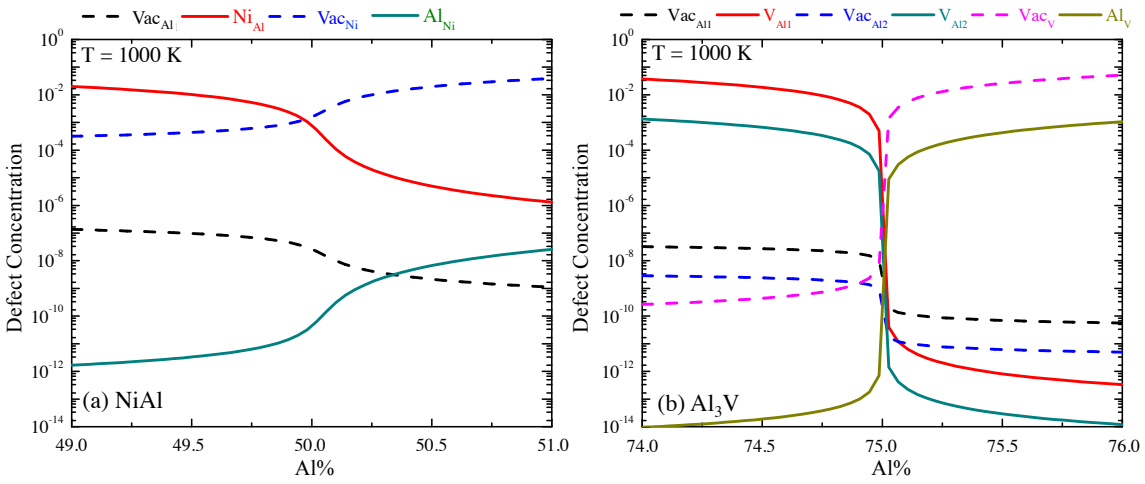

Figure A.3: Equilibrium constitutional and thermal defect concentrations in (a) NiAl and (b) Al_3V at T = 1000 K as a function of the mole fraction of Al.

Al_3V (mp-2554)

The current code also enables distinguishing symmetrically inequivalent sites and this is demonstrated with Al_3V (mp-2554). The Al_3V crystal structure has I4/mmm (139) space group with two symmetrically distinct Al lattice sites and one V site in a primitive cell, as shown in Figure A.2 (b). The symmetrically inquivalent Al sites warrant additional calculations leading to three vacancy and three antisite calculations. The constitutional and thermal defect concentration profiles for Al_3V around the ideal stoichiometry are plotted in Figure A.3 (b). Our calculations indicate that for Al-poor concentrations, the majority defects in the structure are V antisites on the Al sublattices, while for Al-rich concentrations, the dominant defects are vacancies on the V sublattices.

A comparison between Al1 and Al2 sites shows that the excessive V preferentially occupies Al1 site, and the antisite defection concentration V_{Al1} is about one order of magnitude higher than that of V_{Al2}. These calculations demonstrate the significant antisite defect property differences between the two Al lattice sites in Al_3V crystal structure.

A.4.2 Solute Site Preference

Solute Ti, Mo and Fe in NiAl (mp-1487)

As an extension of equilibrium constitutional and thermal defect concentration calculations, the solute site preference calculation examples are presented for solutes Ti, Mo and Fe in NiAl (mp-1487). Figure A.4 shows the calculated fraction of solute on Al sublattice as a function of Al concentration. Within the composition region considered here, the present examples feature three type of elements (i) strong site preference of Ti to Al sublattice, (ii) composition-dependent site preference of Mo and (iii) strong site preference of Fe to Ni sublattice. The behaviors of these three solute species in NiAl is consistent with

the previous calculations by Jiang [277].

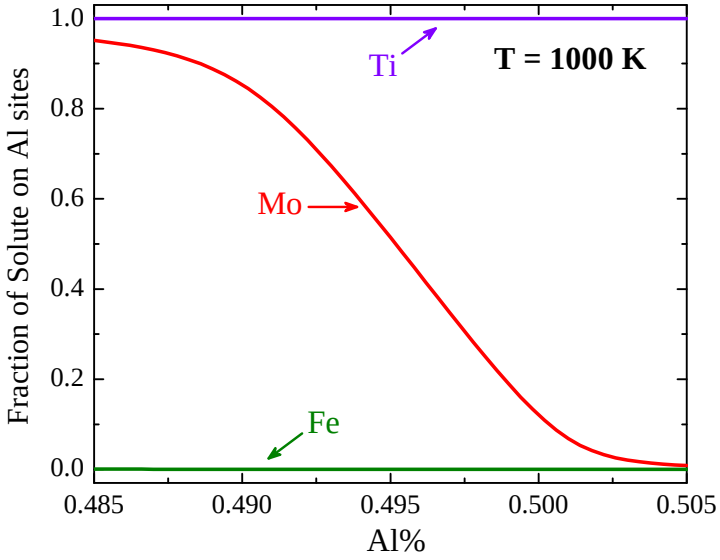

Figure A.4: Calculated fraction of solute X (X = Ti, Mo or Fe) occupying the Al sublattice in $Ni_xAl_{0.99-x}X_{0.01}$ alloys at T = 1000 K as a function of the mole fraction of Al.

A.5 Future developments

At the current state of development, PyDII is only handling binary intermetallic systems. For multicomponent systems, different concentration constraints could be provided. A more general code for inputing specific constraints would be written in the future to satisfy this kind of needs.

Based on the current equilibrium defect concentration with different composition, users could further derive other information of interest, like separating constitutional defects and thermal defects. Other post processing functions are under development to further interpret the output of current work and to derive other defect properties that may be relevant in the context of alloy design. As an open-source project, we welcome users to join the development of the PyDII. Any questions, suggestions or code contributions can be submitted to the pymatgen repository on Github.